Institute of Earth and Environmental Sciences

Thesis in cumulative form entitled:

SAR interferometry analysis of surface processes in the Pamir – Tien Shan active orogens - emphasis on coseismic deformation and landslides

Dissertation
to obtain the academic degree
“doctor rerum naturalium” (Dr. rer.nat.)
for the scientific discipline “Geology”
submitted to
the Faculty of Mathemathics and Natural Sciences
at the University of Potsdam

Kanayim Teshebaeva

Potsdam, March 2016

Published online at the
Institutional Repository of the University of Potsdam:
URN urn:nbn:de:kobv:517-opus4-96743
http://nbn-resolving.de/urn:nbn:de:kobv:517-opus4-96743

I herewith declare that the work in this present thesis is original except as acknowledged in the text. Passages in the text, taken analogously from other sources, are marked as such.

Financially support was provided by the VW-foundation postgraduate program, ‘Land Use, Ecosystem Services, and Human Welfare in Central Asia (LUCA)’ and the GFZ German Research Center for Geosciences.

Potsdam, March 2016

Kanayim Teshebaeva.

Acknowledgments

This work was a challenge for multiple reasons. I would have not succeeded to overcome this if I would have not had continuous support from friends, family, and people at work. I am satisfied as I learned how to do real science, and improved my existing expertise. I hope this thesis will be useful to other researchers and contribute to the radar remote sensing.

I like to thank Helmut Echtler for his continuous supervision to my work and logistical support at the university. His mentorship has been tireless. His door was always open for discussion and encouraging support.

I am grateful to Sigrid Roessner, who is principal investigator of the postgraduate LUCA program, which provided the initial opportunity. She welcomed and motivated me to do this PhD work.

My special thanks at Potsdam University are for Manfred Strecker, who substantially supported and motivated me to continue my research. He provided me opportunities to enlarge considerably my experiences in earth sciences.

I thank specially Henriette Sudhaus, who encouraged and supported me very much during the initial stage of my PhD. I also thank Bodo Bookhagen and Oliver Korup for very fruitful discussions and contribution. My specials thanks go to Ed Sobel and Gerold Zeilinger for encouraging advice and guidance in the fieldwork.

I am grateful to Katy Unger-Shayesteh, who became a very good friend and supported me throughout my PhD work. She involved me to Central Asian Water project activities.

My special thanks to Sylvia Magnussen who has constantly supported me. Many thanks to the nice colleagues Uli Wetzel, Mahdi Motagh, Daria Golovko, that helped in different moments.

Last but not least I am grateful to my parents and family for their continuous support and encouragements.

Contents:

Abstract

This thesis presents new approaches of SAR methods and their application to tectonically active systems and related surface deformation. With 3 publications two case studies are presented:

(1) The coseismic deformation related to the Nura earthquake (5th October 2008, magnitude Mw 6.6) at the eastern termination of the intramontane Alai valley. Located between the southern Tien Shan and the northern Pamir the coseismic surface displacements are analysed using SAR (Synthetic Aperture RADAR) data. The results show clear gradients in the vertical and horizontal directions along a complex pattern of surface ruptures and active faults. To integrate and to interpret these observations in the context of the regional active tectonics a SAR data analysis is complemented with seismological data and geological field observations. The main moment release of the Nura earthquake appears to be on the Pamir Frontal thrust, while the main surface displacements and surface rupture occurred in the footwall and along of the NE–SW striking Irkeshtam fault. With InSAR data from ascending and descending satellite tracks along with pixel offset measurements the Nura earthquake source is modelled as a segmented rupture. One fault segment corresponds to high-angle brittle faulting at the Pamir Frontal thrust and two more fault segments show moderate-angle and low-friction thrusting at the Irkeshtam fault. The integrated analysis of the coseismic deformation argues for a rupture segmentation and strain partitioning associated to the earthquake. It possibly activated an orogenic wedge in the easternmost segment of the Pamir-Alai collision zone. Further, the style of the segmentation may be associated with the presence of Paleogene evaporites.

(2) The second focus is put on slope instabilities and consequent landslides in the area of prominent topographic transition between the Fergana basin and high-relief Alai range. The Alai range constitutes an active orogenic wedge of the Pamir – Tien Shan collision zone that described as a progressively northward propagating fold-and-thrust belt. The interferometric

analysis of ALOS/PALSAR radar data integrates a period of 4 years (2007-2010) based on the Small Baseline Subset (SBAS) time-series technique to assess surface deformation with millimeter surface change accuracy. 118 interferograms are analyzed to observe spatially-continuous movements with downslope velocities up to 71 mm/yr. The obtained rates indicate slow movement of the deep-seated landslides during the observation time. We correlated these movements with precipitation and seismic records. The results suggest that the deformation peaks correlate with rainfall in the 3 preceding months and with one earthquake event. In the next step, to understand the spatial pattern of landslide processes, the tectonic morphologic and lithologic settings are combined with the patterns of surface deformation. We demonstrate that the lithological and tectonic structural patterns are the main controlling factors for landslide occurrence and surface deformation magnitudes. Furthermore active contractional deformation in the front of the orogenic wedge is the main mechanism to sustain relief. Some of the slower but continuously moving slope instabilities are directly related to tectonically active faults and unconsolidated young Quaternary syn-orogenic sedimentary sequences. The InSAR observed slow moving landslides represent active deep-seated gravitational slope deformation phenomena which is first time observed in the Tien Shan mountains. Our approach offers a new combination of InSAR techniques and tectonic aspects to localize and understand enhanced slope instabilities in tectonically active mountain fronts in the Kyrgyz Tien Shan.

Key words: Synthetic Aperture Radar; earthquake; landslide; Pamir-Tien Shan; InSAR.

Zusammenfassung

Die vorliegende Arbeit stellt neue Ansätze zu Methoden des „Synthetic Aperture Radar“ (SAR) vor und wendet diese auf tektonisch aktive Systeme und die damit einhergehende Oberflächenverformung an. In drei wissenschaftlich begutachteten Publikationen in internationalen Fachzeitschriften werden im wesentlichen zwei Fallstudien präsentiert:
(1) Die koseismische Verformung in Folge des Nura-Erdbebens (5. Oktober 2008, Mw 6.6) am östlichen Rand des intramontanen Alai-Beckens. Die koseismischen Verformungen an der Erdoberfläche wurden im Bereich zwischen dem südlichen Tien Shan und dem nördlichen Pamir mit Hilfe von SAR („Synthetic Aperture Radar“) Daten analysiert. Die Ergebnisse zeigen klare, sowohl horizontale als auch vertikale Gradienten, die entlang eines komplexen Musters von Brüchen an der Oberfläche und aktiven Störungen ausgebildet sind. Um diese Beobachtungen interpretieren und in den regionalen tektonischen Zusammenhang stellen zu können, wurde die SAR-Analyse durch seismologische und geologische Felduntersuchungen ergänzt. Die hauptsächliche Freisetzung der seismischen Energie des Nura-Erdbebens scheint an der frontalen Pamir-Überschiebung erfolgt zu sein, während die Hauptverformung und Oberflächenrupturen im Liegenden und entlang der NE-SW streichenden Irkeshtam-Störung auftraten. Unter Nutzung von InSAR-Daten von den aufsteigenden und absteigenden Satelliten-Bahnen sowie von Pixel-Versatz-Messungen wurde das Nura-Erdbeben als ein segmentierter Bruch modelliert. Dabei entspricht ein Segment einer steilen spröden Verwerfung an der frontalen Pamir-Überschiebung, während zwei andere Segmente mittel-steile und reibungsarme Verwerfungen an der Irkeshtam-Störung zeigen. Die integrierte Analyse der koseismischen Deformation spricht für eine Segmentierung des Bruches und eine Verteilung der Verformung in Folge des Erdbebens. Dies hat möglicherweise einen Gebirgskeil im äußersten östlichen Teil der Pamir-Alai-Kollisionszone aktiviert. Zudem könnte die Art der Segmentierung mit der Ablagerung von Paläogenen Evaporiten assoziiert sein.
(2) Der zweite Schwerpunkt wurde auf tief-liegende langsame Böschungsverformungen gelegt, die insbesondere im Gebiet des markanten Übergangs zwischen dem Fergana-Tal und dem Hochrelief der Alai-Gebirgskette ausgeprägt sind. Die Alai-Kette stellt einen aktiven Gebirgskeil der Pamir-Tien-Shan-Kollisionszone dar, welche als ein sich stufenweise nach Norden fortsetzender Falten- und Überschiebungsgürtel beschrieben wird. Die interferometrische Analyse von ALOS/PALSAR-Radardaten deckt einen Zeitraum von vier Jahren ab (2007-2010) und nutzt den „Small-Basline-Subset“ (SBAS) Zeitreihenansatz um Oberflächendeformationen mit Millimeter-Genauigkeit zu bestimmen. 118 Interferogramme

wurden analysiert, um die räumlich-kontinuierlichen Bewegungen mit Hangabwärts-Geschwindigkeiten von bis zu 71 mm/Jahr zu beobachten. Die erhaltenen Raten weisen auf eine langsame Bewegung von tief-verwurzelten Hangrutschungen während der Beobachtungszeit hin. Wir korrelierten diese Bewegungen mit Niederschlags- und seismischen Beobachtungen. Die Ergebnisse deuten darauf hin, dass die größten Deformationen mit den Regenmengen der drei vorhergehenden Monate und mit einem Erdbebenereignis korrelieren. Im nächsten Schritt wurden die tektonischen und lithologischen Verhältnisse mit den Mustern der Oberflächendeformation kombiniert, um das räumliche Muster der Hangrutschungsprozesse zu verstehen. Wir zeigen, dass die lithologischen und tektonischen Strukturen die Hauptkontrollmechanismen für das Auftreten von Hangrutschungen und für den Grad der Oberflächendeformation sind. Darüber hinaus ist die aktive Kontraktion und Einengungstektonik an der Vorderseite und Front des kontinentalen Akkretionskeils der hauptsächliche Mechanismus der Relieferhaltung. Einige der langsameren aber kontinuierlich in Bewegung befindlichen Instabilitäten stehen in direktem Zusammenhang mit der tektonisch aktiven Störungen und Hebung sowie mit unkonsolidierten, jung-quartären synorogenen Molassesedimenten. Unser Ansatz bietet eine neue Kombination von InSAR-Techniken und tektonischen Aspekten um Hanginstabilitäten in tektonisch aktiven Gebirgsfronten im Kirgisischen Tien Shan zu lokalisieren und zu verstehen.

Key words: Synthetic Aperture Radar; earthquake; landslide; Pamir-Tien Shan; InSAR-Techniken.

Chapter 1

1.1 Problem statement

On 5th October of 2008, the 6.6 magnitude Nura earthquake struck Alai region, killing about 74 people, injuring many and destroying dozens of buildings in the Pamir-Tien Shan collision zone. The region is characterized by frequent seismicity associated with the southward subduction of the Eurasian continental crust (Arrowsmith and Strecker, 1999; Bazhenov, 1993; Biske, 1996; Burtman, 2000; Burtman, 2006; Cobbold et al., 1996; Molnar and Tapponnier, 1975; Strecker et al., 1995). In the NEIC (National Earthquake Information Center, United States Geological Survey) catalog, approximately 270 earthquakes have been recorded with magnitudes of 4 and larger, between 1973 and 2011. Along with frequent ground shaking the region is affected by destructive landslides. Approximately 4500 landslides were observed in this region between 1969 and 2010 (Ibatulin, 2011). The frequent occurrence of large landslides leads to extensive damage to settlements and infrastructure as well as loss of human lives. Thus, catastrophic landslides on 22 April 2003 killed 38 people in the village of Kara-Taryk of Alai range. One year later on 27 April 2004, 33 people were buried and killed under a landslide in the same region. A total of 20 landslides were recorded during April 2004 alone, prior to these landslides on 9th April 2004 the Uzgen area has been affected by a shallow earthquake with magnitude 4.2 Mw (Ibatulin, 2011).

Destructive earthquakes and landslides represent one of the major natural hazards in the Pamir-Alai collision zone. Mitigation of the effects of such natural disasters requires a fast response system including continuous deformation monitoring and analysis scheme. Surface deformation measurements are used to constrain the subsurface geometry of active faults and the spatial distribution of coseismic slip. The key to understand earthquakes and landslides is our ability to characterize the actual state of stress and to understand the interaction between surface changes of topography, lithology and tectonic structures. Modern advances in interferometric synthetic aperture radar (InSAR) during the last decade, improved our ability to understand these and other crustal processes.

This dissertation contributes to monitoring and understanding surface deformation by combining recent/advanced InSAR techniques and morphometric analysis in tectonically active mountain fronts in the Pamir – Tien Shan. Two case studies are presented: (1) focuses on the site which has been affected by the destructive 2008 Nura earthquake in the northern Pamir mountain front; (2) focuses on the site of high landslide activity in the southern Tien Shan mountain front of the Alai range (Fig.1).

1.2 Tectonic setting of the study area

The Pamir-Alai mountains constitute the collision zone between the southern Tien Shan and the northern front of the Pamir (Fig 1). These Central Asian intracontinental mountain belts (Arrowsmith and Strecker, 1999; Bazhenov, 1993; Biske, 1996; Burtman, 2000; Burtman, 2006; Cobbold et al., 1996; Molnar and Tapponnier, 1975; Strecker et al., 1995) are active since Late Cenozoic (Sobel et al., 2013) and resulted in high elevation relief associated with crustal scale fold and thrust belts.

The region is characterized by frequent seismicity associated with the southward subduction of the Eurasian continental crust below the northward propagating Indian plate (Molnar et al. 1973; Arrowsmith & Strecker 1999; Coutand et al. 2002; Strecker et al. 2003). The intracontinental ranges of the Central Asian orogens record largely distributed N-S directed shortening and strong uplift. So far it is considered that most of the deformation in the south-western Pamir-Alai zone is accommodated within a narrow zone with contracting Pamir and Alai valley (Molnar et al. 1973; Arrowsmith & Strecker 1999; Coutand et al. 2002; Strecker et al. 2003). The estimated rate of N-S shortening between northern Pamir and southern Tien Shan is 10 to 15 mm/yr (Reigber et al. 2001; Yang et al. 2008; Zubovich et al. 2010).
This study focuses on the eastern termination of this system and its northern extent at the deformation front between the Alai range and Fergana basin. This region faces a diversity of natural hazards which frequently lead to the occurrence of natural disaster (e.g., 1994: about 1,000 landslides caused 115 human fatalities; 2008: Nura earthquake M=6.6 led to74 human fatalities and 150 injured people) (Kalmetieva et al. 2009).

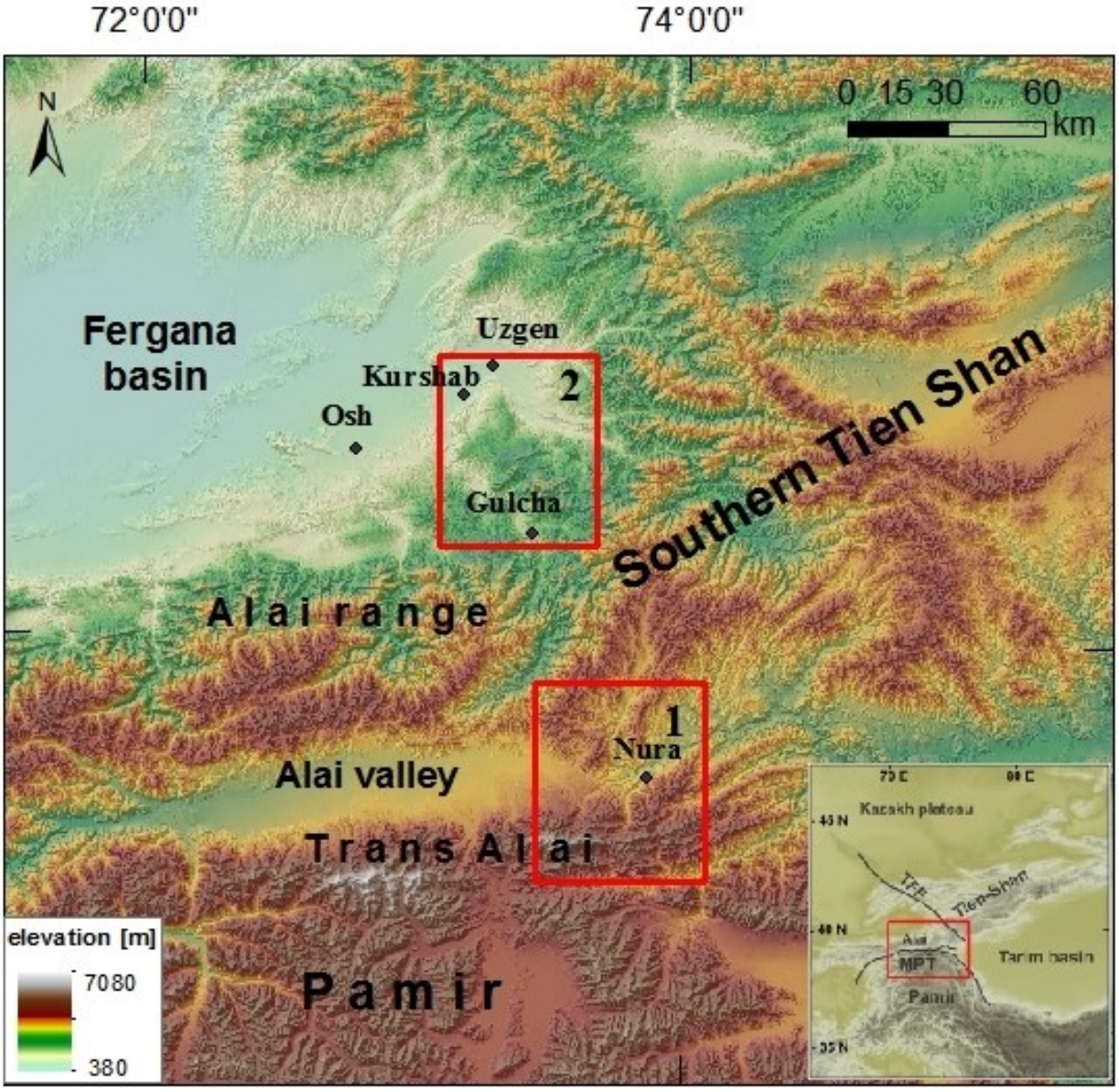

Figure 1. Geographic location of the investigated areas in the southern Tien Shan and Pamir mountains. The red boxes indicates the case study 1 the Nura earthquake and case study 2 landslides

1.3 Methods

Methodological focus has been put on using Synthetic Aperture Radar (SAR) data acquired by different satellites for detecting surface displacements as a consequence of earthquakes and slope instabilities in the Pamir-Alai ranges. Radar remote sensing as a so-called active remote sensing technique is based on microwave radiation. The radar system (antenna) emits non-optical microwave wavelengths ranging from a few centimeters to more than one meter. The same antenna records the returned signals after they have been backscattered from the Earth's surface. In comparison to optical remote sensing, radar has the advantage of being independent from clouds and daylight. The first civilian satellite-based radar remote sensing systems have become wider available at the beginning of the 1990-ies (e.g., ERS-1, JERS-1) whereas their number and quality have steadily increased since then. Based on these data various analysis techniques have been developed. One group of methods focuses on multi-temporal analysis of SAR data for quantitative assessment of surface displacements comprising Differential SAR Interferometry (D-InSAR), InSAR time-series and pixel offset techniques. In this study these methods are used for analyzing surface displacements which are related to earthquakes and landslides in southern Kyrgyzstan. We complement our remote sensing analysis by field investigations in order to validate and interpret our SAR-based results.

1.3.1 Synthetic Aperture Radar (SAR) Interferometry

The InSAR is a powerful image analysis technique which has successfully been used for geophysical monitoring of a wide range of processes representing potential natural hazards. They include earthquake-caused surface rupturing and deformation as well as mass movements (e.g. Wright et al., 2001; Fialko et al., 2005; Zhao et al., 2012; Wasowski & Bovenga, 2014). In the result InSAR has emerged as a widely used method for spatially continuous detection and mapping of surface deformation. It allows quantification of deformation causing topographical changes in the range of centimeters by analyzing differences in the phase component of the radar signal recorded by the remote sensing sensor.

Depending on the temporal repeat interval of InSAR data acquisition, deformation rates can be derived for time spans ranging between days and years by performing time series analysis in order to determine slow and temporal uniform deformation. The quality of the radar

interferometry results is influenced by the size of the observing radar wavelength (Michel and Rignot, 1999). Shorter wavelength as C-band (Table 1) are more irregularly backscattered from the surface increasing the noise part of the signal. Whereas longer wavelength L-band (Table 1) performs better in highly vegetated environments, and the phase signal is less susceptible to degradation of signal quality due to temporal change in backscattering. These factors are described by the interferometric coherence as mainly determining the quality of the interferometric measurement.

Coherence is sensitive to microscopic object properties and to short-term scatter changes. The thematic information content decreases with increasing acquisition interval, mainly due to phenological or manmade changes of the object or differing weather conditions (e.g. Rosen et al. 2000). In case of high dynamics of surface changes coherence can be reduced to the point of its complete loss making it impossible to apply InSAR techniques. In such cases the pixel offset method represents an alternative.

1.3.2 Pixel offset

Surface displacement may also be derived from the correlation peak of the amplitudes of the intensity images using the pixel offset method. The resulting pixel offsets represent two-dimensional vector displacements and are more robust against temporal decorrelation of the radar signal because they are based on the image intensity information. In order to obtain reliable estimates of the surface displacement, these image offsets need to be determined with sub-pixel precision (Michel and Rignot, 1999). The overall accuracy of this method is mainly determined by the size of the image pixels (spatial resolution of the sensor, Table 1).

Table 1. Satellite missions characteristics of the analyzed SAR data

Characteristics	**ENVISAT /ASAR ESA**	**ALOS/PALSAR Jaxa**
Launch date	March 1, 2002	Jan. 24, 2006
Wavelength	C-band(56mm)	L-band (236 mm)
Repeat cycle	35 days	46 days
Resolution	20m (ASAR)	7m to 44m (FBS Mode) 14 to 88m (FBD Mode)

1.4 Thesis outline

The thesis consists of three manuscripts two of which have been published and third is under review in scientific journals. For each associated manuscript there are multiple authors, however, the author of this dissertation is the primary researcher and first author.

Chapter 2 present a study of the 2008 Nura earthquake which struck the eastern termination of the Alai valley in the Pamir-Tien Shan continental collision zone. We measure the coseismic surface displacements using SAR data. The results show clear gradients in the vertical and horizontal directions along a complex pattern of surface ruptures and active faults.
This chapter has been published in *Geophysical Journal International by Oxford University Press on behalf of the Royal Astronomical Society. All rights reserved*:

Teshebaeva, K., Sudhaus, H., Echtler, H., Schurr, B., Roessner, S., (2014). Strain partitioning at the eastern Pamir-Alai revealed through SAR data analysis of the 2008 Nura earthquake**.** *Geophysical Journal International 198: 760-774; doi:10.1093/gji/ggu158.*

Chapter 3 investigates the potential of the L-band ALOS/PALSAR time-series data radar interferometry to monitor landslide phenomena in the southern Tien Shan mountains. The temporal evaluation of the results suggests that the deformation peaks correlate with rainfall in the 3 preceding months and with an earthquake event. The results of this study indicate the great potential of L-band InSAR time series analysis for efficient spatiotemporal identification and monitoring of slope mobilization in this region of high landslide activity in southern Kyrgyzstan.
This chapter has been published in *Remote Sensing Journal*:

Teshebaeva, K., Roessner, S., Echtler, H., Motagh, M., Wetzel, H.-U., Moldobekov, B., (2015). ALOS/PALSAR InSAR Time-Series Analysis for Detecting Very Slow-Moving Landslides in Southern Kyrgyzstan. *Remote Sensing 7: 8973-8994; doi:10.3390/rs70708973.*

Chapter 4 focus is to investigate deep-seated gravitational slope deformation using ALOS/PALSAR time series data in the southern Tien Shan mountain front. The data show continuous and constant movements in this period with downslope velocities up to 71 mm/yr. The obtained very slow but continuously moving slope instabilities are directly related to active faults and unconsolidated young mainly Quaternary syn-orogenic sedimentary sequences.
This chapter is submitted to journal of *Geomorphology*.

Teshebaeva Kanayim, Echtler Helmut, Bookhagen Bodo, Strecker Manfred. Styles of surface deformation in the Southern Kyrgyz Tien Shan revealed from InSAR analyses and tectonic geomorphology.

Chapter 5 provides a summary of the thesis and future work.

Chapter 2

Strain partitioning at the eastern Pamir-Alai revealed through SAR data analysis of the 2008 Nura earthquake

Kanayim Teshebaeva[1,3], Henriette Sudhaus[1], Helmut Echtler[1,2], Bernd Schurr[1] and Sigrid Roessner[1]

[1] GFZ German Research Centre for Geosciences, Telegrafenberg, 14473 Potsdam;
[2] Institute of Earth and Environmental Sciences, Universität Potsdam, 14476 Potsdam;
[3] CAIAG Central Asian Institute for Applied Geosciences, Timur-Frunze str.73/2, Bishkek, Kyrgyzstan

SUMMARY

On 2008 October 5, a magnitude 6.6 earthquake struck the eastern termination of the intermontane Alai valley between the southern Tien Shan and the northern Pamir of Kyrgyzstan. The shallow thrust earthquake occur red in the footwall of the Main Pamir thrust, where the Pamir orogen is colliding with the southern Tien Shan mountains. We measure the coseismic surface displacements using SAR (Synthetic Aperture RADAR) data; the results show clear gradients in the vertical and horizontal directions along a complex pattern of surface ruptures and active faults. To integrate and to interpret these observations in the context of the regional tectonics, we complement the SAR data analysis with seismological data and geological field observations. While the main moment release of the Nura earthquake appears to be on the Pamir Frontal thrust, the main surface displacements and surface rupture occurred in the footwall along the NE–SW striking Irkeshtam fault. With InSAR data from ascending and descending tracks along with pixel offset measurements, we model the Nura earthquake source as a segmented rupture. One fault segment corresponds to high-angle brittle faulting at the Pamir Frontal thrust and two more fault segments show moderate-angle and low-friction thrusting at the Irkeshtam fault. Our integrated analysis of the coseismic deformation argues for rupture segmentation and strain partitioning associated to the earthquake. It possibly activated an orogenic wedge in the easternmost segment of the Pamir-Alai collision zone. Further, the style of the segmentation may be associated with the presence of Paleogene evaporites.

Key words: Radar interferometry; Earthquake source observations; Asia.

2.1 INTRODUCTION

In 2008 October, the Mw6.6 Nura earthquake struck the eastern termination of the intermontane Alai Valley in the Pamir-Tien Shan continental collision zone. This earthquake caused 74 deaths and the destruction of property and infrastructure (Kalmetieva et al. 2009). The epicentre was located in southeaster n Kyrgyzstan at 39.51.N and 73.72.E, near the border with China and Tajikistan (Fig. 1). This region corresponds to the northernmost sectors of the Pamir orogen and the structurally complex collision zone between the Trans Alai and the Tien Shan mountains to the north (Fig. 1). Because of the rugged topography and the past political conditions in this remote area between China, Kyrgyzstan and Tajikistan, the regional geological setting is not well known.

The epicentral area of the Nura earthquake is located at the southern flank of the Trans Alai range and within the footwall block of the easternmost thrust system delineating the Pamir. The Trans Alai range of the Pamir and the associated contractional features of this region result from the ongoing convergence between the Indian indenter and the Eurasian plate (Burtman & Molnar 1993).

Recent geodetic analysis from continuous GNSS networks (Yang et al. 2008; Zubovich et al. 2010) across the Pamir orogen revealed that the central sector of the convex-northward Trans Alai accommodates more than 50 percent of the 25 mm/yr convergence between the Pamir and Eurasia (Reigber et al. 2001;Yang et al. 2008; Zubovich et al. 2010). Whereas most of the intracontinental ranges of the Central Asian orogens record largely distributed shortening and uplift, most of the deformation in the Pamir-Alai zone is accommodated within a narrow zone (Molnar et al. 1973; Arrowsmith & Strecker 1999; Coutand et al. 2002; Strecker et al. 2003, Fig. 1).

The segment of the Trans Alai mountain front affected by the Nura earthquake is situated in the footwall of the Pamir Frontal thrust zone and the eastern termination of the intermontane Alai Valley. This basin represents the vestige of a formerly contiguous sedimentary basin that linked the Chinese Tarim Basin in the east and the Tadjik Depression in the west (Burtman & Molnar

1993; Burtman 2000, Fig. 1). This tectonic segment marks the transition between the generally E–W striking tectonic structures in the central sector of the Trans Alai mountain front and the multiform eastern bend of the orogen, which is dominated by a complex set of structures showing shortening, strike-slip faulting, and extension farther south (Robinson et al. 2007; Sobel et al. 2013).

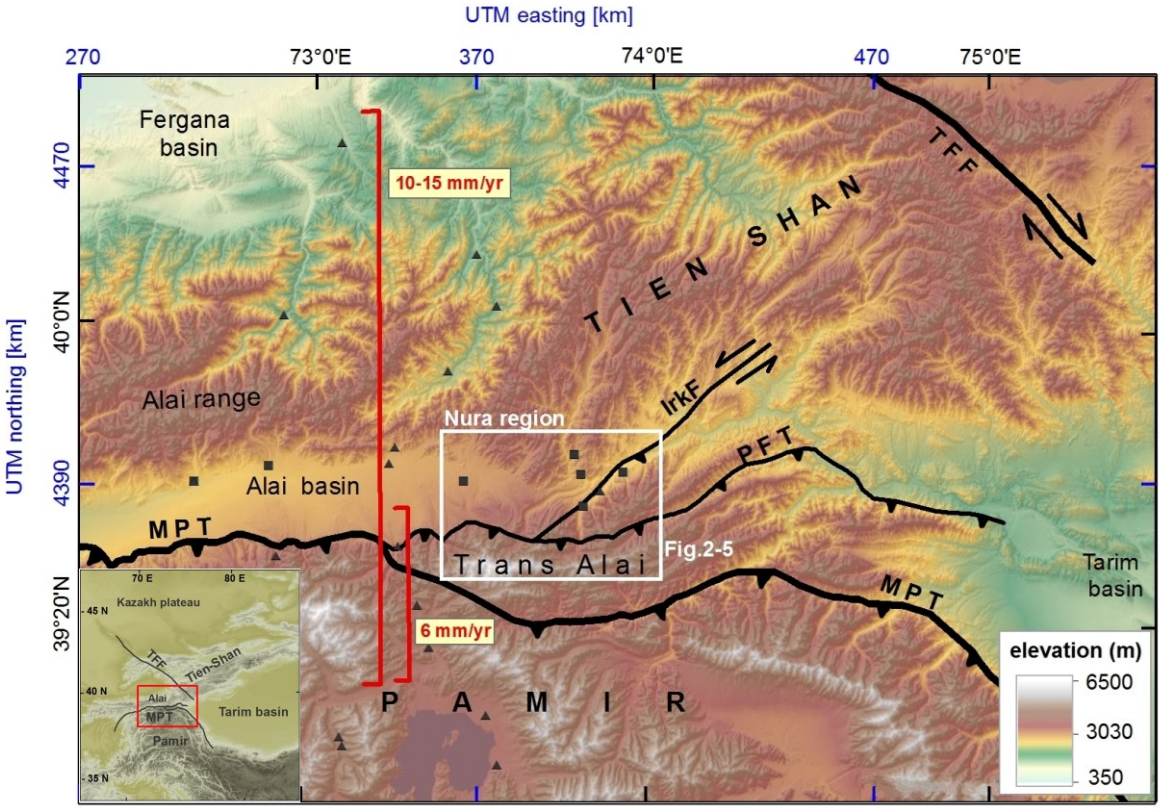

Figure1. Tectonic map of the northern Pamir–southwestern Tien Shan region showing the active faults (after Sobel etal.2013); (after Kalmetieva etal.2009) over the colour-shaded topographic relief from SRTM data (Farr & Kobrick 2000). The marked faults are the main Pamir thrust (MPT), the Pamir Frontal thrust (PFT), the Irkeshtam fault (IrkF) and the Talas-Fergana fault (TFF). The red lines mark transects in the Pamir-Alai region for which shortening rates (red numbers) have been estimated from GPS data (Reigber et al.2001; Yang et al.2008; Zubovich et al. 2010; Li Tao et al.2012). The black triangles and squares show locations of the TIPAGE seismic network and the GFZ Task Force seismic stations, respectively (see also main text). The white box shows extents of Figs 2–5.

The Nura earthquake was recorded by a temporary seismic network deployed by the Tien Shan-Pamir Geodynamic Program (TIPAGE; Krumbiegel et al. 2011; Mechie et al. 2012; Schneider et al. 2013; Sippl et al. 2013) and the Earthquake Task Force group of GFZ Potsdam (German Research Centre for Geoscience). Using these data, Kalmetieva et al. (2009) located the main shock and some aftershocks along the NE–SW striking Irkeshtam fault (IrkF), which was thought to have ruptured during this earthquake. The fault is exposed close to Nura village (Fig. 1). In contrast to Kalmetieva et al. (2009), Krumbiegel et al. (2011) and Sippl et al. (2013) located the Nura main shock at a shallow centroid depth of 4 km along the east–west striking Pamir Frontal thrust (PFT; Fig. 2). Their main shock location suggests that the Nura earthquake ruptured part of the PFT, instead of the IrkF. This assessment is further supported by their moment tensor solution pointing to a clear east–west oriented fault plane related to a thrust earthquake. Because of the discrepancies in locating the Nura earthquake and the complex structural setting of this region, our remote sensing and field-based study investigates the locus of the faulting and the corresponding surface expression of this earthquake.

We combined SAR remote sensing techniques with seismicity data, tectonic and geological interpretations, and geophysical modelling. We apply the InSAR technique using SAR images from ALOS and ENVISAT satellites, and pixel offset techniques in the ALOS amplitude images to measure surface displacements. Using this approach, we provide surface displacement maps with different line-of-sight (LOS) projections of the 3-D surface displacement (e.g. Wright et al. 2004; Fialko et al. 2005). We also present recently acquired field data of the Nura earthquake surface rupture. Our new data set provides an excellent opportunity for understanding the active structures of the leading deformation front of the eastern part of the northernmost part of the Pamir, a hitherto poorly studied region. With the seismological results and our measured surface displacement and field data, we characterize the faults that were active during the Nura earthquake, using elastic fault modelling (Okada 1985). With this combined information, we provide additional information on earthquake source parameters to that gained in previous seismological studies. It allows us to define the geometry of the ruptured faults at depth and to determine the contractional nature of the strain partitioning in the eastern Trans Alai.

2.2 SEISMOTECTONIC SETTING OF THE REGION

2.2.1 Tectonic setting

The Pamir-Alai region constitutes the collision zone between two mountain systems, the southwestern Tien Shan and the northern Pamir (Fig. 1). The Tien Shan mountains form several ranges that extend approximately 2500 km from east to west (Fig. 1). They are transected into the northeastern and southwestern Tien Shan by the almost 800-km-long NW-SE striking Talas-Fergana fault, a major right-lateral strike-slip fault (Molnar et al. 1973; Burtman & Molnar 1993; Burtman 2000; Korjenkov et al. 2012). The contact zone between Tien Shan and Pamir is characterized by generally east–west trending mountain ranges: the Alai range in the southern Tien Shan to the south the Alai valley and the Trans Alai range (Zaalai) in the northern Pamir (Fig. 1).

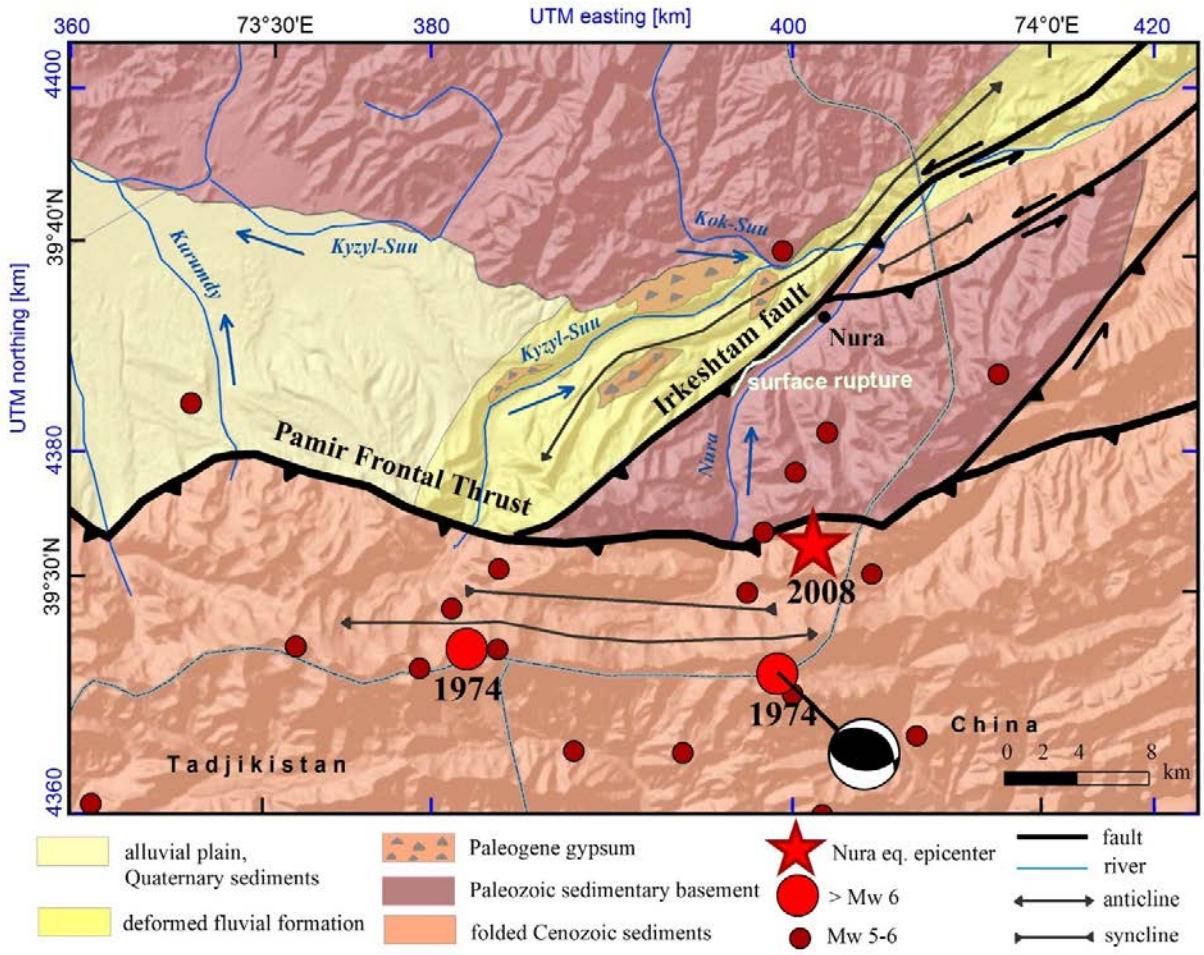

Figure 2. Tectonic and geological map of the eastern Pamir-Tien Shan region from the geological map of 1958 (1:200.000), modified according to our field observations and marked with the surface rupture trace (white line, see also Fig. 6). The regional seismicity is taken from the NEIC catalogue for the years 1973–2011 and the moment tensor of the large 1974 earthquake from Fan et al.(1994). The blue arrows show flow direction of the rivers.

Shortening and uplift of the Trans Alai began during the Neogene (Molnar et al. 1973; Burtman & Molnar 1993; Arrowsmith& Strecker 1999; Burtman 2000; Coutand et al. 2002) and has continued until the present-day. Fault scarps at the Trans Alai mountain front attest to protracted shortening during the Quaternary (Strecker et al. 1995; Arrowsmith & Strecker 1999). The main N–S shortening between the Pamir and Tien Shan is concentrated in the Trans Alai with estimated rates from GPS data of 10–15 mm/yr (Reigber et al. 2001; Yang et al. 2008; Mohadjer et al. 2010; Zubovich et al. 2010). Offsets of Holocene terrace deposits along the Trans Alai mountain front suggest that a large part of this regional shortening is accommodated through slip along the south-dipping Main Pamir and the PFTs (Fig. 1; Strecker et al. 1995; Arrowsmith & Strecker 1999). Both faults are surface manifestations of the south-directed intracontinental Alai subduction zone (Burtman & Molnar 1993; Sobel et al. 2011, 2013). The active structures in the Trans Alai thus account for half of the shortening between the Pamir and Eurasia (Li Tao et al. 2012).

Our study area is located at the far eastern end of the Alai valley and corresponds to the footwall of the Main Pamir thrust (MPT) at the eastern bend of the orogen, where the PFT transitions toward a number of SW–NE striking structures that are an integral part of the orogenic wedge of the collision zone between the Trans Alai and the Tien Shan (Figs 1 and 2). The rock units exposed in the Nura region, integrating the Kyzyl-Suu river basin, include folded and thrusted Neogene to Quaternary strata (Nikonov et al. 1983, Fig. 2). The faults and folds in the hanging wall of the PFT and 20 km east of the Nura village are associated with an evaporitic detachment and integrate shallow-marine and non-marine Paleogene sediments (Dan & Terry 1985). A Paleocene gypsum layer is exposed at the junction of the Kok-Suu and the Kyzyl-Suu rivers with an average thickness of approximately 200 m. Here it thrusts over Eocene silt and sandstones (Nikonov et al. 1983). We observed gypsum exposures also north of and along the IrkF, which emphasizes the importance of evaporites in this tectonic setting. The tectonic province at the eastern closure of the Alai valley also forms a tectonically controlled drainage divide between the Tajik basin in the west of the Pamir and the Tarim basin in the east (Fig. 1), highlighting the role of active tectonism in the landscape evolution of this region.

2.2.2 Regional seismicity and the Nura 2008 earthquake

The MPT and the PFT are characterized by frequent seismicity associated with the southward subduction of the Eurasian continental crust. In the National Earthquake Information Center (NEIC, United States Geological Survey) catalogue, approximately 267 earthquakes have been recorded with magnitudes of four and larger, between 1973 and 2011 along the eastern edge of the Alai valley (between 73.E, 39.67.N and 74.E, 39.17.N). Eighty per cent of these events are at depths of less than 40 km.

During the last five decades apart from the 2008 Nura earthquake only two other large earthquakes have occur red in the region: in 1974 the Markansu earthquake and an aftershock of Mw6.1 occur ring on the same day (Fig. 2). The 1974 earthquakes are characterized by shallow focal depth of less than 7 km and by an oblique thrust mechanism with a component of strike-slip motion (Fig. 2; Fan et al. 1994). In contrast to the large earthquakes in 1974, the Nura event was well recorded by the TIPAGE network, which also had one seismic station in the Nura village (Mechie et al. 2012; Schneider et al. 2013; Sippl et al. 2013). Furthermore, short-period seismic stations close to the epicentre have been deployed 18 d after the earthquake (Krumbiegel et al. 2011; Mechie et al. 2012; Schneider et al. 2013; Sippl et al. 2013) as well as two additional instruments on the Chinese side of the border (Earthquake Administration of Xinjiang Uygur Autonomous Region), which resulted in valuable information about the aftershocks (Fig. 3).

The Nura main shock earthquake was located at a shallow centroid depth of 4 km along the east–west striking PFT, with the main shock moment tensor solution showing a dominant thrust mechanism and only a minor strike-slip component (Krumbiegel et al. 2011, Fig. 3). This suggests that the earthquake ruptured a segment of the PFT (Krumbiegel et al. 2011; Mechie et al. 2012; Schneider et al. 2013; Sippl et al. 2013) (Fig. 3). In addition, two aftershocks with Mw> 5 occur red on the PFT, whereas other moderate-sized aftershocks occur red farther northeast, aligning closely with topographic features (Fig. 3). Based on network criteria Krumbiegel et al. (2011) estimated the absolute location precision to be better than 3 km, while relative location errors are significantly smaller.

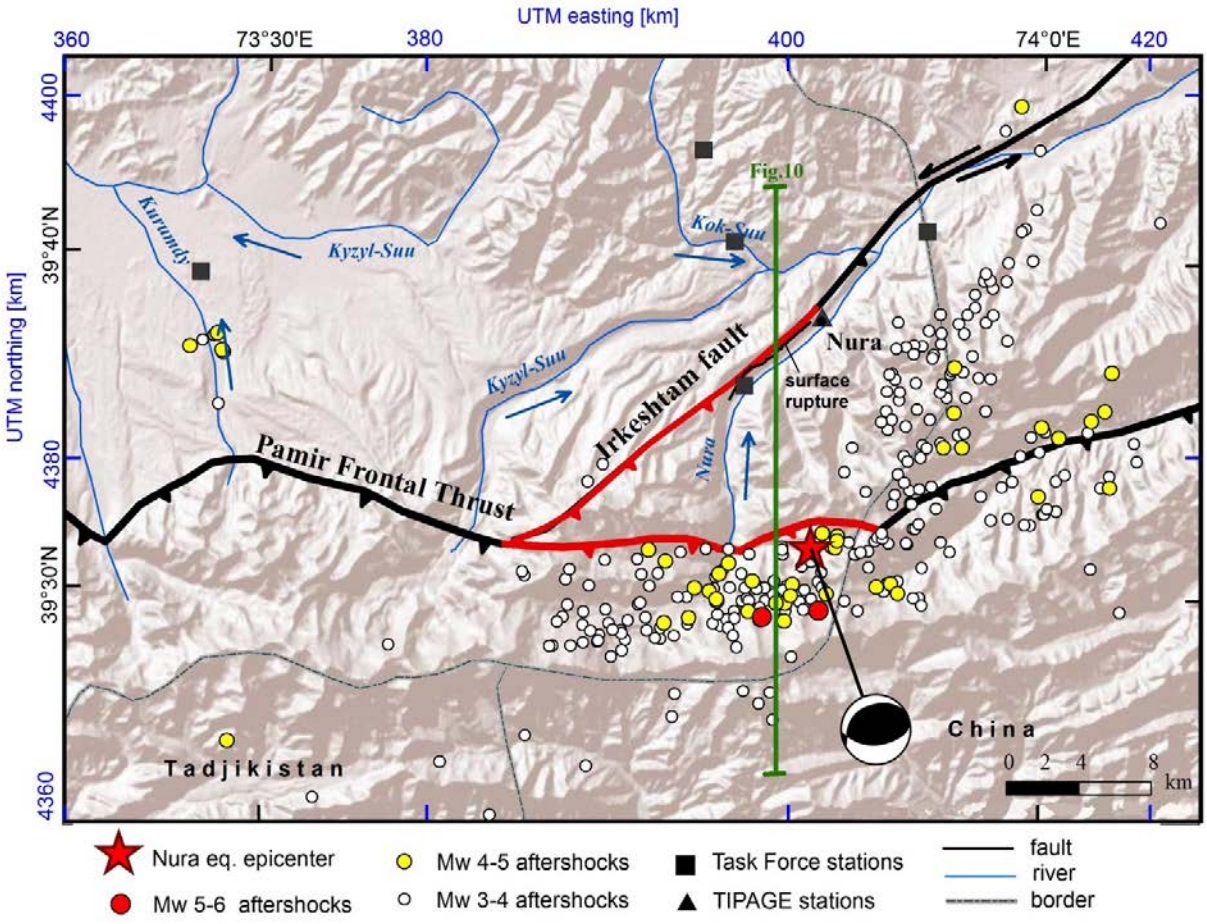

Figure 3. Main and aftershock location map of the Nura region with the activated (red colour) Pamir Frontal thrust (PFT) and the Irkeshtam fault (IrkF). The main shock (red star) moment tensor and aftershock locations are after Krumbiegel et al. (2011). The marked profile line (solid green line) is the cross-section of the postulated fault geometry at depth for the PFT and the IrkF shown in Fig. 10.

2.3 SURFACE DISPLACEMENT MEASUREMENTS

SAR data for the Nura epicentral region are available from the ALOS (PALSAR L-band sensor with = 23.6 cm) and ENVISAT (ASAR C-band sensor with = 5.6 cm) satellites. We processed 16 ascending ALOS and seven descending ENVISAT images spanning from 2008 May 8 until 2009 August 20, and we formed differential interferograms and pixel offset maps. Ideally, by combining ascending and descending sets of observations and pixel offsets, 3-D displacements can be measured in the affected area (Wright et al. 2004; Fialko et al. 2005). To provide ground

truthing to the SAR-based surface displacement maps, we complement our remote sensing investigations by structural field observations guided by our SAR results.

2.3.1 InSAR and pixel offset processing

We processed 16 ascending ALOS images and 7 ENVISAT images, with perpendicular baselines of less than 300 m and temporal baselines of less than 14 months using the SARscape and the ROIPAC (Rosen et al. 2004)software packages (see Annex 1, Tables S1 and S2). We then selected one interferogram from each look direction for further analysis (Table 1). The chosen interferogram pairs provided optimal coherence and had short perpendicular baselines, which are 91 m for the ALOS and 131 m for the ENVISAT image pairs (Table 1).

Table 1. SAR scene acquisition information of the analysed interferograms.

Pass	**Track**	**Frame**	**Master**	**Slave**	**B⊥ [m]**	**Incidence angle [degree]**
ALOS/PALSAR						
Asc	527	780	2008/07/02	2009/08/20	90.01	34.3
ENVISAT						
Desc	234	2817	2008/05/08	2009/05/28	131.494	23
B⊥ : perpendicular baseline between the orbits in meters.						

For the ALOS interferogram, we used multilook factors of 1 in the range direction and 5 in the azimuth direction, which resulted in a ground resolution of approximately 20 m × 20 m. To increase the low signal-to-noise ratio in the ENVISAT interferograms, we applied multi-looking factors of 16 in the range direction and 80 in the azimuth direction, which resulted in approximately 320 m of range ground resolution. We removed the topographic phase contribution in the interferograms by using the SRTM DEM data at 90 m resolution (Fan et al. 1994). The resulting differential interferograms were then filtered using an adaptive filter (Goldstein & Werner 1998). For the phase unwrapping, to resolve the 2π-phase ambiguity of the interferograms, we used the Snaphu software package (Chen & Zebker 2001). Noisy and uncorrelated areas, layovers, and unwrapping errors were masked out. Finally, we transform the unwrapped data from the satellite azimuth-range coordinates to ground coordinates, specifically, Universal Transverse Mercator (UTM) coordinates, and we retrieved the surface displacement maps in a cartographic reference frame (Fig. 4).

In addition to SAR interferometry, we used pixel offset estimates between amplitude images of the coseismic data pairs (Table 1) in the range and azimuth directions to measure ground displacements (Fig. 5). These pixel offsets were determined through a cross correlation of small subsets in the image, which provided measures of pixel shifts between the two images at a subpixel resolution. Pixel offset measurements in the image range direction complement the interferometric displacement measurements because they give the component of displacement in slant range direction (Michel & Rignot 1999), the same projection as the ALOS interferogram, but they do not suffer from phase ambiguity (Fig. 5). Pixel offset measurements in the azimuth direction, however, add a new displacement component that is purely horizontal in the satellite's flight direction. We estimated the offsets with window sizes of 64 and 128 pixels in the range direction and the azimuth direction, respectively.

The range pixel offsets show sharp changes of the surface displacement at the IrkF (Fig. 5). Here we measure up to 1.5 m of displacement south of the IrkF. In the azimuth-pixel offsets, the observed displacement pattern shows a clear left-lateral component of movement along the IrkF (Fig. 5). The difference in the horizontal motion across this oblique thrust fault reaches 2 m.

2.3.2 Results of the surface displacement measurements

Measuring the coseismic surface displacement using InSAR is challenging in this region of high topographic relief because of abundant areas of layover and all-season snow coverage. In this case, the ALOS data perform better than the ENVISAT data (Fig. 4). The larger average radar-beam incidence angle of 39 emitted by the ALOS SAR sensor reduces layover in the interferograms compared to the 23 incidence angle of the ENVISAT SAR radar beam.

Furthermore, the L-band data are less sensitive to small changes on Earth's surface relative to the C-band SAR data. Therefore, the L-band data preserve the coherence of the interferometric phase and backscatter characteristics over longer time spans. Although the ENVISAT data seem to be less suitable for measuring surface displacements in this environment, information gained from the different look angle in descending orbit is important and complements the ascending orbit data from ALOS (Wright et al. 2004).

In the ascending ALOS interferograms, we observe clear coseismic surface displacements mainly north of the PFT and at the IrkF (Fig. 4, top panel). We measure widespread motion

away from the sensor of about –24 cm and a strong, more localized signal of movement towards the sensor in the northeastern part of the IrkF of about 48 cm. In the epicentral region more south large positive LOS displacements can be observed, but the phase coherence is not well enough preserved to reliably unwrap the interferometric phase for quantitative measures. In the descending ENVISAT interferogram the phase coherence is generally low and again only in the area north of the IrkF measurements of the surface displacements are possible. We here observe widespread motion towards the sensor with up to 6cm of LOS displacement (Fig. 4, bottom panel). The large differences in the measured LOS displacements between the ascending and descending images are to be expected only for a considerable amount of E–W horizontal surface displacement.

In both interferograms the phase gradients increase from the north towards the IrkF. At the fault gradual phase changes become disrupted and/or the phase coherence is lost abruptly. These observations point to surface rupture. South of the PFT far-field surface displacements can be observed in both interferograms. They show slight positive to negative phase shift.

The pixel offsets add new information to our displacements measured by using InSAR. First, range and azimuth pixel offsets give coherent displacement measurements for the area south of the IrkF, where no InSAR data are available (Fig. 5). Secondly, azimuth pixel offsets provide another and purely horizontal component of the displacement field in an approximately N–S direction. The range pixel offsets show positive LOS displacements south of the IrkF of up to 2 m, pointing to an upward and/or westward motion. Directly at the IrkF and towards north the values drop to zero and less (Fig. 5, left-hand panel). The azimuth pixel offsets also give positive displacements south of the IrkF, reaching values of up to 2 m and showing a northward displacement (Fig. 5, right-hand panel). The values again drop rapidly across the IrkF and become negative. The observed step in the pixel offsets is a feature that extends continuously for approximately 25 km in a northeast–southwest direction, which aligns with the IrkF as mapped in the regional geological maps (Fig. 2). The azimuth pixel offset measurements are affected by strong and wavelike artifacts, that are known to occur for azimuth offset measurements using L-band SAR data (e.g. Gray et al. 2000). These errors are caused by heterogeneities in the ionosphere, which behaves dispersive for radar waves. We describe the treatment of data errors in more detail in Section 4.1 and in the Supporting Information (Annex 1 Fig. S1).

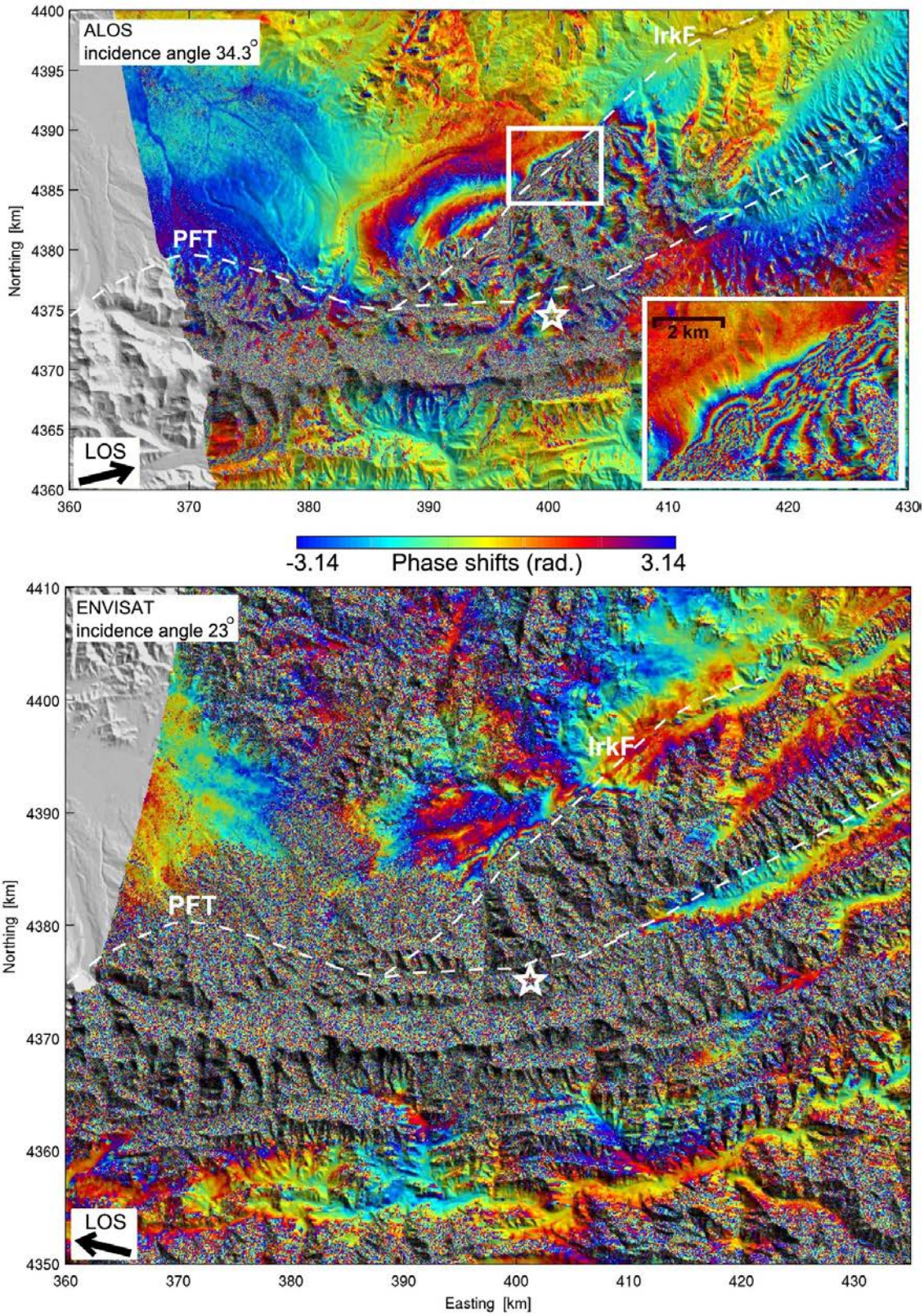

Figure 4. ALOS (top panel) and ENVISAT (bottom panel) interferograms in wrapped phase and over a shaded relief show the line-of-sight (LOS, black arrows) surface displacement close to the Nura earthquake epicentre (white star). White dashed lines outline the Pamir Frontal thrust (PFT) and the Irkeshtam fault (IrkF). The inset in the top panel shows an enlarged image of the in white outlined area, where steps in the interferometric phase values point to surface rupture.

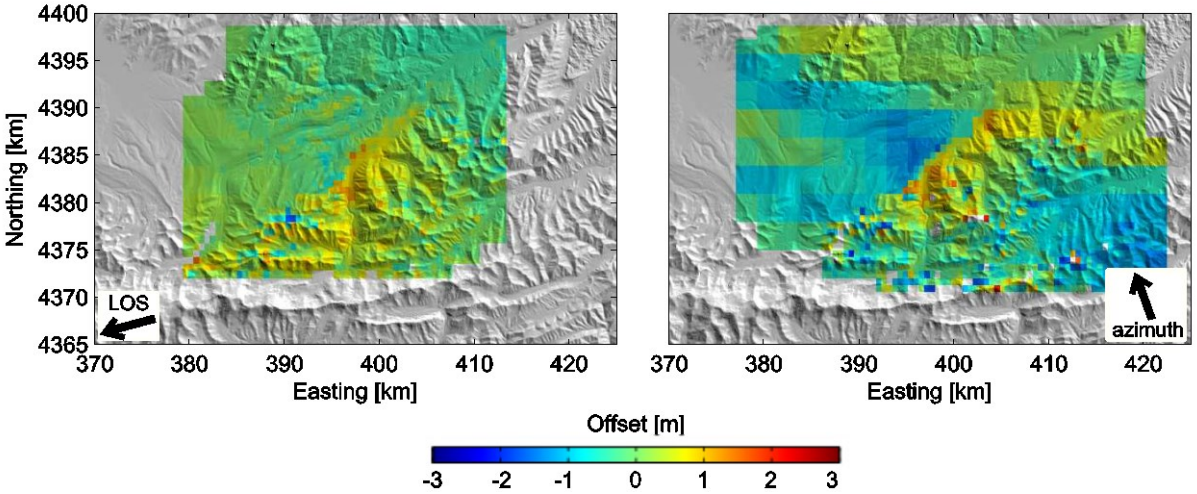

Figure 5. ALOS pixel offset measurements. The range offsets are in the slant range direction (left-hand panel, black arrow). Azimuth offsets give purely horizontal surface displacements in the direction parallel to the satellite flight direction (right-hand panel, black arrow).

2.3.3 Field observations

Our field work in the fall of 2012 aimed at ground truthing SAR displacement measurements through mapping of the detected surface rupture of the Nura earthquake. The metre-scale displacements and the sharp discontinuities for a distance of approximately 25 km as defined in our SAR data analysis (Section 3.2) suggest that surface ruptures should be observable in the field.

Information given by locals in combination with our remote sensing data helped to identify prominent, 7-km-long ground ruptures southwest of the Nura settlement on the northwest side of the Nura the river, which here flows parallel to the IrkF (Fig. 6). These ruptures constitute steep scarps and fractures in the soil-mantled surface, with offsets of up to 80 cm (Fig. 6b). Furthermore, in these areas we found a number of fractured erratic glacial boulders that had formed transgranular extension fractures parallel to the surface trace of the rupture (Fig. 6c). Importantly, in addition to the clear vertical offsets associated with the fractures, we were able to observe left lateral displacements along the fractures. These kinematic markers are in excellent agreement with the SAR-measured displacements. Further details of these structural geologic and geomorphologic field investigations are beyond the framework of this study and will be presented in a separate study.

Another important and relevant observation during the field investigations was the observation of exposed evaporite sequences along the IrkF. Along the south side of a road between Nura village and the Chinese border, gypsum is observed within the Eocene stratigraphic sequence. This setting is similar to the better-documented stratigraphic sections farther east, on the Chinese side of the border, in the westernmost Tarim basin (Sobel et al. 2011, 2013). A stratigraphic correlation between these sequences is supported by the presence of Eocene fossils.

The presence of gypsum in the deformation zone may affect the overall rheology and therefore influence the tectonic pattern, the mode of thrust stacking and the nature of the strain partitioning along the strike. The extensive presence of evaporates may also have a major impact on the mechanics of coseismic deformation.

Based on these findings, we posit that the PFT and the IrkF are rooted in a common detachment at depth (Fig. 10). This explains why they were apparently activated during the same earthquake. We use these observations and considerations to infer a potential geometry of the PFT and the IrkF at depth (Fig. 10) and to further explore the nature of this geometry in non-linear and elastic fault modelling.

2.4 FAULT MODELLING

Using the InSAR surface displacements and the pixel offset measurements, we can potentially put constraints on the fault orientation at depth, the spatial extent, and the fault through non-linear fault modelling. Here we attempt to test if our hypothesis of the rupture continuation and rupture mechanisms (Fig. 10) are consistent with the observed surface displacement pattern at the PFT and the IrkF. In this area it is difficult to measure the surface displacement with sufficient spatial detail and with observations from different look angles to optimally constrain a fault model. We reach the best possible coverage of displacement measurements through the combination of different data sets: interferometric ascending ALOS L-band data and descending ENVISAT C-band data, as well as ALOS range and azimuth pixel offset measurements. While individual data sets are all affected by noise that differs in spatial

structure and strength, we consider the variable data quality in the fault modelling through data weighting based on empirically estimated weighting factors as described below.

Figure 6. Field observations of the surface rupture of the Nura earthquake in September 2012, which could be followed along 7 km (a). Surface trace offsets reached a maximum vertical offset of about 80 cm (b) and clear left-lateral motion (c). Photos from Edward Sobel.

2.4.1 Data subsampling and weighting

Our data combination led to a large amount of data points that we could not implement for further digital data analysis. Therefore, we subsample the frequently smooth displacement signal by using the well-established Quadtree Algorithm (J´onsson et al. 2002). Quadtree subsampling enables a spatially irregular subsampling without loss of information and with further noise reduction. From a multimillion point data set we keep only a total number of 3177 points for all four data sets.

The different data sets to be combined have widely differing quality with respect to their signal-to-noise ratio and the amount of correlated data errors (Hanssen 2001), which depends on the sensor wavelength, the acquisition dates (e.g. with or without snow cover) and the temporal baseline between image pairs. To account for the variability of the error content, we form a data weighting matrix from empirically estimated data error variances and covariances. For this error estimation, we use sample variograms and sample covariograms from which we infer the error variances and covariance functions of the individual data sets as described in Sudhaus &J´onsson (2009). A special case here are the azimuth offsets that show a strong anisotropic error component. Here, we apply a simplified method for the error estimation in the presence of anisotropic noise (Knospe & J´onsson 2010) that considers an azimuthal dependence of the error-correlation length. We then combine all estimated variances and covariance functions to a single variance–covariance matrix used in the fault model optimization (for details see Supporting Information, Fig. S1). In this way, based on the data quality, we balance the individual data points in the fault model optimization, which has been shown to stabilize and improve the modelling results in highly non-linear inverse problems (Sudhaus & J´onsson 2009; Duputel et al. 2012).

2.4.2 Fault model set-up and optimization approach

For the fault modelling we use the widely applied rectangular dislocation model (Okada, 1985). This model represents the Earth's crust with a homogeneous, purely elastic half-space and represents the embedded faults through planar, rectangular dislocations with a uniform fault slip. Given this model set-up, the formulations in Okada (1985) allow for analytical calculations of displacements at the surface. Although this model simplifies the faulting processes at depth,

it is widely used in studies on earthquake sources, for example, Nissen et al. (2007), J´onsson et al. (2002) and Fialko et al. (2005). The rectangular dislocation model is useful because we often lack information about the actual material heterogeneities and structural complexities of the faults at depth, which is the case in our study, and the forward computation of the fault models is fast.

However, even for such a simplified model set-up, the estimation of fault properties, for example, fault location, orientation and slip on the fault, is a highly non-linear inverse problem. We approach it by using a direct search method (Sambridge 1999). Direct search entails searching a set of physically possible and geologically meaningful models that best reproduce the observed surface displacement data. Specifically, we use an evolutionary algorithm (Sambridge 1999), which mimics a natural selection process (‘survival of the fittest’).

Table 2. Fault model parameters for the Nura earthquake estimated from surface displacement data. Fixed model parameter values are marked with ’*’, tightly constrained model parameters are marked with ’(*)’. The east, north and depth values give the location of the midpoint of the upper fault edge in UTM coordinates (UTM zone 43).

Parameters	**Pamir Frontal thrust**		**Irkeshtam 1 segment**		**Irkeshtam 2 segment**	
	optimum	**ranges**	**optimum**	**ranges**	**optimum**	**ranges**
Easting (km)	395*		400*		395.5*	
Northing (km)	4376*		4386.5*		4381.5*	
Top depth (km)	0	[0, 2]	0.5	[0, 2]	0.1	[0, 2]
Bottom depth (km)	2.4		8.5		5.8	
Length (km)	13.6	[10, 16]	7*		6*	
Width (km)	14	[10, 16]	10(*)	[9,11]	8(*)	[7, 10]
Strike (deg)	83*		51*		43*	
Dip (deg)	80	[40, 90]	37	[20, 70]	44	[10, 90]
Strike-slip (m)	0	[0, 2]	1	[0, 2]	1.3	[0, 2]
Dip-slip (m)	0.9	[0, 3]	1.6	[0, 3]	2	[0, 3]
Rake (deg)	90		57		57	

To represent the coseismically activated faults as identified by seismological studies and in the surface displacement data (Fig. 10) with rectangular dislocations, we chose to use three dislocation planes. One of these segments represents the rupture at the PFT and two segments represent the faulting at the IrkF. For the segment at the PFT, we fix the location and fault strike based on the seismological moment tensor characteristics of the Nura earthquake (Section 2.2 and Table 2). The free model parameters in the optimization for this segment are the dimensions

of the fault segment, length and width, the depth of the fault, the fault dip and fault slip along strike and down dip. The relatively tight parameters ranges for fault length and width are chosen based on moment scaling relations (Mai & Beroza 2000). For the fault-model segments along the IrkF, we place constraints from the pixel offset analysis and our field observations, and we fix the fault location, the fault strike, and the segment length in the optimization. Also, we require the same rake for both IrkF segments. Furthermore, we place tight constraints on the poorly resolved fault width based on scaling relations (Mai & Beroza 2000). The remaining model parameters, the depth, the fault dip, the strike-slip, and the dip-slip components, are part of the model parameter space in the optimization (Table 2). With these constraints on the three fault segments we arrive at 14 fault model parameters to be optimized within the given parameter ranges (Table 2). While the common rake constrain on the IrkF segments reduced the model parameter independence to some extent. For the elastic half-space we chose a Poisson's ratio of 0.29, since we consider relatively fast movements and therefore undrained conditions in the material (Peltzer at al. 1992; J´onsson et al. 2003). In addition to the fault-model and medium parameters, we include data ambiguity parameters that account for common offsets, range, and azimuth linear ramps in the surface displacement measurements; we use three ambiguity parameters per data set, which amounts to 12 additional model parameters.

For the optimization, in our implementation of an evolutionary algorithm, we first randomly pick a set of 200 candidate fault models from the described parameter space. From these candidate models we then chose the best performing half of the models. The criterion for the selection is the misfit between the predicted and the observed data, with misfit function being the l2-norm of the weighted data residuals. These selected models are commonly called the parent generation. The parent models are then used to seed a next model generation, the offspring, by recombining the model parameters to form new models and by altering the parameters of these new models to some extend, which is called mutation. In this way we from 200 offspring models and again do a selection as before to find the next parent generation. We tested different numbers for the size of the parent and offspring populations as well as for the number of generations. We found that we obtain stable solutions for the given population sizes and 500 generations.

2.4.3 Fault model for the Nura earthquake

Our optimization results in a fault model in which the PFT has a steep southward dip of 80^0 involving 0.9 m of fault dip-slip and negligible strike-slip (Fig. 7). The eastern part of the IrkF

dips south with an angle of 37^0 and becomes steeper to approximately 44^0 towards the west. The slip estimates at the IrkF's first and second segment give an oblique thrust mechanism with 1.6 and 2 m of fault dip-slip, and 1 and 1.3 m of left-lateral fault strike-slip, respectively (Table 2). The slip rake, calculated based on the obtained dip-slip and strike-slip components, is 90^0 for the PFT and 57^0 for the IrkF segments (Table 2). In combination, the optimum faults form a complex structure with reverse and strike-slip faulting.

The fit of the predicted surface displacements to the observed ones is not entirely satisfying. Obvious is the underestimation of the surface displacements in the hanging wall of the IrkF (Fig. 8). The footwall displacements at the PFT, including the rupture at the IrkF, are generally well modelled as is the far-field in more than 20 km distance from the epicentre (Figs. 7 and 8).

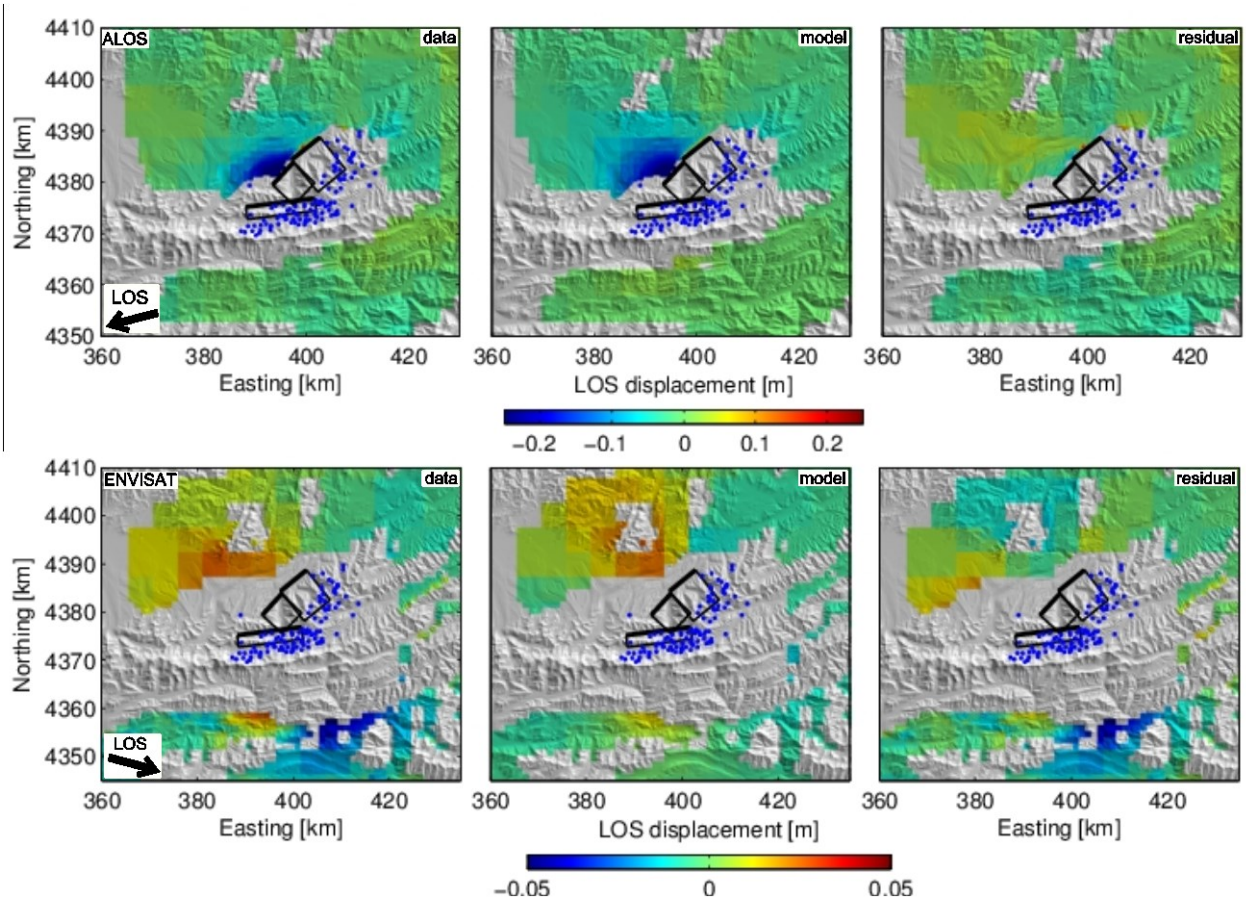

Figure 7. InSAR data model results. ALOS (top panels) and ENVISAT (bottom panels) observed data (left-hand panels), predicted data (middle panels) and residuals (right-hand panels) for the three-segments optimum model representing the Pamir Frontal thrust and the Irkeshtam fault. The map-projected segments are marked in solid black lines, thick lines mark the upper edge. Aftershock locations are shown with blue dots.

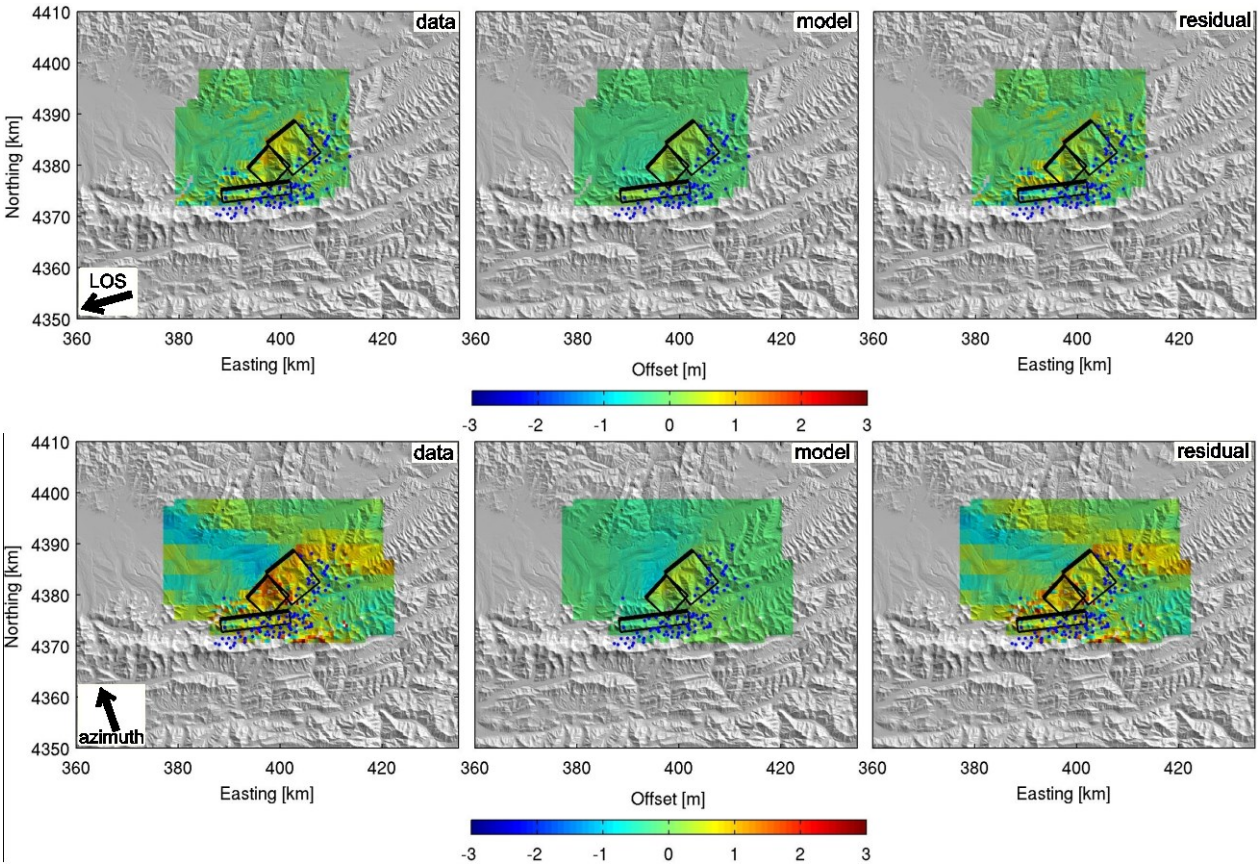

Figure 8. Pixel offset model results. ALOS range (top panels) and azimuth (bottom panels) observed pixel offsets (left-hand panels), predicted pixel offsets (middle panels) and residuals (right-hand panels) for the three-segments optimum model representing the Pamir Frontal thrust and the Irkeshtam fault. The map-projected segments are marked in solid black lines, thick lines mark the upper edge. Aftershock locations are shown with blue dots.

2.5 DISCUSSION

The SAR surface displacement measurements of the Nura earthquake and their analysis reveal three important results. First, the Nura earthquake nucleated at the PFT, where a major part of coseismic deformation took place in the footwall. Secondly, we observe surface ruptures along the IrkF to the north of the PFT, where no aftershock activity is observed. Thirdly, we find generally larger surface displacements in the hanging wall of the IrkF than in its footwall (Figs. 4 and 5). There is a complex inter play of active faults in the Nura region, which we discuss in the following sections.

2.5.1 Fault kinematics in the Nura region

The Nura earthquake activated the E–W striking PFT and the SW– NE striking IrkF. Along the active part of the PFT we found evidence for thrust faulting, which is consistent with the seismological analysis of the main shock and the aftershock sequence (Krumbiegel et al. 2011). For the IrkF, we found evidence for oblique thrusting, with a significant left-lateral strike-slip component. These observations clearly document that strain partitioning must have taken place between the two faults. From the fault geometry and differential uplift at the surface, we conclude that the PFT and the IrkF likely share a common root at depth. This hypothesis was strengthened by the fault modelling, which requires a steeper fault geometry for the PFT than for the IrkF. The faults therefore seem to form part of an imbricate thrust system (Fig. 10). This is important because it supports the view that the current mountain front of the Trans Alai is part of a northward-advancing thrust wedge that successively involves sectors of the Trans Alai piedmont (e.g. Coutand et al. 2002; Strecker et al. 2003; Sobel et al. 2013).

We observe that the hanging wall of the IrkF accommodates a large part of the N–S contraction relative to the N–S contraction at the PFT. The IrkF is the focus of the highest surface displacement evident from InSAR and pixel-offset measurements (Figs 4 and 5) as well as mapped surface ruptures in the field (Fig. 6). While there is no direct evidence from the seismological data that the IrkF was coseismically active, the transgranular fractures in the boulders found at the fault surface trace (Fig. 6) point to a sudden rupture with high-frequency seismic waves. Because no aftershocks have been observed near the IrkF (Krumbiegel et al. 2011), we conclude that the rupture of the IrkF was coseismic and concur rent with the Nura main shock.

Moreover, the NE–SW strike of the IrkF, which deviates from the E–W dominated structural pattern west of the Nura region, combined with a significant left-lateral strike-slip component on the fault seems to indicate a general pattern of deformation in this sector of the orogenic front (Fig. 3; Krumbiegel et al. 2011; Mechie et al. 2012; Schneider et al. 2013; Sippl et al. 2013). The observed strain partitioning of the N–S contraction into northward thrusting on the E–W striking thrusts and frontal, NE–SW striking sinistrally oblique thrusting appears to be the predominant tectonic mode.

2.5.2 Fault mechanics and moment estimates

We estimated the orientation and the fault mechanisms of the active fault segments at depth through analytical dislocation modelling. In this model approach, we assume uniform slip on the faults and a homogeneous elastic medium. We further constrained the location and orientation of the fault at the surface based on our combined data set. We find a qualitatively good agreement between the pattern of the observed and the predicted surface displacements. As described in Section 4.3, however, at the hanging wall of the IrkF the predicted pixel offsets from our best model do not reach the large surface displacement values as measured, with discrepancies amounting to 1 m. Therefore, the model results on the fault dip and slip need to be taken with care, since the estimated model parameters could be biased to an unknown extent. To increase the displacement predictions for the hanging wall of the IrkF, a larger fault slip and/or a more shallow fault dip would be needed. We find that this leads to significant changes in the predicted footwall surface displacements, which are well explained with our optimal model.

The reason for this data-model-mismatch resulting from the purely kinematic rectangular dislocation models might be that this model forces symmetric fault slips on both sides of the dislocation, each accounting for half of the total slip. Additionally, other simplifications of the chosen dislocation model could contribute to the apparent data-model-mismatch, including the oversimplified fault geometry through forced planar dislocations with a uniform slip. We think, however, that the influences of the oversimplified dislocations are second-order to an oversimplified material, as the parameters of the dislocations are part of the optimization, which provides estimates of average values. In contrast, the material properties are assumed before any modelling.

The systematic underestimation of the surface displacements at the hanging wall may be attributed either to different material properties on both sides of the fault, with different elastic proper ties (e.g. Nissen et al. 2007), or to an asymmetric slip with a larger slip on the hanging-wall side of the IrkF compared to the PFT, facilitated by a weak fault zone. We think the first possible explanation of less rigid hanging wall material than the footwall material is not likely because at the IrkF Paleozoic rocks thrust over the much younger, probably less consolidated

and less competent basin sediments. The alternative explanation, that there is a partially non-elastic faulting process, seems to be the more plausible one.

We tested whether or not the hypothesis of asymmetric slip on the fault is compatible with our model results and if the systematic model residuals the IrkF hanging wall would be reduced. For this test we increased the optimum slip values of the otherwise fixed IrkF model segments by factors in step-wise manner. We then evaluated the resulting models based on the data variance reduction, while distinguishing the IrkF footwall and hanging wall areas (Fig. 9). For increased fault slips by factors of 1.3–1.5 with respect to the optimum fault slip we find systematically larger variance reductions of the hanging wall data whereas the variance reductions of the footwall data systematically decrease. A possible explanation for this behavior could be a very weak fault zone. Close to the outcrop of the IrkF gypsum and salt are exposed, which are otherwise interstratified in the overthrusted basin sediments (see Section 3.3). With approximately 10 GPa, salt and gypsum have only about a third of the rigidity that is usually assumed for the average crustal rocks (Robertson et al. 1958; Bell 1981). If these weak materials were associated with a fault zone, they could be subject to inelastic deformation and effectively decrease the friction of the fault.

Moment magnitude estimates based on our model provide slightly larger values than the seismically inferred. The moment magnitude, M_w, is calculated via the geodetic moment through the equation: $M_w = 2/3M_0 - 6.03$ (Kanamori 1977), where $M_0 = \mu A\overline{D}$, and where μ is the assumed average crustal rigidity of 30 GPa, A is the fault area and $\overline{D}$ is the average slip on the fault. With our optimum model we derive geodetic moments of 4.99×10^{18}Nm for the PFT, corresponding to M_w6.43, and a larger geodetic moment of 5.43×10^{18}Nm for the IrkF, which corresponds to M_w6.46. Taken together, the moments for both faults add up to Mw6.65 for the Nura earthquake, which is similar to the seismically estimated M_w6.6 (e.g. Krumbiegel et al. 2011). More indications for a coseismic rupture with little fault friction at the IrkF could be obtained from a comparison of M_w and the energy magnitude, M_e (Choy & Boatwright 1995). While for many earthquakes, M_w and M_e are similar, low-friction earthquakes with high stress drops generate high-frequency seismic waves, which add to M_e more strongly than to M_w (e.g. Bormann & Di Giacomo 2011). For the Nura earthquake, the USGS reports M_e7.5, which is significantly larger than the seismic estimate of M_w6.6 (Krumbiegel et al. 2011). Convers & Newman (2011), however, provide a second estimation of M_e6.6, which is as large as M_w.

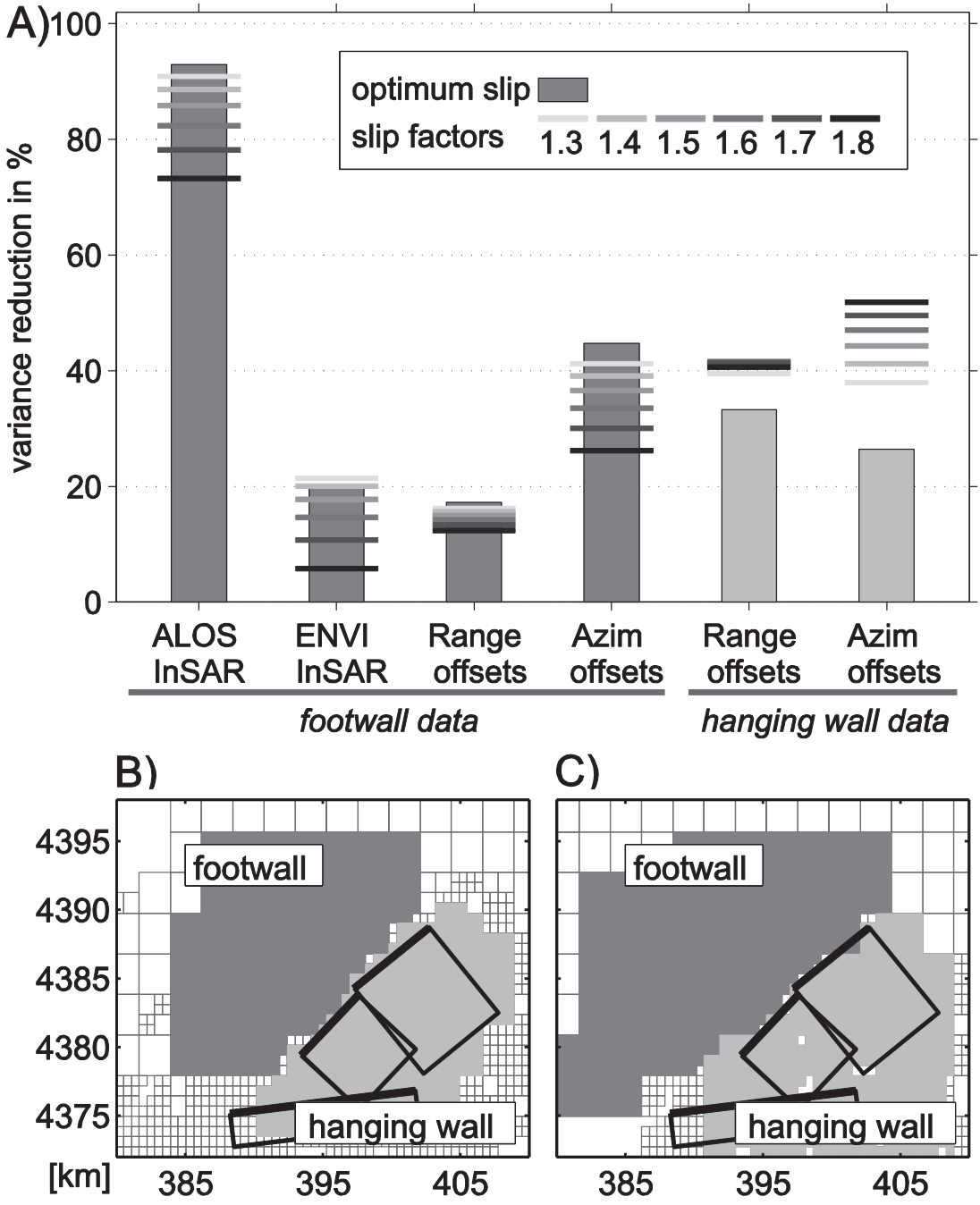

Figure 9. Test of asymmetric slip hypothesis. (a) Bars show the variance reduction through modelling per data set and distinguishing footwall and hanging wall areas of the Irkeshtam fault. The InSAR data sets provide footwall data only, the range and azimuth pixel offset measurements have been spatially divided (see b and c, respectively) into footwall and hangingwall areas. Shaded horizontal lines at each of the bars give the corresponding variance reduction for increased slip on the fault model (geometry kept fixed) for factors of 1.3–1.8.

Concerning the coseismic fault slip at the IrkF, we interpret the fractured boulders along the surface ruptures as important indicators of coseismic behavior of both faults (see Sections 3.3 and 5.1).

However, to infer the fault slip in our modelling, we use the measured surface displacement from the interferograms that span several months of post-seismic time (10 months for the ALOS data and close to 8 months for the ENVISAT data). Therefore, a significant part of the fault slip could have been generated post-seismically, for example, through afterslip (Scholtz 1998). Afterslip is commonly observed in the shallow parts of coseismically activated faults, in which the material properties favor stable sliding (Marone et al. 1991). Unfortunately, the available post-seismic pairs that we processed do not show any significant post-seismic displacements or have a decor related interferometric phase in the area of interest, likely because of snow.

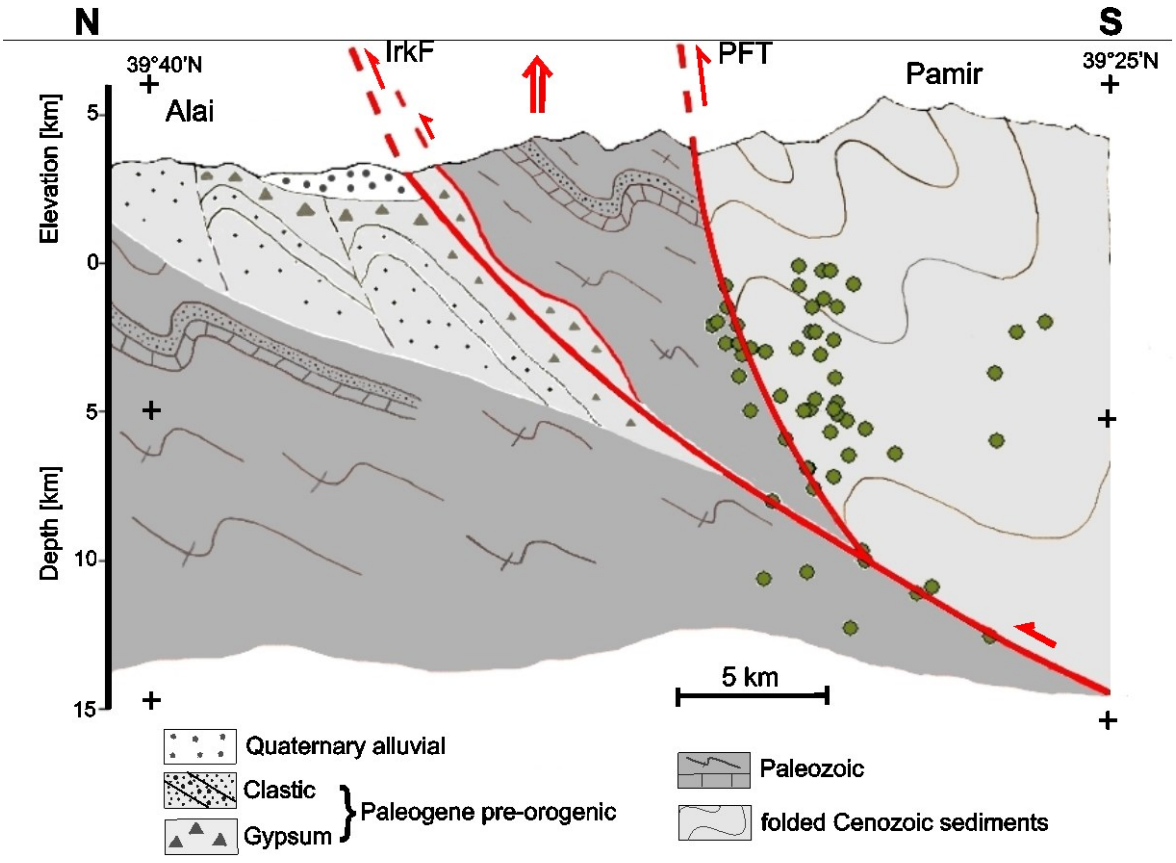

Figure 10. Interpreted cross section (for location see Fig. 3) across active Pamir Frontal thrust (PFT) and Irkeshtam fault (IrkF) with aftershock locations (green circles). For visualization the gypsum layer possibly exaggerated in thickness.

2.5.3 Implications for regional tectonics

From the fault kinematics and the fault mechanics that we have discussed, we form a synthesis of the gathered information and integrate it with the given geology and tectonics of the eastern Pamir-Tien Shan collision zone. Evidently, the Nura earthquake activated a contractional frontal wedge in the footwall of the MPT. The interpretation of the fault geometry and activity as well of the PFT as of the IrkF and the inter play of rock units at depth, are accommodated with the main N–S shortening direction (Fig. 10). The profile shows a distinct change in the lithology across the back-range fault, the PFT, and the front-range fault, the IrkF. At the back-range fault consolidated, folded Cenozoic sediments are upthrusted over Paleozoic basement units. At the front-range fault, Quaternary alluvial and Paleogene pre-orogenic continental sediments have been thrust over and left-laterally displaced to the north east along the IrkF zone, that presents a gypsum dominated tectonic m´elange and thick detachment horizon (Fig. 10). The PFT divides two competent rock units and, therefore, appears to facilitate the nucleation of earthquakes, as evident from the Nura epicentre and main shock location and the aftershock concentration observed there. The IrkF forms a boundary between the more competent rock units of the Paleozoic sediments in the south and the weak rock units of the poorly lithified, gypsum-bearing Paleogene strata in the north (Fig. 10). The northern structures are dominated by intensely folded and up to 2-km-thick Paleogene sediments with a high content of mechanically weak gypsum. Gypsum is inferred to lubricate the fault and to facilitate material transport. Such a scenario would explain the relatively high displacements as measured for the hanging wall structure and the lack of seismicity relating to the IrkF zone. We therefore interpret the IrkF as a rather aseismic d´ecollement.

The presence of thick and mechanically weak layers pose questions concerning earthquake characteristics also elsewhere, such as in the Zagros Simply Folded Belt, Iran (e.g. Nissen et al. 2010; Barnhart & Lohman 2013) and in the Cordillera de la Sal, Chile (Kuhn & Reuther 1999). In the Zagros mountains, seismically and geodetically infer red ruptures of moderate to large earthquakes seem to be systematically displaced to more shallow depths with respect to the volumes outlined by aftershock activity. The situation resembles the presented Irkeshtam rupture and the off-set aftershock sequence of the Nura earthquake. Possibly, the proposed significant role of aseismic slip in the Zagros (Barnhart & Lohman 2013) finds a parallel in the faulting style in the north-eastern footwall of the Pamir.

In the Nura region, the northward motion of the Pamir and its collision with the Tien Shan constitutes a fold-and-thrust belt, in which the thrust wedge has been accreted over detachments (Nikonov et al. 1983). One of these detachments might be responsible for the basement structures of the frontal thrust system and associated structures investigated here, similar to other areas along the Indo-Asian collision, such as the Trans-Indus ranges of Pakistan (e.g. Blisniuk et al. 1996, 1998; Ahmad et al. 2005).

2.6 CONCLUSIONS

In our study, we demonstrate the usefulness of InSAR and pixel offset techniques for measuring surface displacements in combination with geological observations and seismological data to enhance our understanding of active tectonics in a structurally complex continental collision zone. We found that the 2008 Nura earthquake (Mw6.6) ruptured an imbricated thrust system. This thrust system is part of the PFT and constitutes a fold-and-thrust belt in the eastern convex transition of the Trans Alai range, where it collides with the Tien Shan to the north. The IrkF at the deformation front is a moderate-angle d´ecollement fault that seems to be controlled by mechanically weak evaporites lubricating the fault. This fault was coseismically activated by the Nura earthquake, as documented by prominent surface ruptures and fractured boulders along the trace of the rupture; meanwhile, the earthquake nucleated at the back-range PFT. The Nura earthquake thus caused dip-slip thrusting and sinistrally oblique thrusting on the kinematically connected PFT and the IrkF. This event presents an example of coseismic strain partitioning in a tectonically active collision zone, which is characterized by northward orogenic wedge migration toward the Tien Shan mountains.

ACKNOWLEDGEMENTS

We thank Ed Sobel, Gerold Zeilinger and Bolot Moldobekov for their support, high-engagement in the field work and for a very useful discussion on the geology of the region. We also thank Frank Krueger for fruitful discussions on the seismological aspects of this study. We thank Claudia Krumbiegel for the seismic data analysis. Furthermore, we are grateful for the support of Mahdi Motagh, Uli Wetzel and Alexander Mikolaichuk during the early stages of the work. This work is collaborative study in the framework of the LUCA project, which is funded by the German Volkswagen foundation, the PROGRESS project, which is funded by the German Ministry of Science and Research (BMBF) and the German Helmholtz Alliance 'Remote Sensing and Earth System Dynamics'. This study was supported by the German Research Centre for Geosciences GFZ, Germany, and the Central Asian Institute of Applied Geosciences (CAIAG), Bishkek (Kyrgyzstan), in the framework of the Global Change Observatory Central Asia. The ALOS data for this study were provided by the Japanese Aerospace Agency (JAXA) through the research proposal P610.

REFERENCES:

Ahmad, S., Ali, A. & Irfan, M., 2005. Imprints of transtensional deformation along Kalabagh fault in the vicinity of Kalabagh Hills, Pakistan, Pak. J. Hydrocarbon Res., 15, 35–42.

Arrowsmith, J.R. & Strecker, M.R., 1999. Seismotectonic range-front segmentation and mountain belt growth in the Pamir-Alai region, Kyrgyzstan (India-Eurasia collision zone), Geol. soc. Am. Bull., 111, 1665– 1683.

Barnhart, W.D. & Lohman, R.B., 2013. Phantom earthquakes and triggered aseismic creep: vertical partitioning of strain during earthquake sequences in Iran, Geophys. Res. Lett., 40(5), 819–823.

Bell, F.G., 1981. Geotechnical properties of some evaporitic rocks, Bull. Int. Assoc. Eng. Geol., 24, 137–144.

Blisniuk, M.P., 1996. Structure and tectonics of the northwest Himalayan frontal thrust system, Trans-Indus ranges, Northern Pakistan, Unpublished PhD thesis, Dartmouth College, Hanover, N.H., U.S.A.

Blisniuk, M.P., Sonder, L.J. & Lillie, R.J., 1998. Foreland normal fault control on northwest Himalayan thrust front development Hampshire, Tectonics, 17(5), 766–779.

Bormann, P. & Di Giacomo, D., 2011. The moment magnitude Mw and the energy magnitude Me: common roots and differences, J. Seismol., 15(2), 411–427.

Burtman, V.S., 2000. Cenozoic crustal shortening between the Pamir and Tien Shan and a reconstruction of the Pamir-Tien Shan transition zone for the Cretaceous and Paleogene, Tectonophysics, 319, 69–92.

Burtman, V.S. & Molnar, P., 1993. Geological and geophysical evidence for deep subduction of continental crust beneath the Pamir, Geol. Soc. Am. Spec., 281, 76.

Chen, C.W. & Zebker, H.A., 2001. Two-dimensional phase unwrapping with use of statistical models for cost functions in nonlinear optimization, J. Opt. Soc. Am. A, 18(2), 338–351.

Choy, G.L. & Boatwright, G.L., 1995. Global patterns of radiated seismic energy and apparent stress, J. geophys. Res., 100(B9), 18 205–18 228.

Convers, J.A. & Newman, A.V., 2011. Global evaluation of large earthquake energy from 1997 through mid-2010, J. geophys. Res., 116, B08304, doi:10.1029/2010JB007928.

Coutand, I., Strecker, M.R., Arrowsmith, R., Hilley, G., Thiede, R.C., Korjenkov, A. & Omuraliev, M., 2002. Late Cenozoic tectonic development of the intramontane Alai Valley (Pamir-Tien Shan region, Central Asia): an example of intracontinental deformation due to the Indo-Eurasia collision, Tectonics, 21(6), doi:10.1029/2002TC001358.

Dan, M.D. & Terry, E., 1985. The role of salt in fold-and-thr ust belts, Tectonophysics, 119, 67–88.

Duputel, Z., Rivera, L., Fukahata, Y. & Kanamori, H., 2012. Uncertainty estimations for seismic source inversions. Geophys. J. Int., 190(2), 1243– 1256.

Fan, G., Ni, F.J. & Wallace, C.T., 1994. Active tectonics of the Pamirs and Karakorum, J. geophys. Res., 99, (B4), 7131–7160.

Farr, T.G. & Kobrick, M., 2000. Shuttle radar topography mission produces a wealth of data, EOS, Trans. Am. geophys. Un., 81, 583–585.

Fialko, Y., Sandwell, D., Simons, M. & Rosen, P., 2005. Three-dimensional deformation caused by the Bam, Iran, earthquake and the origin of shallow slip deficit Nature, 435, 295–299.

Goldstein, R.M. & Werner, C.L., 1998. Radar interferogram filtering for geophysical applications, Geophys. Res. Lett., 25(21), 4035–4038.

Gray, A.L., Mattar, K.E. & Sofko, G., 2000. Influence of ionospheric electron density fluctuations on satellite radar interferometr y, Geophys. Res. Lett., 27(10), 1451–1454.

Hanssen, R., 2001. Radar Interferometr y: Data Inter pretation and Error Analysis, Kluwer Academic Publishers.

J´onsson, S., Segall, P., Pedersen, R. & Bjorsson, G., 2003. Post-earthquake ground movements correlated to pore-pressure transients, Nature, 424, 179–183.

J´onsson, S., Zebker, H.A., Segall, P. & Amelung, F., 2002. Fault slip distribution of the 1999 Mw7.2 Hector Mine earthquake, California, estimated from satellite radar and GPS measurements, Bull. seism. Soc. Am., 92(4), 1377–1389.

Kalmetieva, Z.A., Mikolaichuk, A.V., Moldobekov, B.D., Meleshko, A.V., Jantaev, M.M. & Zubovich, A.V., 2009. The atlas of earthquakes in Kyrgyzstan. CAIAG Bishkek, 76, ISBN 978-9967-25-829-7.

Kanamori, H., 1977. The energy release in great earthquakes, J. geophys. Res., 82, 2981–2987.

Knospe, S. & J ´onsson, S., 2010. Covariance estimation for DInSAR surface-deformation measurements in presence of anisotropic atmospheric noise, IEEE Trans. Geosci. Remote Sensing, 48(4), 2057–2065.

Korjenkov, A.M., Rust, D., Tibaldi, A. & Abdieva, S.V., 2012. Parameters of the strong Paleoearthquakes along the Talas-Fergana fault, the Kyrgyz Tien Shan, Earthquake Research and Analysis—Seismology, Seismotectonic and Earthquake Geology, ed. D'Amico, S., InTech Publ.

Krumbiegel, C., Schurr, B., Orunbaev, S., Rui, H., Pingren, L. & the TIPAGE Team, 2011. Geophys. Res. Abstr., 13, EGU2011-4846.

Kuhn, D. & Reuther, C.-D., 1999. Strike-slip faulting and nested block rotations: structural evidence from the Cordillera de Domeyko, northern Chile, Tectonophysics, 313, 383–398.

Li, T., Chen, J., Thompson, J.A., Burbank, D.W. & Xiao, W., 2012. Equivalency of geologic and geodetic rates in contractional orogens: new insights from the Pamir Frontal Thrust, Geophys. Res. Lett., 39(15), L15305, doi:10.1029/2012GL051782.

Mai, P. & Beroza, C., 2000. Source scaling properties from finite fault rupture models, Bull. seism. Soc. Am., 90, 605–615.

Marone, C.J., Scholtz, C.H. & Bilham, R., 1991. On the mechanics of earthquake afterslip, J. geophys. Res., 96(B5), 8441–8452.

Mechie, J. et al., 2012. Crustal and uppermost mantle structure along a profile across the Pamir and southern Tien Shan as derived from project TIPAGE wide-angle seismic data, Geophys. J. Int., 188(2), 385–407.

Michel, R. & Rignot, E., 1999. Flow of glacier Moreno, Argentina, from repeat-pass Shuttle Imaging Radar images: comparison of the phase correlation method with radar interferometr y, J. Glaciol., 45(149), 93– 100.

Mohadjer, S. et al., 2010. Partitioning of India-Eurasia convergence in the Pamir-Hindu Kush from GPS measurements, Geophys. Res. Lett., 37, L04305, doi:10.1029/2009GL041737.

Molnar, P., Fitch, T.J. & Wu, T.F., 1973. Fault plane solutions of shallow earthquakes and contemporary tectonics in Asia, Earth planet. Sci. Lett., 19, 101–112.

Nikonov, A.A., Vakov, A.V. & Veselov, I.A., 1983. Seismotectonics and earthquakes in the convergent zone between the Pamir and the Tien Shan. Moscow, Nauka, 240 p. (in Russian).

Nissen, E., Emmerson, B., Funning, G.J., Mistrukov, A., Parsons, B., Robinson, D.P., Rogozhin, E. & Wright, T.J., 2007. Combining InSAR and seismology to study the 2003 Siberian Altai earthquakes—dextral strike-slip and anticlockwise rotations in the northern India-Eurasia collision zone, Geophys. J. Int., 169, 216–232.

Nissen, E., Yamini-Fard, F., Tatar, M., Gholamzadeh, A., Bergman, E., Elliott, J.R., Jackson, J.A. & Parsons, B., 2010. The vertical separation of mainshock rupture and microseismicity at Qeshm island in the Zagros fold-and-thr ust belt, Iran, Earth planet. Sci. Lett., 296(3–4), 181–194.

Okada, Y., 1985. Surface Defor mation due to shear and tensile faults in a half-space, Bull. Seism. Soc. Am., 75, 1135–1154.

Peltzer, G., Rosen, P., Rogez, F. & Hudnut, K., 1992. Poroelastic rebound along the Landers 1992 earthquake surface rupture, J. geophys. Res., 103(B12), 30 131–30 145.

Reigber, C. et al., 2001. New space geodetic constraints on the distribution of deformation in central Asia. Earth planet. Sci. Lett., 191, 157–165.

Robertson, E.C., Robie, R.A. & Books, K.G., 1958. Physical Properties of salt, anhydrite, and Gypsum, Trace Elements Memorandum Report 1048, United States Department of the Interior Geological Survey.

Robinson, C.A., Yin, A., Manning, E.C., Harrison, M.T., Zhang, Sh.-H. & Wang, X.-F., 2007. Cenozoic evolution of the easter n Pamir: implications for strain-accommodation mechanisms at the wester n end of the Himalayan-Tibetan orogen, Geol. soc. Am. Bull., 119(7–8), 882–896.

Rosen, P., Henley, S., Peltzer, G. & Simons, M., 2004. Updated Repeat Orbit Interferometr y Package Released, EOS, Trans. Am. geophys. Un., 85(5), 47.

Sambridje, M., 1999. Geophysical inversion with neighborhood algorithm I. Searching a parameter space, Geophys. J. Int., 138, 479–494.

Schneider, F.M. et al., 2013. Seismic imaging of subducting continental lower crust beneath the Pamir, Earth planet. Sci. Lett., 375(1), 101–112.

Scholtz, C.H., 1998. Earthquakes and friction laws, Nature, 391, 37–42.

Sippl, C. et al., 2013. Origin and geometry of the Pamir-Hindu Kush zone of inter mediate-depth earthquakes from local seismicity data, J. geophys. Res., 118(4), 1438–1457.

Sobel, E.R., Schoenbohm, L.M., Chen, J., Thiede, R., Stockli, D.F., Sudo, M. & Strecker, M.R., 2011. Late Miocene-Pliocene deceleration of dextral slip between Pamir and Tarim: Implications for Pamir orogenesis, Earth planet. Sci. Lett., 304, 369–378.

Sobel, E., Chen, J., Schoenbohm, L., Thiede, R., Stockli, D., Sudo, M. & Strecker, M., 2013. Oceanic-style subduction controls late Cenozoic deformation of the Northern Pamir orogen, Earth planet. Sci. Lett., 363, 204–218.

Strecker, M., Frisch, M., Hamburger, M., Ratschbacher, L., Semiletkin, S., Zamoruev, A. & Sturchio, N., 1995. Quater nary defor mation in the eastern Pamirs, Tadzhikistan and Kyrgyzstan, Tectonics, 14, 1061– 1079.

Strecker, M.R., Hilley, G.E., Arrowsmith, J.R. & Coutand, I., 2003. Differential structural and geomorphic mountain-front evolution in an active continental collision zone: the NW Pamir, southern Kyrgyzstan, Geol. soc. Am. Bull., 115, 166–181.

Sudhaus, H. & J ´onsson, S., 2009. Improved source modelling through combined use of InSAR and GPS under consideration of correlated data errors: application to the June 2000 Kleifarvatn earthquake, Iceland, Geophys. J. Int., 176(2), 389–404.

Wright, T.J., Parson, B.E. & Lu, Z., 2004. Towards mapping surface deformation in three dimensions using InSAR, Geophys. Res. Lett., 31(1), doi:10.1029/2003GL018827.

Yang, S. M., Li, J. & Wang, Q., 2008. The deformation pattern and fault rate in the Tianshan Mountains inferred from GPS observations, Sci. China, 51(8), 1064–1080.

Zubovich, A.V. et al., 2010. GPS velocity field for the Tien Shan and surrounding regions, Tectonics, 29, TC6014, doi: 10.1029/2010TC002772.

Chapter 3

ALOS/PALSAR InSAR time-series analysis for detecting very slow-moving landslides in Southern Kyrgyzstan

Kanayim Teshebaeva[1,2], Sigrid Roessner[1], Helmut Echtler[1], Mahdi Motagh[1], Hans-Ulrich Wetzel[1] and Bolot Molodbekov[3]

[1] GFZ German Research Centre for Geosciences, Telegrafenberg, 14473 Potsdam; E-Mail: kanayim@gfz-potsdam.de;
[2] Institute of Earth and Environmental Sciences, Universität Potsdam, 14476 Potsdam, Germany;
[3] CAIAG Central Asian Institute for Applied Geosciences, Timur-Frunze str.73/2, Bishkek, Kyrgyzstan

Abstract

This study focuses on evaluating the potential of ALOS/PALSAR time series data to analyze the activation of deep-seated landslides in the foothill zone of the high mountain Alai range in the southern Tien Shan (Kyrgyzstan). Most previous field-based landslide investigations have revealed that many landslides have indicators for ongoing slow movements in the form of migrating and newly developing cracks. L-band ALOS/PALSAR data for the period between 2007 and 2010 are available for the 484 km^2 area in this study. We analyzed these data using the Small Baseline Subset (SBAS) time-series technique to assess the surface deformation related to the activation of landslides. We observed up to ±17 mm/y of LOS velocity deformation rates, which were projected along the local steepest slope and resulted in velocity rates of up to -63 mm/year. The obtained rates indicate very slow movement of the deep-seated landslides during the observation time. We also compared these movements with precipitation and earthquake records. The results suggest that the deformation peaks correlate with rainfall in the 3 preceding months and with an earthquake event. Overall, the results of this study indicated the great potential of L-band InSAR time series analysis for efficient spatiotemporal identification and monitoring of slope activations in this region of high landslide activity in Southern Kyrgyzstan.

Keywords: Interferometric SAR (InSAR); small baseline subset (SBAS); time-series; ALOS/PALSAR; deep seated landslide; very slow moving landslide.

3.1 Introduction

Landslides are a widespread phenomenon in mountainous regions affected by ongoing tectonic activity. Additionally, deep-seated landslides represent an especially high risk to the local population because they generally occur in the relatively densely populated foothill zones of the high mountain ranges. They are characterized by a highly variable activity style that comprises both regular and rather continuous slow movements as well as accelerations, which eventually cause sudden slope failures (Hungr et al., 2014). The velocities of very slow moving landslide are less than 1.6 m/year, according to the velocity classification of Cruden and Varnes (1996). In case of deep-seated landslides, the mobilization and downward movement often affect large masses and thus represent a potential threat with a high likelihood for catastrophic consequences for nearby populations and infrastructure. Therefore, the continuous monitoring of the state of activity is very important for slopes prone to the formation and reactivation of deep-seated landslides. One way to monitor this is to establish ground-based monitoring systems, which provide detailed information on above-ground and subsurface process characteristics contributing to the principle understanding of the nature of the phenomenon. However, these methods are mostly point-based and are rather limited in the spatial extent of the monitored area, which is especially insufficient if large areas are affected.

On the contrary, the Satellite Synthetic Aperture Radar (SAR) Interferometry (InSAR) technique has evolved as a powerful tool to assess the slope deformation related to the activation of deep-seated landslides (Calo et al., 2014; Castaldo et al., 2015; Herrera et al., 2013; Tolomei et al., 2013). With the increasing availability of suitable radar data, advanced time-series analysis techniques have been developed, which allow for the quantitative derivation of spatially variable deformation rates with increasing improvements in the temporal resolution. The resulting satellite InSAR techniques have been successfully applied for the quantitative analysis of landslide activities in a variety of environments (Akbarimehr et al., 2013; Bianchini et al., 2013; Lu et al., 2014; Sun et al., 2014; Tantianuparp et al., 2013a; Tofani et al., 2013). A comprehensive review of the current state-of-the-art satellite InSAR-based landslide investigations can be found in Wasowski & Bovenga, (2014).

In our study, the potential of satellite InSAR time-series analysis for quantitative monitoring of slope deformations related to landslide activity is assessed for a study area in Southern Kyrgyzstan, which is part of the tectonically active Tien Shan. This region is situated at the eastern margin of the Fergana Basin, one of the most landslide-prone regions in Central Asia

(Figure 1). Deep-seated landslides represent one of the major natural hazards in this densely populated region. Therefore, landslides have been investigated since the 1950s with the aim of improving the understanding of the mechanisms as a main prerequisite for the effective protection of the population (Yerokhin, 1999).

Such investigations have been carried out primarily based on field investigations and have been aided by geological and topographical maps as well as aerial photographs (Ibatulin, 2011; Yerokhin, 1999). The use of optical satellite remote-sensing data has allowed for the spatial characterization of the predisposing factors (Roessner et al., 2005a; Wetzel, 2000) and the establishment of a spatially consistent multi-temporal landslide inventory system at a regional scale by integrating landslide information from various sources (Behling et al., 2014; Golovko et al., 2015). These investigations have also revealed that most of the landslide prone slopes have been repeatedly affected by mass movements, which has resulted in various stages of the reactivation and enlargement of existing landslide bodies and an extensive relocation of already displaced slope material. Under these conditions, it is very important to obtain the spatiotemporal information concerning the level of activity of the different slope environments that are characterized by high susceptibility to landslide phenomena. Despite the above-described efforts, in the past, this region has lacked rigorous spatial analyses of the landslide activity in relation to the predisposing and triggering factors. Due to the large area affected by landslides and the limited financial means for regular ground-based investigations, satellite InSAR-based techniques and the use of spaceborne monitoring systems may, in general, be powerful tools for detecting areas of increased slope activation. This information is important for spatially and temporally differentiated hazard and risk assessments in this region.

To date, few satellite InSAR studies have been performed in Central Asia because of the limited availability of suitable radar data. However, this is changing, following the launch of the ALOS-PALSAR in 2006 and the TerraSAR-X satellites in 2007. In Southern Kyrgyzstan, L-Band ALOS-PALSAR data were used to analyze the 2008 6.5 Mw Nura earthquake (Teshebaeva et al., 2014), whereas X-band TerraSAR descending data represented the basis for detecting the landslide-related surface deformations in the area south of Uzgen (Motagh et al., 2013). The landslide-related results show that it is possible to derive quantitative deformation rates in areas that were previously affected by landslides, which indicate the reactivation of existing landslides. However, the detection of these reactivations by using short wavelength X-band data has been limited due to the lack of coherence during the winter months and the relatively

short data acquisition period (Motagh et al., 2013). This X-band sensitivity has already been described in other studies, such as Notti *et al.,* 2010 (Notti et al., 2010).

In this study, we aim to investigate the potential of the longer wavelength L-band ALOS/PALSAR data for the longer-term monitoring of landslide activity in the southern Tien Shan. Methodologically, we focus on a time-series analysis and use the small baseline subset (SBAS) technique as a satellite InSAR approach; this allows for the quantification of the deformation rates of slow-moving landslides and, thus, for the temporal analyses of their stages of activity (Lanari et al., 2007). In a second step, we analyze the obtained spatial distribution of the deformation velocity rates in relation to the geomorphic setting and the temporal evolution of the observed deformations in relation to the precipitation, temperature and earthquake activity.

3.2 Study area

3.2.1 Geological and geomorphological settings

The study area is situated in the transition zone between the Fergana basin and the high-relief Alai range as part of the southern Tien Shan near the town of Uzgen (Figure 1). This region is tectonically active as part of the Indian and Eurasian collision zone (Reigber et al., 2001; Strecker et al., 1995; Zubovich et al., 2010). Paleozoic and older rocks form the Southern Tien Shan range, and Mesozoic and Cenozoic sediments fill the Fergana basin (Cobbold et al., 1994; Cobbold et al., 1993). The geological scheme of Figure 2 shows folded and faulted sedimentary formations that range from the pre-Mesozoic basement to recent fluvial deposits with molasses-type character. These sediments have been folded and faulted as a result of Cenozoic tectonics (Cobbold et al., 1994; Cobbold et al., 1993).

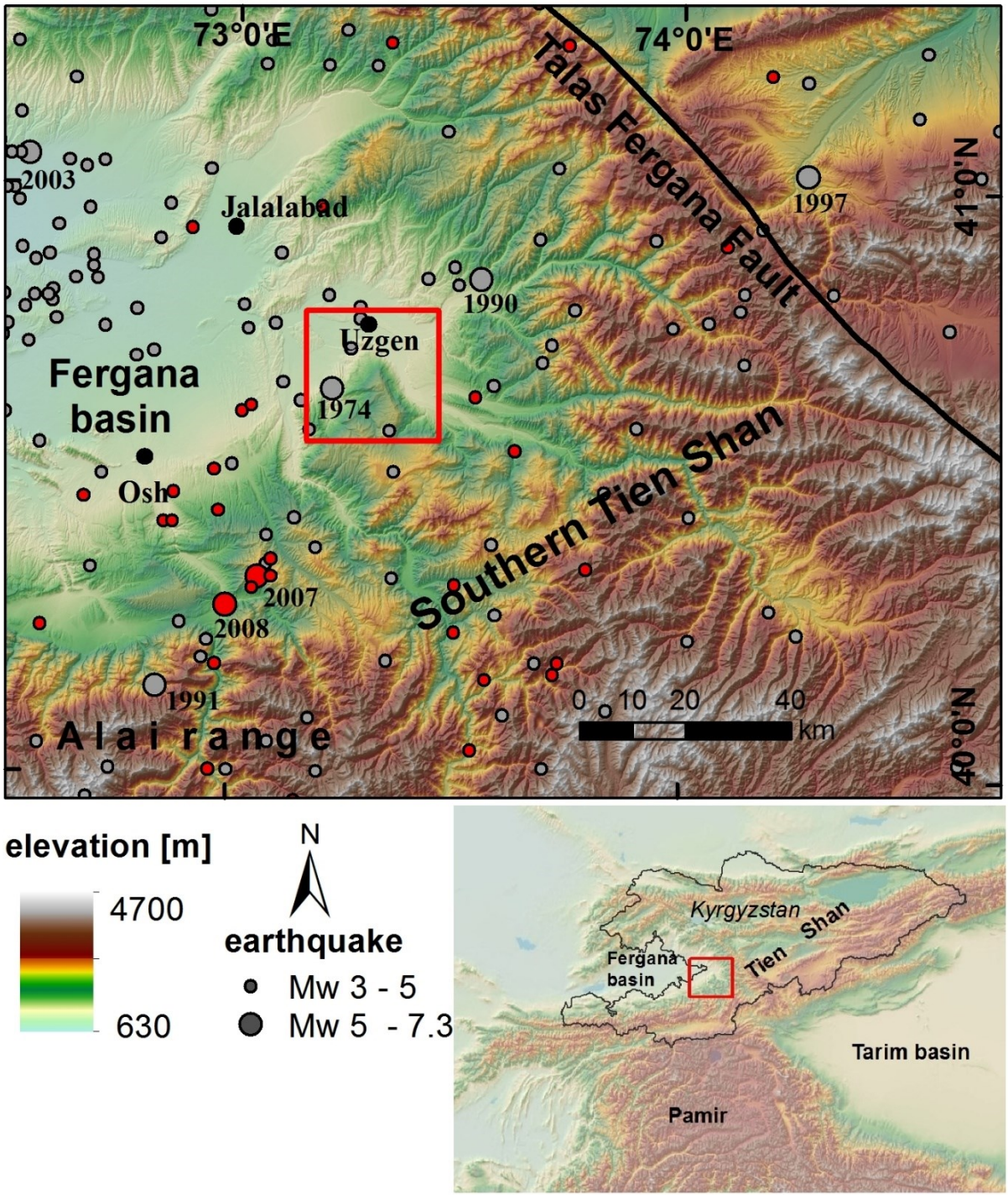

Figure 1. Geographic location of the Uzgen study area in the Southern Tien Shan. The map shows the main structures overlaid on the topography represented by the ASTER GDEM and the red box indicates the study area. The gray circles correspond to the earthquake events between 1973 and 2014 and red circles to the earthquake events between 2007 and 2014 contained in the National Earthquake Information Center (NEIC).

The Uzgen segment of the mountain front integrates an area of 484 km^2, with elevations ranging from 870 to 2250 m.a.s.l. The area is located within the Kara-Darya river basin and is divided into several hydrographic sub-basins (Figures 1, 2). The main drainage divides follow the highest elevations forming the boundaries of a triangle-shaped plateau, which is tilted to the WNW; this determines the main drainage direction for most of the study area. As a result, the eastern slope is much higher, with a maximum elevation of 2250 m.a.s.l., than the western slope, which has a maximum elevation of 1800 m.a.s.l. Both slopes are part of the Uzgen mountain front, and the western and eastern detachment areas are characterized by average slopes of 15-20 degrees. Within the west- and east-facing slopes, complex deep-seated slope failures have developed over a long period of time with unknown onsets. They are characterized by deep sliding surfaces, which lead to large initial mass movements. Subsequent reactivations of the displaced masses are characterized by low deformation rates (Figure 2). In the past, their occurrence has been mapped for the selected landslide prone areas by the Ministry of Emergency Situations and by field investigations conducted in cooperation with the GFZ Postdam. Therefore, the study area represents a suitable site for investigating the potential of multi-temporal satellite InSAR techniques to analyze ongoing landslide activity.

3.2.2 Local climate and seismicity

The climate of the region is semi-arid with an average annual precipitation of 350-600 mm/year (Yerokhin, 1999). The annual precipitation regime has two maxima: one in spring (April and May) and a less pronounced one in fall (October and November) (Duethmann et al., 2013). In winter, the study area has regular snow cover that ranges from 20 to 100 cm in thickness, depending on the elevation and exposition. The average temperature is approximately -10°C during the winter and +24°C during the summer (Yerokhin, 1999). The area is densely populated, with most of the settlements situated in the river valleys. Nearly the entire area is under agricultural use in the form of pastures and agricultural fields. Thus, the vegetation cover consists primarily of grasslands and various agricultural crops, with minor occurrences of trees and bushes.

The region around the Fergana basin is characterized by moderate seismicity (Feld et al., 2015; Haberland et al., 2011). According to the NEIC (National Earthquake Information Center, United States Geological Survey) catalogue, approximately 150 earthquakes have been recorded for the period between 1973 and 2014, and the magnitudes of the detected earthquakes

are less than 5.2 Mw at the depth ranging from 10 to 40 km. Within the study area, an instrumentally recorded earthquake, the 1974 Kurshab earthquake with a magnitude of 5.1 Mw (Figure 1), occurred near the town of Uzgen during the time period covered by the NEIC catalog.

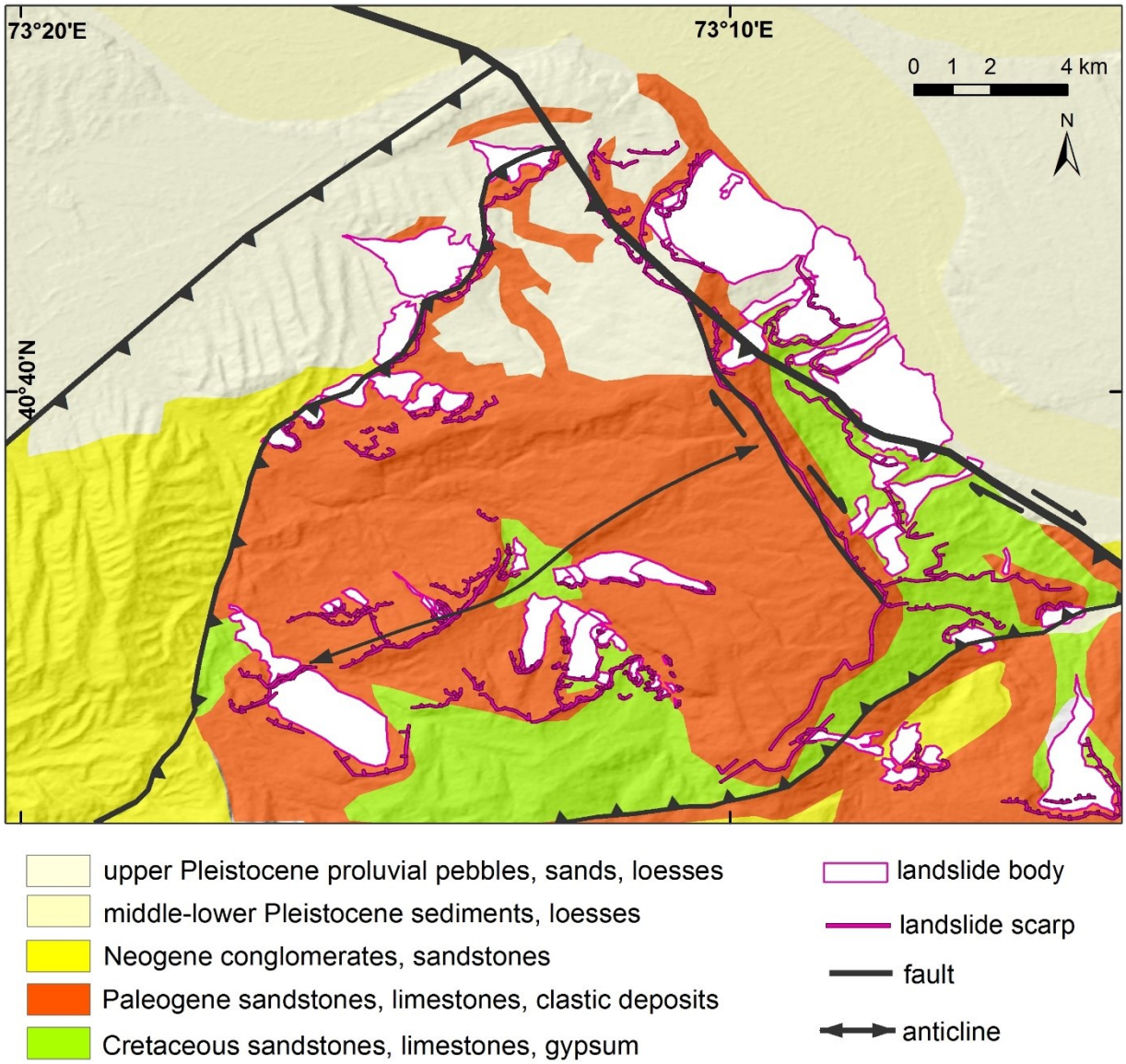

Figure 2. Geological and tectonic map of the study area near Uzgen derived from the 1:200 000 Geological map (1985) and field observations. The A and B profiles cross areas covered by mapped landslides scarps and bodies. The landslides were mapped based on optical satellite remote sensing data and field observations.

3.2.3 The landslides

Southern Kyrgyzstan is characterized by the frequent occurrence of landslides. Between 1969 and 2010, approximately 4500 landslides were observed in this region (Ibatulin, 2011). The landslides occurred at elevations ranging from 700 to 2000 m.a.s.l., which are mostly covered by weakly consolidated sediments in the foothill zones of the high mountain ranges of the southern Tien Shan. In this region, progressive mountain building has created a pronounced topographic relief; in combination with a distinct tectonic setting, this forms the spatial framework for the landslide incidents, where the majority of the landslides develop in the form of deep-seated rotational and translational slides (Roessner et al., 2005b). The main period of landslide manifestations is observed in spring, peaking in the months of March and April. The landslide intensity exhibits high interannual variability that is mainly caused by changes in the groundwater levels, which depend on the precipitation characteristics of the preceding winter season. The landslides vary in their size and movement rates (Roessner et al., 2005b). The study area itself is mainly affected by deep-seated landslides, which are characterized by slower movement rates and long periods of activation. These landslides (Figure 2) are prominently situated in Paleogene and Neogene sediments and in Quaternary loess deposits (refs. Map 1:200 000). The thickness of the loess cover does not exceed 30-40 m (Dodonov, 1991).

In this region, the frequent but sporadic occurrence of large landslides results in the temporary formation of dams and the diversion of river courses. It also leads to the extensive damage of settlements and infrastructure and to the loss of human lives. For example, since 1993, more than 250 people have died due to catastrophic slope failures (Havenith et al., 2006). Satellite remote sensing and field-based investigations of the predisposing factors have revealed that the geological and structural settings play a significant role in the spatial distribution of the landslide occurrence (Roessner et al., 2005a; Wetzel, 2000). However, there is still limited understanding of the spatiotemporal characteristics of the landslide mechanisms in relation to the main triggering factors comprising the precipitation and seismicity. In this context, satellite InSAR analysis allows for the quantitative assessment of the slope deformations related to the movement styles and rates.

3.3 Data and methodology

3.3.1 Data

The SAR imagery analyzed in this study consists of 21 ascending L-band ALOS/PALSAR data sets collected between February 2007 and October 2010. The L-band is the transmitting and receiving microwave frequency of the PALSAR, which operates at a wavelength of 23.6 cm with a temporal resolution of 46 days, and the incidence angle of the acquisitions is approximately 38 degrees. The L-band data are capable of partially reaching the ground surface by penetrating through vegetation cover, thus making PALSAR especially suitable for mapping the surface deformations over longer periods of time. The results derived from the ascending L-band data are compared with results that have been obtained from the descending X-band data for the spring-summer period of 2009 (Motagh et al., 2013). The TerraSAR-X system operates in the X-band (at a wavelength of 3.1 cm) with a temporal resolution of 11 days and an incidence angle of approximately 23 degrees.

We also used ancillary data comprising geological information derived from the 1:200 000 geological map produced by Leningrad State University in 1985; monthly precipitation/temperature data of the Uzgen station for the years 2007 to 2010 recorded by the Kyrgyz Hydrometerological Agency; and seismicity data obtained from the NEIC catalog (1973-2014).

3.3.2 StaMPS method

Slow-moving landslides can be detected and analyzed by integrating spaceborne SAR interferometry data with thematic maps and field observations (Wasowski and Bovenga, 2014). We used the StaMPS software to obtain the ground deformation (Hooper, 2008) by applying the SBAS technique to the interferograms proposed by Berardino *et al.*, 2002 (Berardino et al., 2002). The SBAS technique uses interferograms with small spatiotemporal baselines to mitigate the de-correlation phenomena of the SAR data and to reduce the Doppler centroid frequency differences (Berardino et al., 2002). The outcomes of the SBAS analyses are the mean displacement velocity maps and the time series of the displacements of each coherent pixel that can be analyzed for its temporal evolution. The time-series analysis for the study area was performed using the following workflow: (1) the generation of a subset of small baseline interferograms; (2) the selection of slowly de-correlating filtered phase (SDFP) pixels, defined as pixels whose filtered interferometric phase after azimuth and range filtering shows slow de-

correlation over short time intervals; (3) the performance of 3-D phase unwrapping of the SDFP pixels; (4) the generation of the time-series and mean velocity deformations according to the coherent pixels; (5) the visualization of the obtained deformation StaMPS results and the export to the GIS environment; (6) the projection of the LOS deformation along the local steepest slope deformation that is a downslope movement, which is then further analyzed with thematic maps. More details on the StaMPS method can be found in the literature (Hooper, 2008; Hooper and Zebker, 2007).

3.3.3 StaMPS processing

We generated a subset of small baseline interferograms with spatial and temporal baselines smaller than 2560 m and shorter than 950 days, respectively, to maintain better coherence. The key requirement in selecting spatial and temporal baselines is to consider nearly all of the available SAR acquisitions. We analyzed a total of 118 interferograms, of which pixels with a mean coherence greater than 0.35 were selected for the time-series analysis of the study area that was largely covered by a rugged vegetated topography. We removed the topographic effects from the interferograms using the SRTM (Shuttle Radar Topography Mission) DEM, which was available at a spatial resolution of 90 m (Farr and Kobrick, 2000).

We calculated the interferograms in the slant range multi-looking direction to obtain a resolution equal to the sensor-defined spatial resolution. We applied the Goldstein filter to amplify the phase signal of the generated interferograms (Goldstein and Werner, 1998). Then, we applied three-dimensional unwrapping (Delaunay 3D) to utilize the temporal information (Hooper and Zebker, 2007). The spatially correlated residuals for each small baseline interferogram were visually inspected to identify the unwrapping problems. Following the identification of the incorrectly unwrapped interferograms, we removed them from the unwrapping process. *3.3. StaMPS processing*

We generated a subset of small baseline interferograms with spatial and temporal baselines smaller than 2560 m and shorter than 950 days, respectively, to maintain better coherence. The key requirement in selecting spatial and temporal baselines is to consider nearly all of the available SAR acquisitions. We analyzed a total of 118 interferograms, of which pixels with a mean coherence greater than 0.35 were selected for the time-series analysis of the study area that was largely covered by a rugged vegetated topography. We removed the topographic effects

from the interferograms using the SRTM (Shuttle Radar Topography Mission) DEM, which was available at a spatial resolution of 90 m (Farr and Kobrick, 2000).

We calculated the interferograms in the slant range multi-looking direction to obtain a resolution equal to the sensor-defined spatial resolution. We applied the Goldstein filter to amplify the phase signal of the generated interferograms (Goldstein and Werner, 1998). Then, we applied three-dimensional unwrapping (Delaunay 3D) to utilize the temporal information (Hooper and Zebker, 2007). The spatially correlated residuals for each small baseline interferogram were visually inspected to identify the unwrapping problems. Following the identification of the incorrectly unwrapped interferograms, we removed them from the unwrapping process.

We applied 'least-squares inversion after phase-unwrapping' to retrieve the phase with respect to the original master image. We determined the quality and accuracy of the processed data by calculating the DEM error, master atmosphere and orbit error from both the small baseline and the single master interferograms. The processing of the PALSAR data resulted in a spatial resolution of 15 meters. To avoid the use of a subsequent spatial interpolator for generating the final results, we geocoded the data stack of results using a spatial resolution of 25 m. Finally, we obtained the mean velocity displacements for the time period between 2007 and 2010.

3.3.4 StaMPS results visualization and deformation along the local steepest slope

We visualized the processed StaMPS results using the viStaMPS software (Sousa et al., 2014). We displayed the LOS velocities by applying a coherence threshold of 0.35 as a threshold for the rugged topography and vegetated study area, which resulted in 17360 coherent targets for the study area shown in Figure 3. We estimated and removed the spatially correlated DEM error, which includes the error contained in the DEM itself and the error caused by the incorrect mapping of the DEM to the radar coordinates. In addition, we removed the atmospheric phase error for the orbit and master scenes. Then, we defined the 22 km by 22 km final subset of the study area shown in Figure 3 based on the spatial distribution of the coherent targets. Finally, we exported the point velocity displacements of these targets into a GIS environment for the further analysis of the obtained ground deformations.

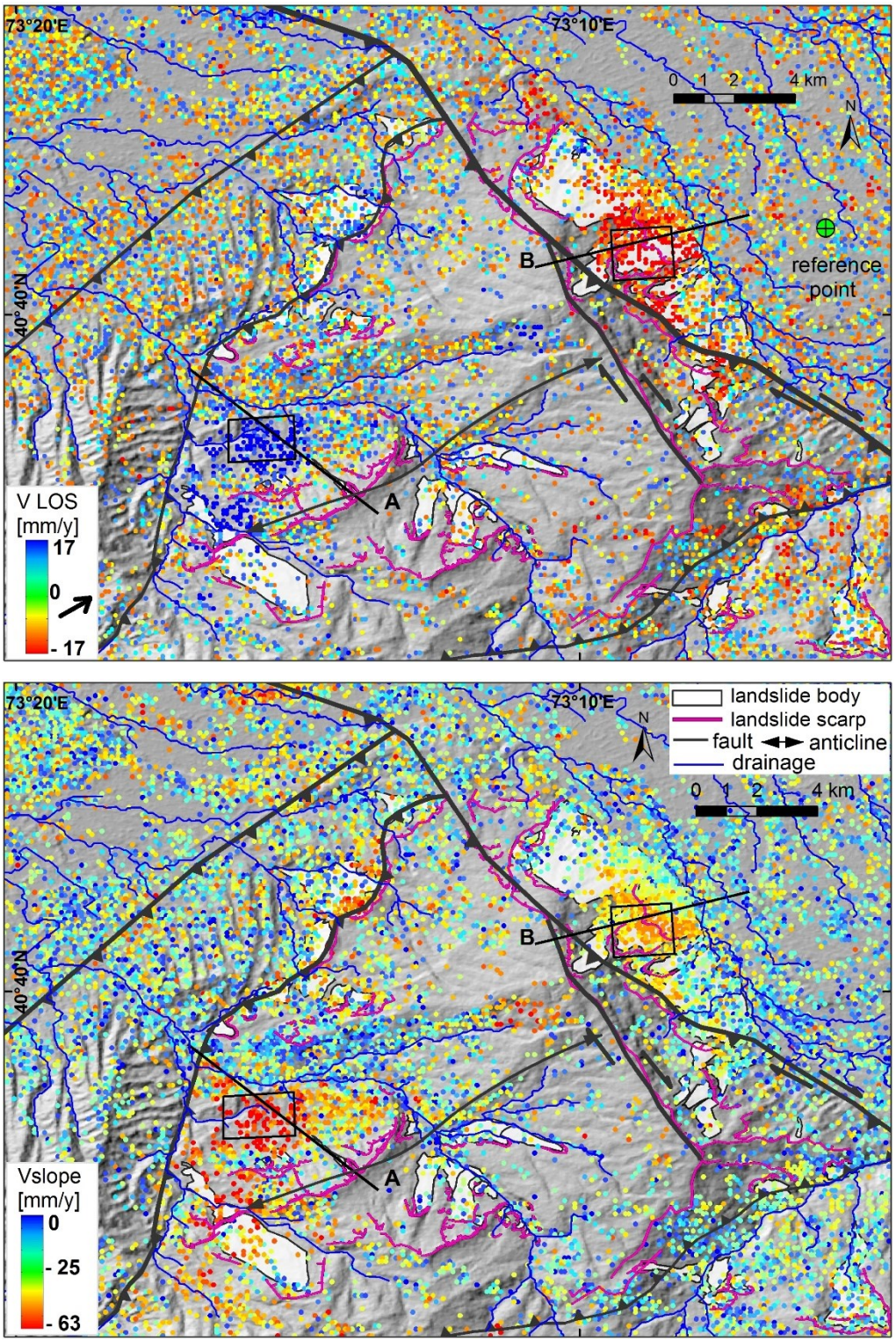

Figure 3. Map of mean velocity deformation rates (mm/y) in LOS direction (upper panel) and projected to downslope Vslope velocity deformation rates (mm/y) (lower panel) obtained for spatially distinct coherent targets (color dots) for the time period between 2007 and 2010. The black boxes represent the spatial subsets for the detailed temporal analysis of slope deformation patterns.

The SBAS-retrieved deformation values represent the one-dimensional LOS projection of the actual movement of the Earth's surface. To overcome the differences between the ground geometry and the LOS direction, we projected the LOS deformations into the direction of the down slope movements (Cascini et al., 2010). We converted the LOS velocity deformation rates into downslope velocity deformation rates (Vslope) (Bardi et al., 2014; Cascini et al., 2010; Colesanti and Wasowski, 2006). To transform the LOS direction into the down slope direction, we needed information about the unit LOS vectors and the slopes. For the unit LOS vectors, we used the incidence angle and the flight azimuth of the satellite. In addition, we employed the slope angle and the slope azimuth for the study area (Figure 4), including the calculations of the slope and azimuth values using the ASTER GDEM2, because the 30-m spatial resolution is better than the 90-m resolution of the SRTM-DEM.

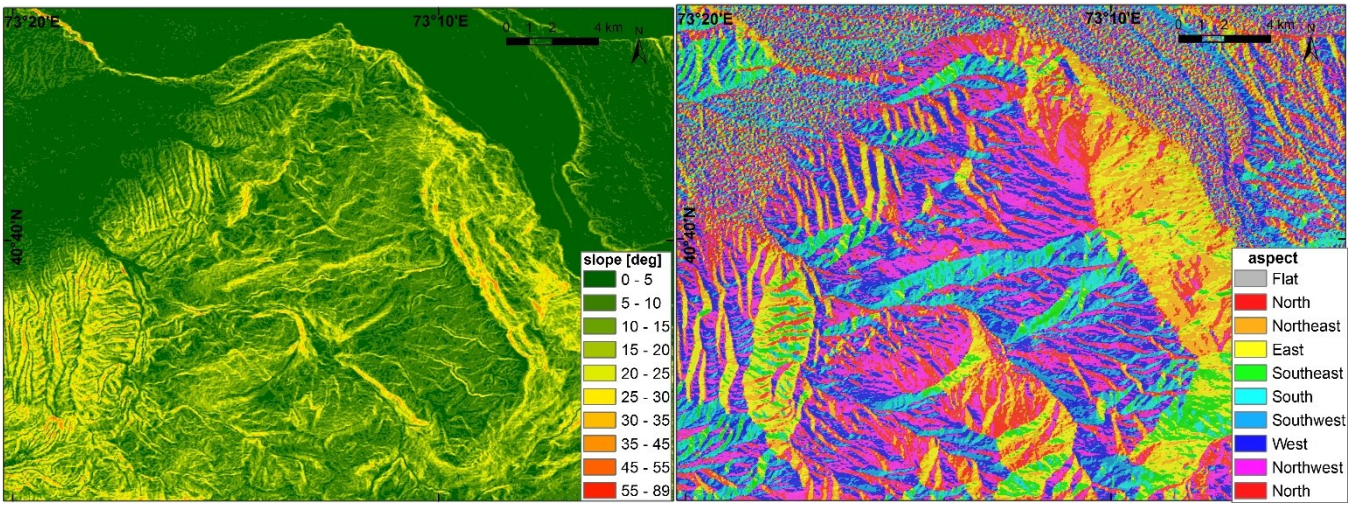

Figure 4. Slope and aspect map of the study area calculated based on ASTER GDEM2.

3.4 SBAS results and interpretation

3.4.1 Spatial distribution of landslide deformation

The processed 21 ALOS/PALSAR L-band scenes cover a time period of four years (2007-2010). The obtained SBAS results were derived for 17360 coherent targets situated in the 484-km^2 subset of the Uzgen mountain front (Figure 3). We selected a reference point (Figure 3) that was characterized by high coherence and whose deformation behavior was known a priori as a non-deforming zone. This zone represents the stable foreland outside the tectonically active

area, as indicated by a younger geological surface (Figure 4). From the results shown in Figure 4, we identified a selection of benchmarks located in the non-deforming zone, which represent the area around the reference point.

The obtained SBAS results only show displacements where the surface moves towards or away from the satellite along the line of sight. The L-band wavelength maintains good coherence over the longer periods of time (up to one year) and thus provides longer-term information of the surface deformations related to the landslide processes. The results of the ascending interferograms are more sensitive to the mass movements that occur on the eastward facing slopes. Our satellite InSAR results show the deformations in areas that were formerly affected by landslides. The velocity rates in the LOS direction are up to ±17 mm/year (the red to blue color range in Figure 3). The most pronounced surface deformation signals detected in this study are located at different slope orientations: one signal is observed on the east slope, and the other is found on the west slope (Figure 3). To homogenize these differences, we project the LOS to the downslope, and we obtain the Vslope landslide movements.

The SBAS-observed downslope velocity deformation rates (Vslope) range from >0 to 63 mm/y (Figure 3). Among the coherent locations characterized by high downslope deformation rates, we identified two major signals. One is situated on the (1) western slope, and the other is on the (2) eastern slope; both were determined using the downslope velocity values (Figure 3).
(1) At the western slope we observed downslope velocity deformation rates of up to -63 mm/y (Figure 3). The observed signal covers an area that is up to 4 km wide and ranges in elevation from 1800 m.a.s.l to 1100 m.a.s.l. over a horizontal distance of approximately 6 km, which results in an average slope of 15 degrees. Increased deformations on the western slope mainly occur in the area represented by profile A (Figure 5), which had not been identified previously as an active landslide area. However, these locations are situated in the downslope vicinity of morphologically distinct scarps, which indicate the presence of relict landslide masses in this area (Chediya, 1986) (Figure 5).
(2) On the eastern slope, we observed downslope deformation velocity rates of up to -35 mm/y, which occur primarily in the area of already-existing landslide bodies (Figure 3). In this area, the presence of geomorphologically distinct landslide features allowed for the mapping of individual landslide bodies using optical remote-sensing data and field investigations (Figures 5, 6).

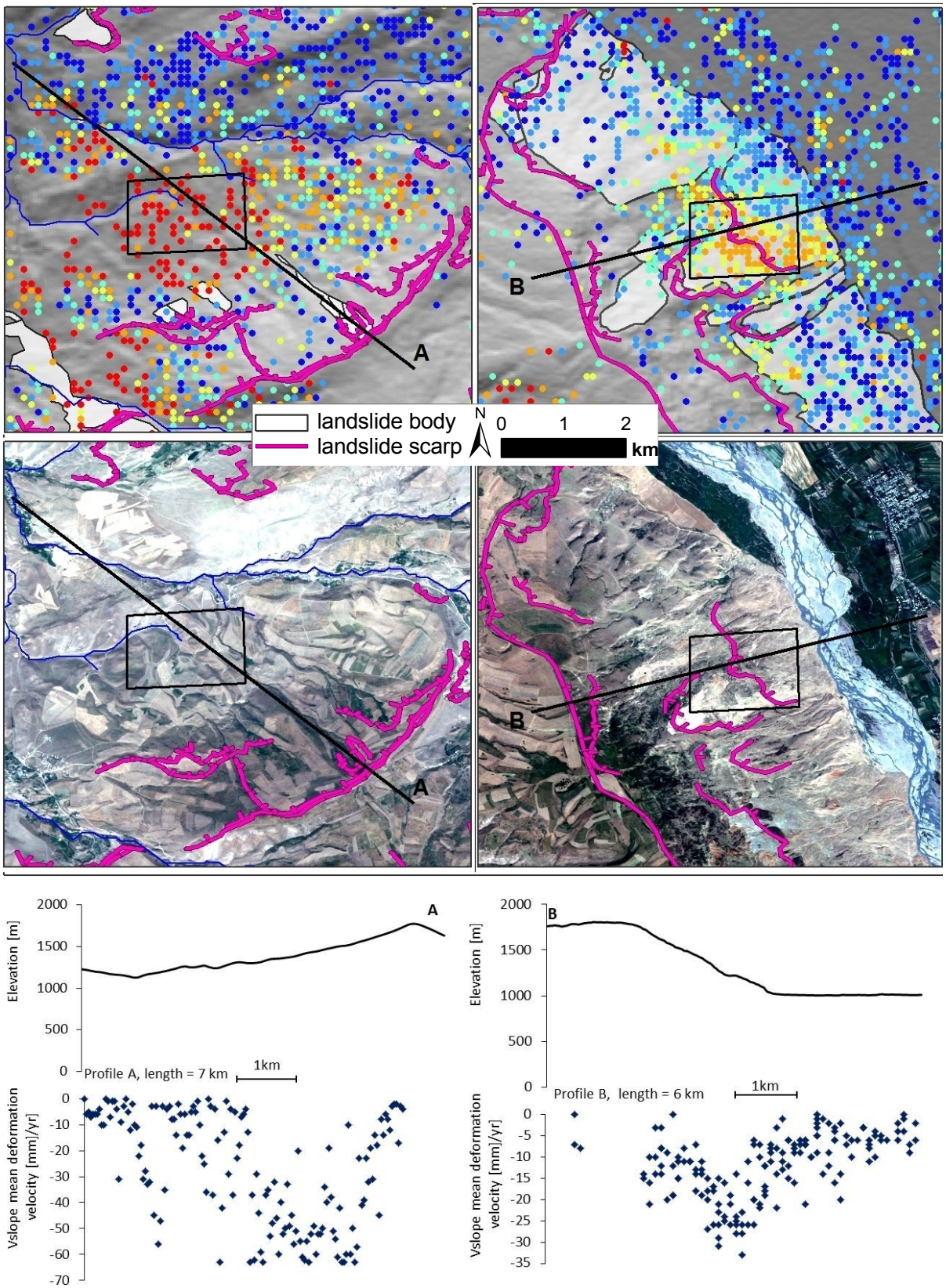

Figure 5. Map of Vslope deformations drawn across the west (profile A) and east (profile B) (upper panel). The middle panel shows the coverage of the area by optical RapidEye data which were acquired in August 2014. The lower panels depict profile information of the down slope deformations and elevation data.

The eastern slope is characterized by several fresh scarps and surface breaks, which indicate recent downslope movements and were documented during field work in September 2011 (Figure 6). The observed signal is up to 5 km wide and covers an area with elevations ranging from 1900 m.a.b.s.l. and 1000 m.a.b.s.l., with a horizontal distance of approximately 5 km, thus resulting in an average slope of 17 degrees. On the eastern slope, represented by profile B (Figure 6), coherent locations that are characterized by increased deformation spatially coincide with previously mapped landslides, which indicates ongoing landslide activity during the analysis period.

3.4.2 Temporal evolution of landslide deformation

In addition to analyzing the mean deformation rates (section 4.1), we investigated the temporal evolution of the detected deformations between 2007 and 2010 based on the time series of date-to-date LOS displacements (Figure 7). For this purpose, we de-trended our time series data to exclude any linear trends that could influence the subsequent analysis. To understand the temporal evolution of the detected deformation, we analyzed the data in relation to the temperature, precipitation and seismicity. For this purpose, we constructed 1.6-km-wide swath profiles depicted as black boxes in Figure 3, and we calculated the minimum, maximum and average deformation values that occurred within these areas to check the signal stability.

In Figure 8, we plotted the values of the de-trended date-to-date deformation time series for the period 2007-2010 against the available time series data for the precipitation (monthly sums) and the temperature (monthly means) as well as the temporal occurrence of the October 2008 Mw 4.1 earthquake. For both profiles, the observed LOS displacements indicate continuous movements in the LOS direction (Figures 7, 8).

Profiles A and B (Figure 6) show differences in the temporal evolution between the deformation signals. Based on the plots, we compared the LOS displacement signals with the temperature and precipitation. The temporal evolution of the deformation along profile A shows a continuous LOS deformation with a distinct peak in October 2008 (Figure 8). The profile B plots also indicate a 3-month correlation between the precipitation and the increased deformation rates. Comparing the time series of deformation with the time series of temperature data for profiles A and B (Figure 8) shows that our observed time series LOS deformation signal does not correlated with the changes in temperature. This observation suggests that the slope instabilities in this area are not related to freezing and thawing processes.

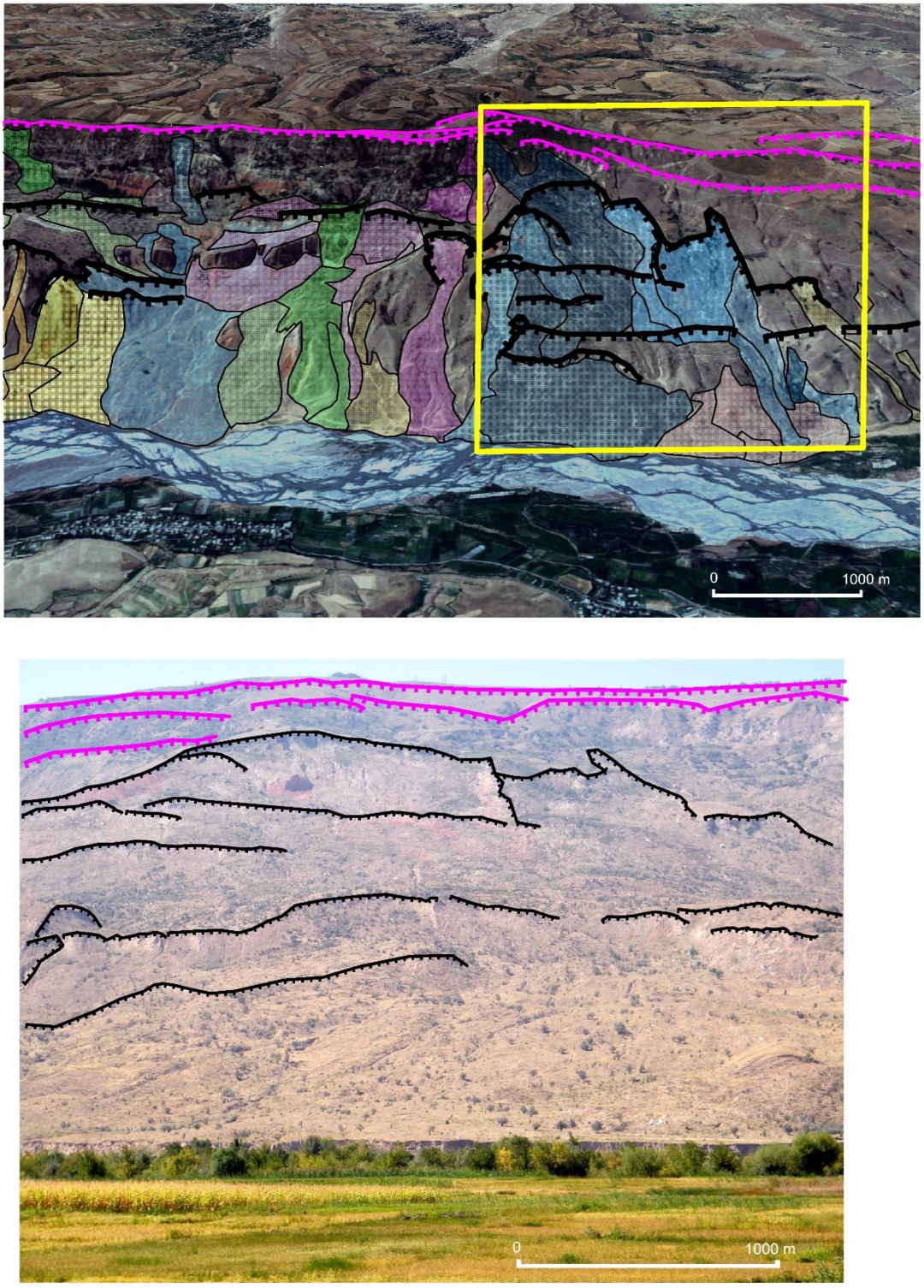

Figure 6. Mapped landslide complexes derived from optical remote sensing data and field observations. Perspective view of the eastern slope (Fig.4) overlaid by Rapid Eye imagery acquired on the 5th April 2011 (upper panel) and field photo (yellow box) taken on 11 September 2012 (lower panel). The individual landslide bodies are indicated by different colors, the main scarps are depicted in magenta and secondary scarps are depicted in black.

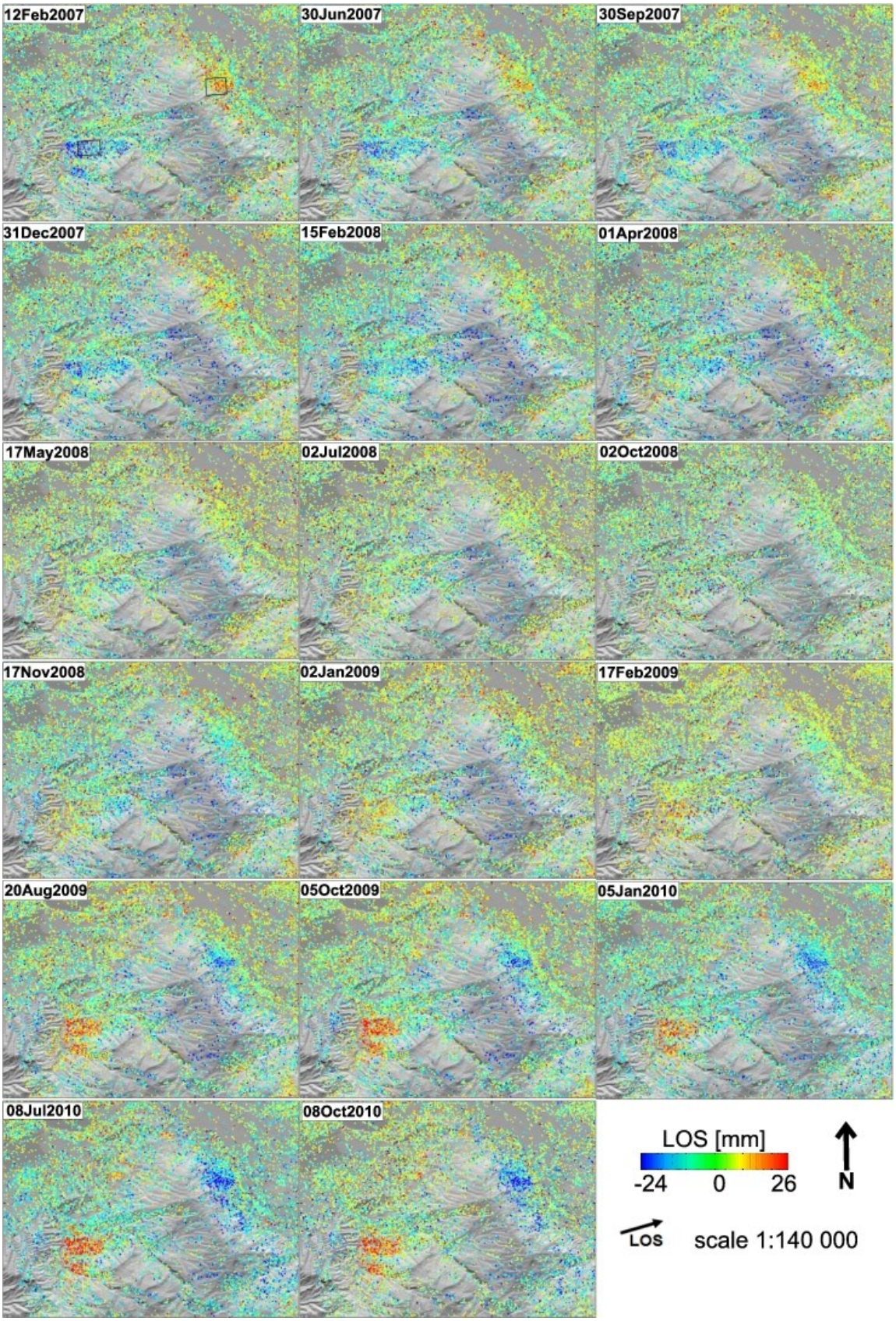

Figure 7. Time-series LOS displacement map for the period between 2007 and 2010. The data inside of black boxes presented in time-series profiles in Figure 7.

3.5 Discussion

3.5.1 SBAS results assessment

In general, the quality of multi-temporal interferometry is checked using cross-comparisons and ground truth (Wasowski and Bovenga, 2014). We apply the approach of comparing the ascending L-band PALSAR observations with the descending X-band TSX observations, which have been derived for the same study area (Motagh et al., 2013). Our L-band PALSAR results represent the cumulative surface displacements for the analyzed time period 2007-2010, which indicate reactivations in the larger parts of the east and west slopes of the Uzgen area. The analysis of the same Uzgen area using descending X-band TSX data showed episodic cm-scale displacement features in the area of the west slope only during the spring-summer period of 2009. Motagh *et al.*, 2013(Motagh et al., 2013) excluded the winter season from their analysis due to a lack of coherence caused by the strong de-correlation of the InSAR signal. The interferometric coherence degraded quickly in the winter and early spring period, presumably due to continuous snow cover, rainfall or the start of vegetation growth. The results from the ascending L-band data spatially correlate with the results obtained from the descending X-band data.

Our L-band results and X-band results are complementary; thus, the L-band data are more suitable for long-term monitoring and the X-band data for short-term monitoring of unstable slopes in the mountainous regions of Southern Kyrgyzstan. Similar observations of the performance of L-band ALOS data compared with X-band and C-band data have been made in the Tena Valley of the Central Spanish Pyrenees (Herrera et al., 2013). However, the X-band data preserve the spatial details and short-term slope deformations well**.** Therefore, they exhibit good potential for the rapid assessment of changes that might occur before or after large slope failures, including the detection of damages related to these failures through more detailed analyses of areas characterized by the loss of or decrease in coherence (Notti et al., 2010; Wasowski and Bovenga, 2014).

3.5.2 Downslope deformations of landslides

The downslope velocity deformation rates of up to -63 mm/y (Section 4.1) lie in the category of very slow moving landslides (Cruden and Varnes; Hungr et al., 2014). Our analyses show that our detected areas of activation within the landslide-prone slopes are located in areas characterized by a slope angle of 15-17 degrees, which is much smaller than the ALOS/PALSAR look angle of 38 degrees. Therefore, landslides can be detected without limitations (Bianchini et al., 2013; Sun et al., 2014; Zhao et al., 2012). Thus, in the area of the Uzgen mountain front, the landslide-prone slopes exhibit the best geometry for monitoring based on the use of L-Band ALOS/PALSAR data.

The eastern slope reveals a predominant movement in the NE direction, which is perpendicular to the orientation of the neighboring river valley. The western slope is characterized by a predominant NNW movement direction, which is parallel to the orientation of the neighboring river valley. Compared with the eastern slope, the obtained velocity rates are approximately 45% higher for the western slope (Figure 3). The western slopes surface deformation occurs in an area underlain by Paleogene clastics. Despite the absence of unequivocal geomorphological indicators of ongoing landslide activity, the high deformation rates on the western slope suggest the reactivation of an ancient landslide body.

Compared with the western slope, the eastern slope has been well documented and mapped because of its high ongoing landslide activity. The origins of these slope failures are deep-seated landslides, where the sliding plane has formed along the boundary between the Cretaceous rocks and the unconformable overlying Pleistocene sediments. The local authorities have confirmed protracted landslides in this area (oral communication Ministry of Emergency Situations). The most recent major failures in this area occurred in 1988 and in the period between 2003 and 2005, and they coincide with phases of high landslide activity in Southern Kyrgyzstan. The temporal evolution of the landslide activity in this area derived from the optical satellite remote-sensing time-series data exhibit regularly reoccurring landslide activity between 1990 and 2013 (Behling et al., 2014).

The SBAS results suggest that the already displaced landslide masses have been subject to subsequent reactivations, which also affect the youngest Pleistocene deposits. Comparable findings of the ALOS/PALSAR-derived downslope velocities of the very slow moving landslides have been observed in Spain (Bianchini et al., 2013) and in Three Gorges in China

(Tantianuparp et al., 2013b).

3.5.3 Potential controls on landslide activity

The analyzed deformation time series reveal the presence of temporal changes of up to a few mm/y in the velocity of the landslide movements for the west and east slopes. The analysis presented in Section 4.2 shows that the observed signals do correlate with an earthquake and precipitation but do not correlate with temperature. In general, the low velocity rates of the surface deformations on the slopes may arise from a wide variety of causes and are thus not simple to interpret (Colesanti and Wasowski, 2006; Wasowski and Bovenga, 2014). However, in case of landslides, the most significant impacts are often those related to (1) climatic variations and their influence on hydrogeology (Wasowski and Bovenga, 2014) or to the deep-seated landslides of the folded and faulted inherited tectonic structures with (2) moderate seismicity in the unconsolidated sediments (Agliardi et al., 2001).

(1) The east slope surface deformation patterns reconstructed along profile B show some seasonality (Figure 8). The deformation acceleration is most likely driven by gravitational slope processes, which are influenced by the overall steeper relief and by changes in the ground water level that result from the integrative amount of precipitation occurring within the last 3 months prior to the observed deformation increase. This result is in accordance with the observations provided by the Ministry of Extreme Emergency (Yerokhin, 1999). Similar findings of the landslide seasonality have been reported from Northern California (Zhao et al., 2012) for the area of the Berkeley Hills slide (Hilley et al., 2004). Due to low temporal resolution of the ALOS/PALSAR data, it is impossible to determine a more precise correlation between the landslide activation and precipitation (Zhao et al., 2012).

(2) In the area of the west slope, the observed high deformation rates are most likely related to seismic activity, which primarily manifests itself along the local faults. The available seismicity data for the area show that the distinct deformation peak observed in profile A can be linked to the Mw 4.1 earthquake, which occurred on 26 September 2008, at a 30-km distance from the local thrust system. Moreover, that area had been previously affected by an Mw 5.1 earthquake in February 1974. At that time, mass movements following the earthquake had also been reported (Kalmetieva et al., 2009). In the area of the west slope, the LOS time-series deformation shows correlation with the seismic activity, which likely leads to the gravitational reactivation of old landslide structures in the vicinity of a tectonically active fault.

Moreover, our deformation results have revealed different activity stages in an area of ongoing landslide activity (east slope) as well as the activation of an area that has not been affected by visible landslide activity in the recent past (west slope). These findings are in agreement with already existing knowledge of landslide processes in this area (Roessner et al., 2005a), thus leading to the observation that the deep-seated landslides occurring in this area are the result of complex interplay between hydrometeorological factors, the local geological setting and seismicity.

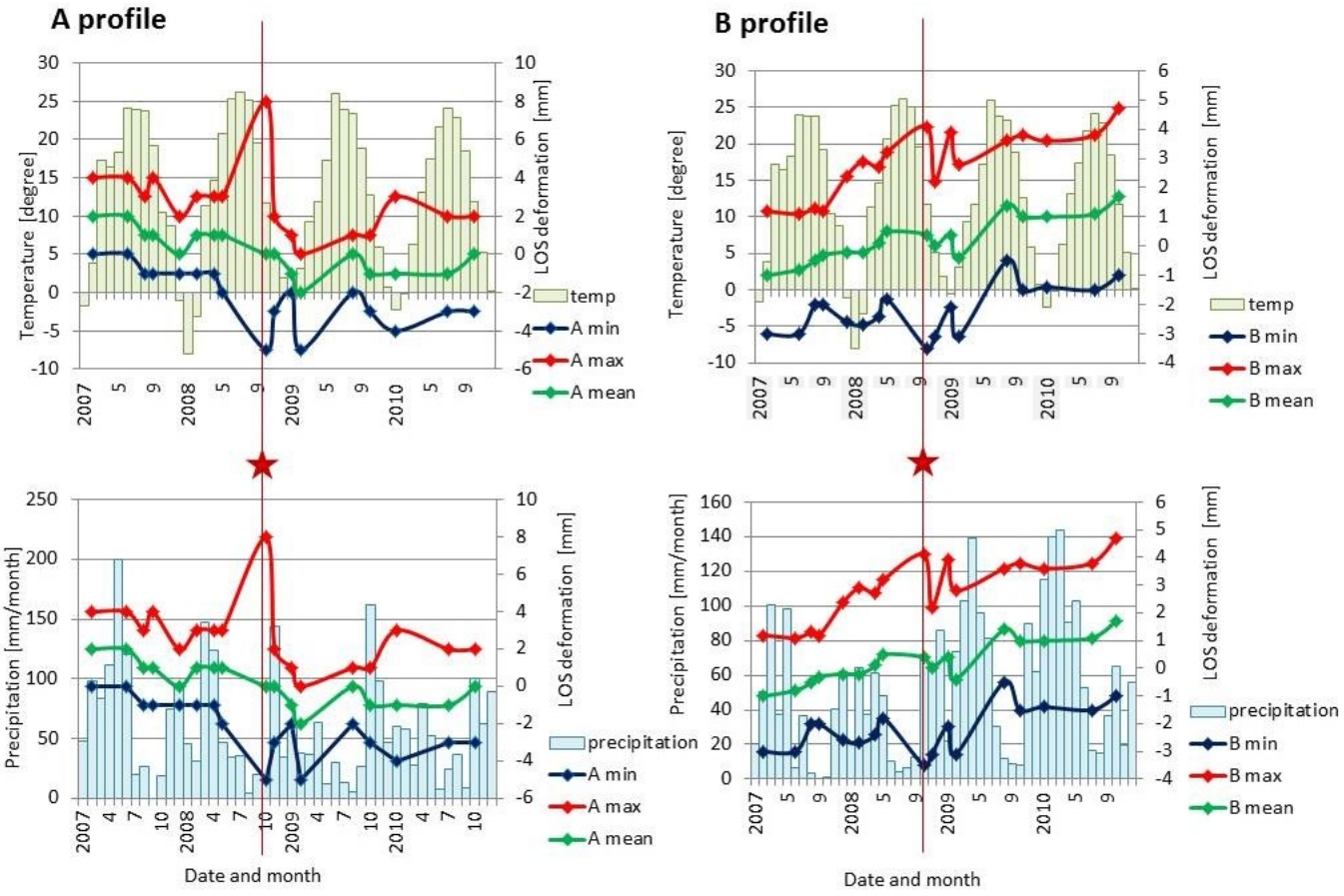

Figure 8. Time-series LOS displacement along profiles A and B for the period between 2007-2010 plotted against monthly sums of precipitation and monthly averages of temperature. The peak of the deformation on 2nd October 2008 coincides with the Mw 4.1 earthquake of 26th September 2008.

3.6 Conclusions

In this study, we show the potential of satellite InSAR analysis based on L-band ALOS/PALSAR imagery to detect and map very slow-moving landslides. Satellite InSAR time-series analysis has resulted in very slow and temporally uniform landslide movements, which have occurred during the time period from 2007 to 2010. Further analyses of the temporal evolution of these very slow-moving landslide show that the local seismicity and the prior 3-month precipitation amounts contribute to the activation of landslide prone slopes. Most of the obtained deformation represents the reactivation of already existing landslides; whereas the spatial occurrence is controlled by the folded and faulted inherited tectonic structures within the weakly consolidated sediments. The obtained L-band results correlate spatially with the X-band results obtained in an earlier study (Motagh et al., 2013), which indicates continuous landslide activity in the area of the Uzgen mountain front. Thus, it can be concluded that the results obtained by the two independent studies are consistent and can be used concurrently to assess both short- and longer-term landslide activity in this area. Both studies have shown the great potential of satellite InSAR analysis for the regular monitoring of landslide activity along the widespread landslide prone slopes in this region. The observed deformations represent important information, which can be integrated using dynamic approaches for hazard assessment. Thus, our results show that L-band missions are of great importance for the longer-term monitoring of landslide activity in mountainous regions. In this context, new opportunities have been created from the recently launched PALSAR-2 and Sentinel-1 missions. In the future, the radar remote-sensing data acquisition capabilities will greatly improve for areas such as Central Asia; this will increase the opportunity for the development of operational satellite InSAR-based monitoring systems, which are complementary to ground-based slope observations. The combined analyses of the obtained SBAS results with additional landslide-related information will support regular process monitoring as part of a quantitative hazard and risk assessment as well as an early warning system in Southern Kyrgyzstan and other landslide prone regions of Central Asia.

Acknowledgments

We thank Bodo Bookhagen, Oliver Korup and Manfred Strecker for valuable discussions, which helped to improve the content of the paper. This research was funded by the Volkswagen foundation within the frame of the LUCA (Land Use, Ecosystem Services and Human Welfare in Central Asia) post-graduate programme. The work was also supported by the German Research Foundation (DFG) under the auspices of the Graduate School GRK1364 "Shaping Earth's Surface in a variable Environment" (Strecker STR 373/18-1) and the Central Asia and Afghanistan Research Fellowship (CAARF). The ALOS data for this study were provided by the Japanese Aerospace Agency (JAXA) through the research proposal P610.

References and Notes

Agliardi, F., G. Crosta, and A. Zanchi, 2001, Structural constraints on deep-seated slope deformation kinematics: Engineering Geology, v. 59, p. 83-102.

Akbarimehr, M., M. Motagh, and M. Haghshenas-Haghighi, 2013, Slope Stability Assessment of the Sarcheshmeh Landslide, Northeast Iran, Investigated Using InSAR and GPS Observations: Remote Sensing, v. 5, p. 3681.

Bardi, F., W. Frodella, A. Ciampalini, S. Bianchini, C. Del Ventisette, G. Gigli, R. Fanti, S. Moretti, G. Basile, and N. Casagli, 2014, Integration between ground based and satellite SAR data in landslide mapping: The San Fratello case study: Geomorphology, v. 223, p. 45-60.

Behling, R., S. Roessner, H. Kaufmann, and B. Kleinschmit, 2014, Automated Spatiotemporal Landslide Mapping over Large Areas Using RapidEye Time Series Data: Remote Sensing, v. 6, p. 8026-8055.

Berardino, P., G. Fornaro, R. Lanari, and E. Sansosti, 2002, A new algorithm for surface deformation monitoring based on small baseline differential SAR interferograms: Geoscience and Remote Sensing, IEEE Transactions on, v. 40, p. 2375-2383.

Bianchini, S., G. Herrera, R. M. Mateos, D. Notti, I. Garcia, O. Mora, and S. Moretti, 2013, Landslide Activity Maps Generation by Means of Persistent Scatterer Interferometry: Remote Sensing, v. 5, p. 6198-6222.

Calo, F., F. Ardizzone, R. Castaldo, P. Lollino, P. Tizzani, F. Guzzetti, R. Lanari, M. G. Angeli, F. Pontoni, and M. Manunta, 2014, Enhanced landslide investigations through advanced DInSAR techniques: The Ivancich case study, Assisi, Italy: Remote Sensing of Environment, v. 142, p. 69-82.

Cascini, L., G. Fornaro, and D. Peduto, 2010, Advanced low- and full-resolution DInSAR map generation for slow-moving landslide analysis at different scales: Engineering Geology, v. 112, p. 29-42.

Castaldo, R., P. Tizzani, P. Lollino, F. Calò, F. Ardizzone, M. Manunta, F. Guzzetti, and R. Lanari, 2015, The Ivancich Active Landslide Process (Assisi, Central Italy) Analysed via Numerical Modeling Jointly Optimized by DInSAR and Inclinometric Data, *in* G.

Lollino, D. Giordan, G. B. Crosta, J. Corominas, R. Azzam, J. Wasowski, and N. Sciarra, eds., Engineering Geology for Society and Territory - Volume 2, Springer International Publishing, p. 1513-1517.

Chediya, O., 1986, Morfostruktury i noveishii tektogenez Tyan'-Shanya (Morfostructures and Neotectonics of the Tien Shan): Ilim, Frunze (Bishkek), Kyrgyzstan, p. 314.

Cobbold, P., E. Sadybakasov, and J. Thomas, 1994, Cenozoic transpression and basin development, Kyrgyz TienShan, Central Asia.: Geodynamic Evolution of Sedimentary Basins, International Symposium.: Moscow.

Cobbold, P. R., P. Davy, D. Gapais, E. A. Rossello, E. Sadybakasov, J. C. Thomas, J. J. Tondji Biyo, and M. de Urreiztieta, 1993, Sedimentary basins and crustal thickening: Sedimentary Geology, v. 86, p. 77-89.

Colesanti, C., and J. Wasowski, 2006, Investigating landslides with space-borne synthetic aperture radar (SAR) interferometry: Engineering Geology, v. 88, p. 173-199.

Cruden, D., and D. Varnes, 1996, Landslide types and processes., In, Landslides: investigation and mitigation., Edited by, A. K. Turner and R. L. Schuster. Transportation Research Board, Special Report 247, pp. 36-75.

Dodonov, A. E., 1991, Loess of Central Asia: GeoJournal, v. 24, p. 185-194.

Duethmann, D., J. Zimmer, A. Gafurov, A. Güntner, D. Kriegel, B. Merz, and S. Vorogushyn, 2013, Evaluation of areal precipitation estimates based on downscaled reanalysis and station data by hydrological modelling: Hydrol. Earth Syst. Sci., v. 17, p. 2415-2434.

Farr, T. G., and M. Kobrick, 2000, Shuttle radar topography mission produces a wealth of data: EOS Transactions, v. 81, p. 583-585.

Feld, C., C. Haberland, B. Schurr, C. Sippl, H.-U. Wetzel, S. Roessner, M. Ickrath, U. Abdybachaev, and S. Orunbaev, 2015, Seismotectonic study of the Fergana Region (Southern Kyrgyzstan): distribution and kinematics of local seismicity: Earth, Planets and Space, v. 67, p. 40.

Goldstein, R. M., and C. L. Werner, 1998, Radar interferogram filtering for geophysical applications: Geophysical Research Letters, v. 25, p. 4035-4038.

Golovko, D., S. Roessner, R. Behling, H.-U. Wetzel, and B. Kleinschmit, 2015, Development of Multi-Temporal Landslide Inventory Information System for Southern Kyrgyzstan Using GIS and Satellite Remote Sensing: Photogrammetrie-Fernerkundung-Geoinformation, v. 2015, p. 157-172.

Haberland, C., U. Abdybachaev, B. Schurr, H. Wetzel, S. Roessner, A. Sarnagoev, S. Orunbaev, and C. Janssen, 2011, Landslides in southern Kyrgyzstan: understanding tectonic controls: Eos Trans AGU, v. 92, p. 20.

Havenith, H. B., I. Torgoev, A. Meleshko, Y. Alioshin, A. Torgoev, and G. Danneels, 2006, Landslides in the Mailuu-Suu Valley, Kyrgyzstan - Hazards and impacts: Landslides, v. 3, p. 137-147.

Herrera, G., F. Gutierrez, J. C. Garcia-Davalillo, J. Guerrero, D. Notti, J. P. Galve, J. A. Fernandez-Merodo, and G. Cooksley, 2013, Multi-sensor advanced DInSAR monitoring of very slow landslides: The Tena Valley case study (Central Spanish Pyrenees): Remote Sensing of Environment, v. 128, p. 31-43.

Hilley, G. E., R. Bürgmann, A. Ferretti, F. Novali, and F. Rocca, 2004, Dynamics of slow-moving landslides from permanent scatterer analysis: Science, v. 304, p. 1952-1955.

Hooper, A., 2008, A multi-temporal InSAR method incorporating both persistent scatterer and small baseline approaches: Geophysical Research Letters, v. 35.

Hooper, A., and H. A. Zebker, 2007, Phase unwrapping in three dimensions with application to InSAR time series: Journal of the Optical Society of America a-Optics Image Science and Vision, v. 24, p. 2737-2747.

Hungr, O., S. Leroueil, and L. Picarelli, 2014, The Varnes classification of landslide types, an update: Landslides, v. 11, p. 167-194.
Ibatulin, K. V., 2011, Monitoring of landslides in Kyrgyzstan. Ministry of Emergency Situations of the Kyrgyz Republic., p. 145.
Kalmetieva, Z., A. Mikolaichuk, B. Moldobekov, A. Meleshko, M. Jantaev, A. Zubovich, and H. Havenith, 2009, CAIAG, Bishkek.
Lanari, R., F. Casu, M. Manzo, G. Zeni, P. Berardino, M. Manunta, and A. Pepe, 2007, An Overview of the Small BAseline Subset Algorithm: a DInSAR Technique for Surface Deformation Analysis: Pure and Applied Geophysics, v. 164, p. 637-661.
Lu, P., S. B. Bai, and N. Casagli, 2014, Investigating Spatial Patterns of Persistent Scatterer Interferometry Point Targets and Landslide Occurrences in the Arno River Basin: Remote Sensing, v. 6, p. 6817-6843.
Motagh, M., H. U. Wetzel, S. Roessner, and H. Kaufmann, 2013, A TerraSAR-X InSAR study of landslides in southern Kyrgyzstan, Central Asia: Remote Sensing Letters, v. 4, p. 657-666.
Notti, D., J. C. Davalillo, G. Herrera, and O. Mora, 2010, Assessment of the performance of X-band satellite radar data for landslide mapping and monitoring: Upper Tena Valley case study: Natural Hazards and Earth System Sciences, v. 10, p. 1865-1875.
Reigber, C., G. W. Michel, R. Galas, D. Angermann, J. Klotz, J. Y. Chen, A. Papschev, R. Arslanov, V. E. Tzurkov, and M. C. Ishanov, 2001, New space geodetic constraints on the distribution of deformation in Central Asia: Earth and Planetary Science Letters, v. 191, p. 157-165.
Roessner, S., H. Wetzel, H. Kaufmann, and A. Sarnagoev, 2005a, Potential of satellite remote sensing and GIS for landslide hazard assessment in Southern Kyrgyzstan (Central Asia): Nat Hazards, v. 35, p. 395 - 416.
Roessner, S., H. U. Wetzel, H. Kaufmann, and A. Sarnagoev, 2005b, Potential of satellite remote sensing and GIS for landslide hazard assessment in southern kyrgyzstan (Central Asia): Natural Hazards, v. 35, p. 395-416.
Sousa, J. J., P. Guimarães, A. Sousa, A. M. Ruiz, G. Patrício, L. Magalhães, and F. Pereira, 2014, viStaMPS – A Collaborative Project for StaMPS-MTI Results Interpretation: Procedia Technology, v. 16, p. 842-848.
Strecker, M., W. Frisch, M. Hamburger, L. Ratschbacher, S. Semiletkin, A. Zamoruyev, and N. Sturchio, 1995, Quaternary deformation in the eastern Pamirs, Tadzhikistan and Kyrgyzstan: Tectonics, v. 14, p. 1061-1079.
Sun, Q., L. Zhang, X. Ding, J. Hu, and H. Liang, 2014, Investigation of Slow-Moving Landslides from ALOS/PALSAR Images with TCPInSAR: A Case Study of Oso, USA: Remote Sensing, v. 7, p. 72.
Tantianuparp, P., X. Shi, L. Zhang, T. Balz, and M. Liao, 2013a, Characterization of Landslide Deformations in Three Gorges Area Using Multiple InSAR Data Stacks: Remote Sensing, v. 5, p. 2704.
Tantianuparp, P., X. G. Shi, L. Zhang, T. Balz, and M. S. Liao, 2013b, Characterization of Landslide Deformations in Three Gorges Area Using Multiple InSAR Data Stacks: Remote Sensing, v. 5, p. 2704-2719.
Teshebaeva, K., H. Sudhaus, H. Echtler, B. Schurr, and S. Roessner, 2014, Strain partitioning at the eastern Pamir-Alai revealed through SAR data analysis of the 2008 Nura earthquake: Geophysical Journal International, v. 198, p. 760-774.
Tofani, V., F. Raspini, F. Catani, and N. Casagli, 2013, Persistent Scatterer Interferometry (PSI) Technique for Landslide Characterization and Monitoring: Remote Sensing, v. 5, p. 1045-1065.

Tolomei, C., A. Taramelli, M. Moro, M. Saroli, D. Aringoli, and S. Salvi, 2013, Analysis of the deep-seated gravitational slope deformations over Mt. Frascare (Central Italy) with geomorphological assessment and DInSAR approaches: Geomorphology, v. 201, p. 281-292.

Wasowski, J., and F. Bovenga, 2014, Investigating landslides and unstable slopes with satellite Multi Temporal Interferometry: Current issues and future perspectives: Engineering Geology, v. 174, p. 103-138.

Wetzel, H. U., Roessner, S., and Sarnagoev, A., 2000, Remote sensing and GIS based geological mapping for assessment of landslide hazard in Southern Kyrgyzstan (Central Asia): Management Information Systems 2000 - GIS and Remote Sensing, p. 355-366.

Yerokhin, S. A., 1999, Investigation of landslide occurence in Osh and Djalalabad provinces of the Kyrgyz Republic., Bishkek, Institute of Geology.

Zhao, C. Y., Z. Lu, Q. Zhang, and J. de la Fuente, 2012, Large-area landslide detection and monitoring with ALOS/PALSAR imagery data over Northern California and Southern Oregon, USA: Remote Sensing of Environment, v. 124, p. 348-359.

Zubovich, A., X. Wang, Y. Scherba, G. Schelochkov, R. Reilinger, C. Reigber, O. Mosienko, P. Molnar, W. Michajljow, V. Makarov, J. Li, S. Kuzikov, T. Herring, M. Hamburger, B. Hager, Y. Dang, V. Bragin, and R. Beisenbaev, 2010, GPS velocity field for the Tien Shan and surrounding regions: Tectonics, v. 29.

Chapter 4

Styles of surface deformation in the southern Kyrgyz Tien Shan revealed from InSAR analyses and tectonic geomorphology

Teshebaeva Kanayim[1,3], Echtler Helmut[1,2], Bookhagen Bodo[2], Strecker Manfred[2]

[1] GFZ German Research Centre for Geosciences, Telegrafenberg, 14473 Potsdam;

[2] Institute of Earth and Environmental Sciences, Universität Potsdam, 14476 Potsdam, Germany;

[3] CAIAG Central Asian Institute for Applied Geosciences, Timur-Frunze str.73/2, Bishkek, Kyrgyzstan

Abstract

This study focuses on analyzing slow moving slope instabilities in the southern Kyrgyz Tien Shan mountain front using radar (ALOS/PALSAR) time-series data. The interferometric analysis of ALOS/PALSAR radar data integrates a period of 4 years (2007-2010) based on the Small Baseline Subset (SBAS) time-series technique to assess surface deformation with millimeter-change accuracy. We have analyzed 118 interferograms and we observe spatially-continuous movements with downslope velocities up to 71 mm/yr. In order to understand the spatial pattern of landsliding, we related the tectonic morphologic and lithologic settings with the patterns of hillslope deformation. We demonstrate that the preconditioned lithological and tectonic structural patterns are the main controlling factors for downslope mass movement and deformation magnitude. The terrain relief in the study area is controlled by the active contractional deformation of the frontal part of the orogenic wedge. Some of the slower but continuously moving slope instabilities are directly related to tectonically active faults in unconsolidated young Quaternary synorogenic sedimentary sequences. The InSAR observed slow moving landslides represent active deep-seated gravitational slope deformation phenomena which is first time observed in the Tien Shan mountains. The long-term tectonic activity evaluated by extracting ksn values, which correlated with unconsolidated lithologies and for this study it is not an appropriate metric of tectonic deformation. Our approach offers a new combination of InSAR techniques and tectonic aspects to localize and understand slope instability phenomena in the tectonically active mountain fronts of the Kyrgyz Tien Shan.

Keywords: Interferometric SAR (InSAR); small baseline subset (SBAS); deep-seated landslide; river steepness index; tectonic geomorphology; topography; Tien Shan.

4.1 Introduction

The morphology of the tectonically active mountains of the southern Tien Shan is shaped by a combination of tectonic and geomorphologic processes. The interplay of tectonic preconditioning and near-surface processes result in slope instabilities and mass movements e.g., (Arrowsmith and Strecker, 1999; Bazhenov, 1993; Biske, 1996; Burtman, 2000; Burtman, 2006; Cobbold et al., 1996; Molnar and Tapponnier, 1975; Strecker et al., 1995). Some of the largest instabilities are deep-seated, slow-moving slope deformation and resulting landslides in unconsolidated rock types pose an increased risk to the population in mountainous valleys (Jomard et al., 2014, Ambrosi and Crosta, 2006).

The geomorphic role and impact of these deep-seated gravitational slope deformation have been recognized for about a century, but only in the past few decades has the phenomenon been extensively studied (Agliardi et al., 2012; Ambrosi and Crosta, 2006; Dikau, 1996; Galadini, 2006; Gori et al., 2014; Strom and Korup, 2006). For the last decade, differential SAR interferometry techniques have been successfully used to monitor deep-seated slope deformations (Ambrosi and Crosta, 2006; Colesanti et al., 2003; Colesanti and Wasowski, 2006). However, there is still a limited understanding of the deep-seated slope movement in relation to active tectonic structures that may ultimately help to explain the locations of large slope failures and their geometry.

Deep-seated gravitational slope deformation has been observed and documented in many mountain belts through the world and in different lithologies (Agliardi et al., 2012; Ambrosi and Crosta, 2006; Dikau, 1996; Galadini, 2006; Gori et al., 2014; Strom and Korup, 2006). But substantial research on deep-seated gravitational slope deformation in the Tien Shan mountains is not available because this phenomena was not detected and interpreted before.

Our study area at the southern Tien Shan mountain front is an area of tectonic inversion (Fig. 1). It is located to the south and east of the Fergana valley and includes areas that have been affected by mass movements, landsliding and earthquakes e.g. (Abdrakhmatov et al., 2003; Arrowsmith and Strecker, 1999; Chediya, 1986; Danneels et al., 2008; Molnar et al., 1973; Roessner et al., 2005; Teshebaeva et al., 2014; Wetzel, 2000; Yerokhin, 1999).

In our hypothesis the active deformation in the collisional setting of the Pamir-Tien Shan and northward propagating folding and thrusting of the lower plate Alai ridge is the main process to sustain the necessary gravitational instabilities to explain these extraordinary continuous and slow slope deformations. The objective of our study is to understand the spatial distribution of slope deformation and its relation to pre-existing lithologic contrasts and tectonically-active structures. We present an innovative combination of satellite based interferometric synthetic aperture data (InSAR) data, tectonic and morphometric analyses plus field-based observations to constrain the relation between active orogenic and surface deformation of deep-seated gravitational movements.

4.2 Geologic and Geomorphologic setting of the southern Tien Shan and Alai range

The study area is situated in the transition between the low lands of the Fergana basin and the high-relief Alai range also termed as the southern Kyrgyz Tien Shan (Fig.1). The Alai ridge is part of the Central Asian intracontinental Tien Shan mountains that are active since the Late Cenozoic (Arrowsmith and Strecker, 1999; Bazhenov, 1993; Biske, 1996; Burtman, 2000; Burtman, 2006; Cobbold et al., 1996; Molnar and Tapponnier, 1975; Reigber et al., 2001; Sengör et al., 1993; Strecker et al., 1995; Zubovich et al., 2010).

The Alai Range constitutes an active orogenic wedge in the lower plate of the Pamir – Tian Shan collision zone that we describe as a progressively northward propagating fold-and-thrust belt. This region shows one of the high convergence rates of the India-Eurasia collision zone (Reigber et al., 2001; Zubovich et al., 2010, Fig. 1). The northern Pamir thrust system currently absorbs more than 50 percent of the 25 mm/yr convergence between the Pamir and Eurasia (Ischuk et al., 2013; Mohadjer et al., 2010; Reigber et al., 2001; Zubovich et al., 2010).

The northern orogenic front in the area south of Uzgen (Fig. 1 and 2) shows active frontal tectonic uplift, folding and northward thrusting or inverse faulting. The fold-and-thrust belt geometries (Fig. 1) show segmentation into top-to-N forethrusts, top-to-S backthrusts, and dextral (transpressional) NW - SE trending dextral strike slip faults (Fig. 2). These define thrust segments connected to NW-trending dextral transpressive faults all related to the general N-S oriented direction of contraction. Fold axes from the actively deformed Neogene to Quaternary sedimentary formations as well as the related thrust and inverse faults trend N 50 – 60 and NW-SE oriented compression in our study area deviated along the active Kara Darya inverse dextral strike-slip fault (Fig. 1 and 2).

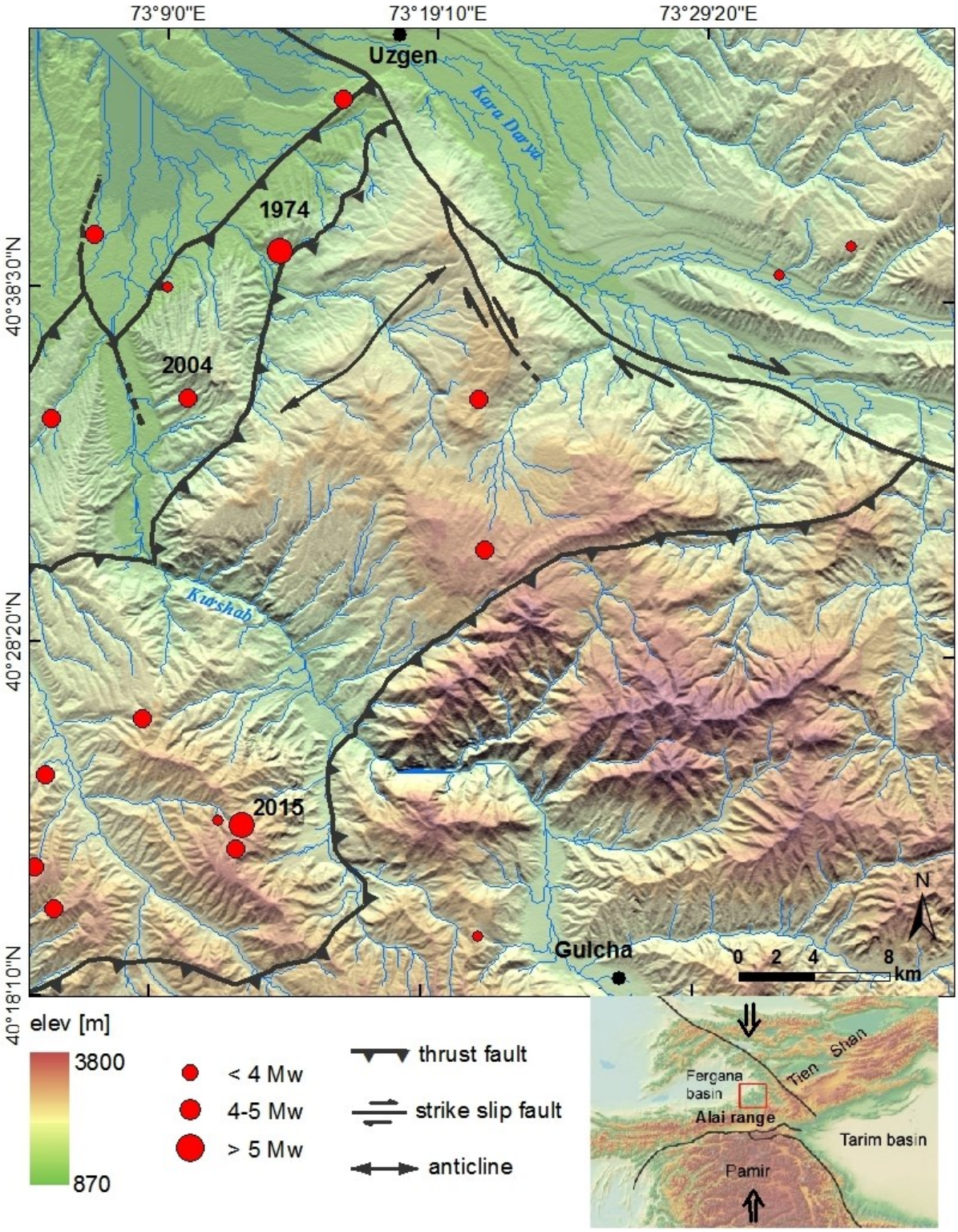

Figure 1. Geographic location of the study area in the southern Kyrgyz Tien Shan (see inset). Main geologic structures (Chediya, 1986) are shown in black overlaid on the SRTM (Shuttle Radar Topography Mission) topography. The red circles correspond to earthquake events derived from the NEIC (National Earthquake Information Center) catalog for the period between 1973 and 2015.

The rock formations that integrate this orogenic wedge range from Paleozoic metamorphic sedimentary to recent alluvial sequences (Fig. 2). A thick syn-orogenic coarse terrestrial formation, Late Oligocene to recent in age is superseding fine grained lacustrine and shallow marine formations, Early Cenozoic in age and related to low-relief and peneplain conditions since the Jurassic (Cobbold et al., 1994; Cobbold et al., 1993b).

The limestones, sandstones, shales, and phylities constitute Variscan structures related with the Late Paleozoic orogeny of the CAOB (Central Asian Orogenic Belt) (Kirscher et al., 2013; Sengör et al., 1993; Windley et al., 2007). The oldest post-CAOB sedimentary cover integrate Jurassic terrestrial clastics and coal layers. Until Middle Oligocene times, the low dynamic terrestrial deposition integrate lacustrine formations alternating with clay, red sandstones and evaporites. Prominent geologic markers are shallow marine oyster-bearing limestones dated from Cretaceous to Late Eocene in the region (Biske, 1996; Cobbold et al., 1993a). The quite condensed Mesozoic to Paleogene pre-alpine and post "Variscan" sequence does not exceed hundreds of meters. Coarsening-up clastic rocks start with the Latest Oligocene and are associate with the first orogenic processes and India-Eurasia collisional tectonics during Neogene times (Strecker et al., 1995). The thick Quaternary sediments also cover the tectonically-inverted Fergana Basin (Fig. 2) that consist of thick molassic conglomerates grading upwards into loess deposits. These Neogene formations constitute the syn-orogenic markers.

The Alai mountain front incorporates an area of about 3000 km^2 with a topographic gradient ranging from 870 to 3800 m above mean sea level. The area is located within the Kara Darya river basin and is divided into several hydrographic sub-basins. The main drainage divides the basin along the highest elevations forming the boundaries of area, tilted in the direction of WNW constituting the main drainage direction for most of the study area. (Fig. 1 and 2).

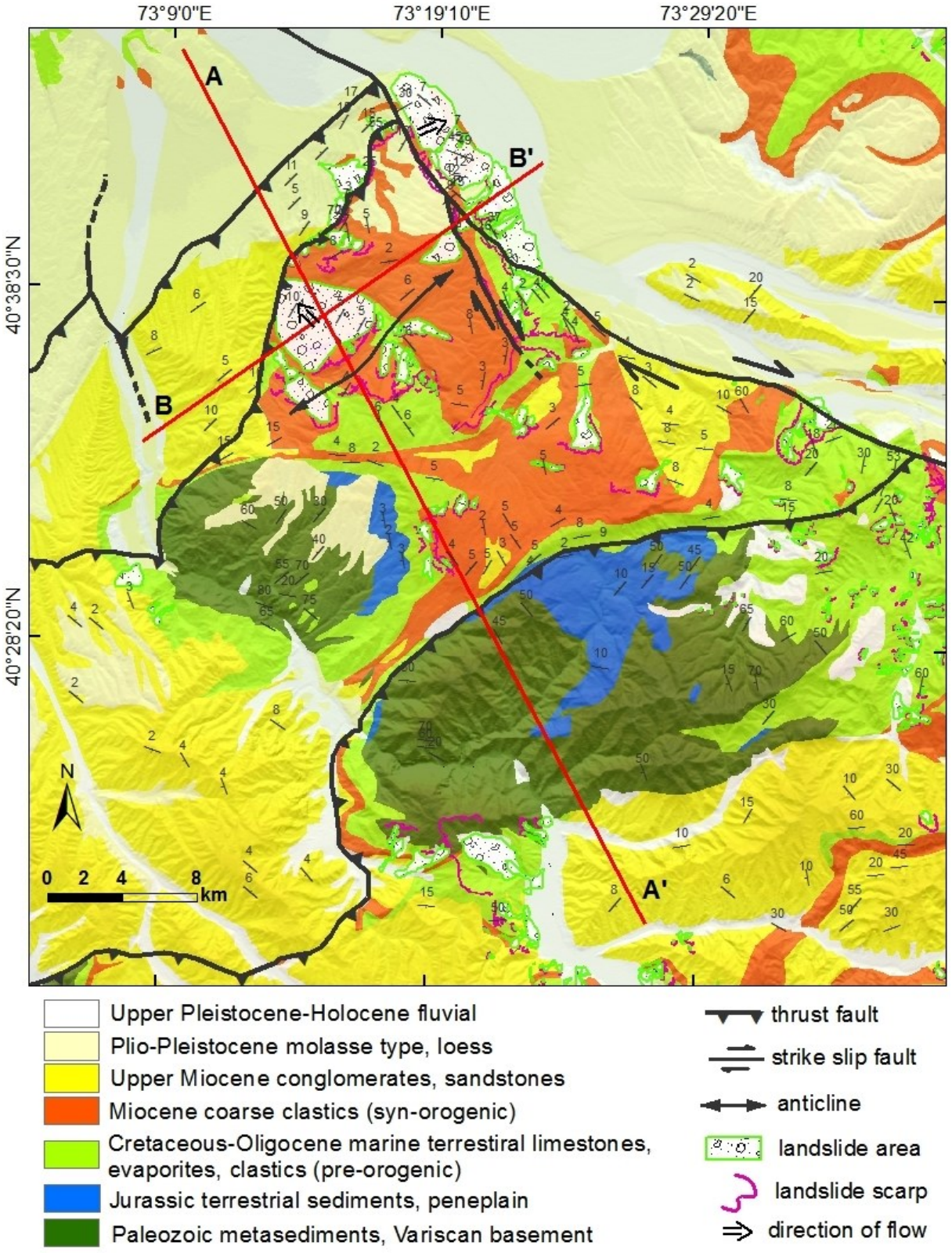

Figure 2. Detailed geologic, tectonic, and structural map of the study area derived from 1:50 000 and 1:200 000 Geological maps (Kyrgyz geological agency 1958, 1985) and own field observations. The landslides were mapped based on optical satellite remote sensing data and field observations (Wetzel, 2000). The AA' and BB' profiles indicate locations of 2-km wide swaths for geomorphologic analyses (Figs. 12, 13).

4.2.1 Seismicity

The study area shows moderate seismicity and is considered seismically active (Feld et al., 2015; Haberland et al., 2011). The National Earthquake Information Center (NEIC), United States Geological Survey, has recorded earthquakes between 1973 and 2015 with a magnitude Mw > 3 Mw (Fig. 1). These earthquakes are characterized as shallow with hypocenter depth that range between 10 and 25 kilometers. Among the recorded earthquakes two are with magnitude Mw > 5: one of them recorded in 1974 with magnitude Mw of 5.1 with shallow hypocenter and thrust mechanism; and a recent 2015 recorded earthquake with magnitude Mw of 5.5 near the village of the Gulcha with a shallow hypocenter (Fig.1).

The spatial distribution of seismicity in the region is uneven without a single predominant fault or structure that can absorb the majority of seismic energy. Other faults in the region are west-east trending, south-vergent thrust faults and northwest-southeast trending oblique faults and defined as tectonically active (Feld et al., 2015; Haberland et al., 2011). Along with reverse faults and thrusts, strike-slip displacements also characterize the neotectonic structure in the region. Fault planes show a majority of thrust mechanisms followed by strike-slip mechanisms. These earthquake mechanisms and the stress field are dominated by NW-SE compression in the regional tectonics setting (Buslov et al., 2007; Cobbold et al., 1996; Ghose et al., 1998; Ni and York, 1978).

4.2.2 Climatic conditions

The climate of the region is semi-arid with an average annual precipitation of 350-600 mm/year (Yerokhin, 1999). The annual precipitation regime has two maxima, one in spring (April and May), and a less pronounced one in fall (October and November) (Duethmann et al., 2013). During the winter, the study area is snow covered with thicknesses ranging between 20 to 100 cm depending on elevation and exposition. The average temperature is about -10^0 C during winter (December to February) and +24° C during summer (May to September) (Yerokhin, 1999).

4.2.3 Surface deformation and landslides

Landslides occur frequently in southern Tien Shan. Approximately 4500 landslides were observed in this region between 1969 and 2010 (Ibatulin, 2011). Largely, landslide occur within the elevation range of between 700 and 2000 m asl where surfaces are mostly covered with weak consolidated clastic sediments. In this region, progressive mountain building has created a pronounced topographic relief in combination with a distinct tectonic setting that constitute the spatial framework for mass movement occurrence where the majority of landslides develop in form of deep-seated rotational and translational slides (Roessner et al., 2005). Deep-seated landslides are common in the study area, generally more than 15 m in depth, characterized by slow continuous movement rates and long periods of activity. The slope failures involve the underlying bedrock (Danneels et al., 2008). Landslide occurrences are most frequent during the peak of spring from March to April and autumn October. The intensity of landslide shows a high inter-annual variability, mainly caused by changes in groundwater levels, which depend on the precipitation characteristics of the preceding winter season. The landslides vary in their size and movement rates and very slow moving landslides have been observed in the area (Teshebaeva et al., 2015).

In this region, the frequent occurrence of large landslides results in temporary formation of dams and diversion of river courses. It also leads to extensive damage of settlements and infrastructure as well as loss of human lives. For example, catastrophic landslides on 22 April 2003 killed 38 people in the village of Kara-Taryk along the river Kurshab within the study area. Moreover, one year later on 27 April 2004, 33 people were buried and killed under a landslide in the same region. A total of 20 landslides were recorded during April 2004 alone, prior to these landslides on 9th April 2004 the Uzgen area has been affected by shallow earthquake with magnitude 4.2 Mw (Fig.1) and two people were killed by a landslide on May 11, 2004 (Ibatulin, 2011). Satellite remote sensing and field-based investigations of predisposing factors have revealed that the geological and structural settings play the main role in the spatial distribution of landslide occurrence (Behling et al., 2014; Roessner et al., 2005; Teshebaeva et al., 2015). However, there is still a limited understanding of the very slow moving deep-seated landslides in relation to lithology, structure, and topographic relief that will explain the locations of large slope failures and their geometry.

4.3 Data and methods

4.3.1 Data

The SAR imagery analyzed in this study consists of 20 ascending L-band ALOS/PALSAR data collected between February 2007 and October 2010 (Table 1). The L-band is the transmitting and receiving microwave frequency of PALSAR, which operates in a wavelength of 23.6 cm with a temporal resolution of 46 days, whereas the incidence angle of the acquisitions is 38 degree. The capability of L-band radar to reach the ground by partially penetrating through vegetation to obtain information about the ground surface makes PALSAR especially suitable for mapping earth-surface deformations over longer periods of time in this region.

The SRTM (Shuttle Radar Topography Mission) Digital Elevation Model (DEM) is used for geomorphological analysis. SRTM is the X-band 1 Arc-Second Global elevation data at a nominal resolution of 30 meters (Farr and Kobrick, 2000).
We also used ancillary data comprising geological information derived from the 1:200 000 and 1:50 000 geological map produced by the Leningrad State University in 1958 and Kyrgyz geological agency in 1985; seismicity data obtained from NEIC catalog (1973-2014).

4.3.2 Time-series InSAR analysis

To illustrate the dynamic of slope processes we use InSAR approach with small baseline subset (SBAS) technique (Berardino et al., 2002). Time-series InSAR technique allows for the quantification of the deformation rates of slow-moving landslides and, thus, for the temporal analyses of their stages of activity (Lanari et al., 2007). We used StaMPS software to obtain ground deformation (Hooper, 2008) using SBAS technique of interferograms stacking (Berardino et al., 2002). The SBAS technique uses interferograms with small spatiotemporal baselines to mitigate the de-correlation phenomena of the SAR data and reduced Doppler centroid frequency differences (Berardino et al., 2002). The results of the SBAS analysis are mean displacement velocity maps and time series of displacements of each coherent pixel that can be analyzed on their temporal evolution.

We generated a subset of small baseline interferograms with spatial and temporal baselines smaller than 2560 m and shorter than 950 days, respectively, to maintain better coherence. The key requirement in selecting spatial and temporal baselines is to consider nearly all of the

available SAR acquisitions. In result, we analyzed a total of 118 interferograms and removed the topographic effects from the interferograms using the SRTM-X DEM. Next, we applied the Goldstein filter to amplify the phase signal of the generated interferograms (Goldstein and Werner, 1998). Then, we applied three-dimensional unwrapping (Delaunay 3D), which convert each ambiguous 2π cycle to absolute value of interferomic phase and utilize the temporal information (Hooper and Zebker, 2007). Moreover, we applied the 'least-squares inversion after phase-unwrapping' method to retrieve the phase with respect to the original master.

Table 1. ALOS PALSAR data used in the time series analysis. Perpendicular baseline is calculated in relation to 02/06/2008 master image.

	Date (date/month/year)	**Perpendicular baseline (meters)**
1	12/02/2007	302
2	30/06/2007	908
3	15/08/2007	1200
4	30/09/2007	1477
5	31/12/2007	1831
6	15/02/2008	2930
7	01/04/2008	3131
8	17/05/2008	3340
9	02/06/2008	0
10	17/08/2008	-2877
11	02/10/2008	-1871
12	17/11/2008	-1439
13	02/01/2009	-1258
14	17/02/2009	-681
15	20/08/2009	144
16	05/10/2009	609
17	05/01/2010	1099
18	20/02/2010	1799
19	08/07/2010	2087
20	08/10/2010	2463

Furthermore, we retrieved quality and accuracy of the processed data by calculating DEM error, master atmosphere and orbit error from both - small baseline and single master interferograms. Finally, we geocoded the data stack with a spatial resolution of 25 m and obtained mean velocity displacements in the Line of Sight (LOS) direction for the time period between 2007 and 2010. To exclude any linear trends that could influence the subsequent analysis, we de-trended our time series data. We visualized the StaMPS results using viStaMPS software (Sousa et al., 2014) and exported the data into a GIS environment for further interpretation of the ground deformations.

The SBAS retrieved deformation values represent the one-dimensional LOS projection of the actual movement of the earth's surface. In order to overcome the differences between the ground geometry and LOS direction, we projected LOS deformation into the direction of the down slope movement (Cascini et al., 2010). We converted the LOS velocity deformation rates into velocity deformation and to downslope deformation (Vslope) (Cascini et al., 2010; Zhao et al., 2012). In order to transform LOS direction to downslope direction, we require information of the unit LOS vector and the hillslope angle. For the unit LOS vector, we used incidence angle and flight azimuth of the satellite. In addition, we employed hillslope angle, and slope azimuth of the study area, including the calculation of hillslope and azimuth values using SRTM 1 Arc-Second Global elevation data.

4.3.3 Hot-spot and cluster analysis

To detect abnormally slow moving landslides from a large number of point data, we performed hot-spot and cluster analysis. This analysis reveals spatial clusters of similar values and allows to identify regions that exhibit significantly The hot-spot and cluster analysis is based on two statistical approaches the Getis-Ord *Gi* statistic (Getis and Ord, 1992) and kernel density estimation (Silverman, 1986). We performed hot-spot analysis on the mean downslope velocity deformation. First, Getis-Ord Gi* statistics are calculated for each point feature in a dataset. The statistics is based on analyzing the spatial pattern of each feature within the context of its neighbors. A single point feature with a high value may not be a representative measurement and the Getis-Ord Gi* statistics requires that neighbors also have elevated values. In order to be a statistically significant hot spot, a point feature will have a high value and is surrounded by other features with similar values. The local sum for a point feature and its neighbors is compared proportionally to the sum of all features; when the local sum is different from the

expected local sum, and when that difference is too large to be the result of random chance, a statistically significant z-score is assigned to that point. The z-score values tell us where point features with either high or low values cluster spatially. The kernel density estimator is used in order to fit smooth surface as hotspot. The kernel density estimator is performed on downslope velocity point data, choosing derived Gi* as the weighting factor. The output is a smooth kernel density map which converts large amount of point data into several hotspots for better visualization.

4.3.4 Analysis of conformity between topographic surface and geological structures

The degree of conformity between topographic and geological surfaces can be expressed as index of the **to**pographic/**b**edding-plane **i**ntersection **a**ngle (TOBIA) (Meentemeyer and Moody, 2000). When a rock mass contains a distinct bedding plane, TOBIA can be categorized into three basic classes (Cruden and Hu, 1996): If the bedding plane dips in the same direction as the hillslope angle, the hillslope is classified as *cataclinal*. If the bed dips in the direction opposite to the hillslope, then the hillslope is classified as *anaclinal*. Cases where the azimuth of the dip direction is perpendicular to the azimuth of the hillslope direction are referred to as *orthoclinal* slopes. Additional information are in the electronic data repository.

4.3.5 Normalized steepness index (k_{sn})

In order to evaluate long-term tectonic activity we extracted the normalized steepness index (k_{sn}) (Kirby and Whipple, 2012; Wobus et al., 2006). The k_{sn} describes abrupt changes in river channel gradient or elevation because the longitudinal profile is normalized by the channel's drainage area. That is, steep river sections have lower values at small drainage areas, but a similarly steep river section downstream at a larger drainage area will result in high k_{sn} values and often represent knickpoints (Kirby and Whipple, 2012; Neely et al., in review). We exploit the well documented relationship between normalized steepness index and tectonic activity (Bookhagen and Strecker, 2012; Kirby and Whipple, 2001; Ouimet et al., 2009; Scherler et al., 2014). The calculation of the normalized steepness index is based on the analysis of a digital elevation model, where the topography of fluvial channels contain the tectonic history and where local channel slope can be expressed as a power-law function of contributing drainage area (Wobus et al., 2006).

$$S = k_s A^{-\theta} \qquad \text{(equation 1)}$$

where, the S local channel slope, k_s is steepness index and θ is concavity index, A is the upstream drainage area.

These k_sn indices are extracted from the 30m SRTM DEM data using Topotoolbox (Schwanghart and Scherler, 2014). We model channel-profile steepness for the drainage network, small channels and rivers within a drainage area of 1 km^2. Normalized steepness indexes (k_{sn}) have been calculated for a reference channel concavity (θ_{ref}) required for inter-channel interpretation and comparison. We choose a value for $\theta_{ref} = 0.45$ that is equal to the mean of observed concavity values in channel segments (Wobus et al., 2006).

4.4 Results

4.4.1 InSAR-observed velocity deformation and topographic surface

The SBAS results obtained by processing L-band PALSAR data record the location of unstable hillslopes and the downslope deformation velocity. The Vslope displacement rates range between >0 and 71 mm/year and the highest rates are found in regions with prior slope failures (Fig. 3). The high downslope deformation rates are mainly found in the downslope vicinity of existing landslide scarps (Fig. 2). The spatial distribution of point features is scattered and affected by noise. In order to average the point data and obtain a continuous estimate we applied hotspot and kernel density analysis. We identified spatially clustered areas of high values (hotspots), which shows the presence of a large mass movement (Fig.4). From this spatial distribution of deformation values, we selected two large clusters and highlighted them as hotspot cluster I and II (Figure 4). The obtained downslope velocity rate for hotspot cluster I is about 71 mm/yr and for the cluster II about 36 mm/yr. We argue that downslope velocity rates for hotspot cluster I are about 50% or double the rates of hotspot cluster II.

The two distinct spatial clusters (I, II) of increased deformation rates were further analyzed by comparing the SBAS results with topographic parameters along geomorphic profiles drawn across the areas involving the highest deformation rates. We analyzed two profiles across the hotspot clusters I and II (Figs. 3, 4). Profile I with a length of 7 km is transecting through a zone characterized by high displacement rates (Figs. 4, 10). Profile II with a length of about 6 km is located in an area where the high deformation signal can be observed across the slope for an area about 6 km wide and which is covered by several large landslide bodies (Figs. 1, 4, 10). Based on these profiles, we examined the relationship between the mean downslope velocity-

displacement rates and topographic properties (absolute elevation, slope, and flow accumulation derived from the SRTM DEM) along these profiles (Fig. 5).

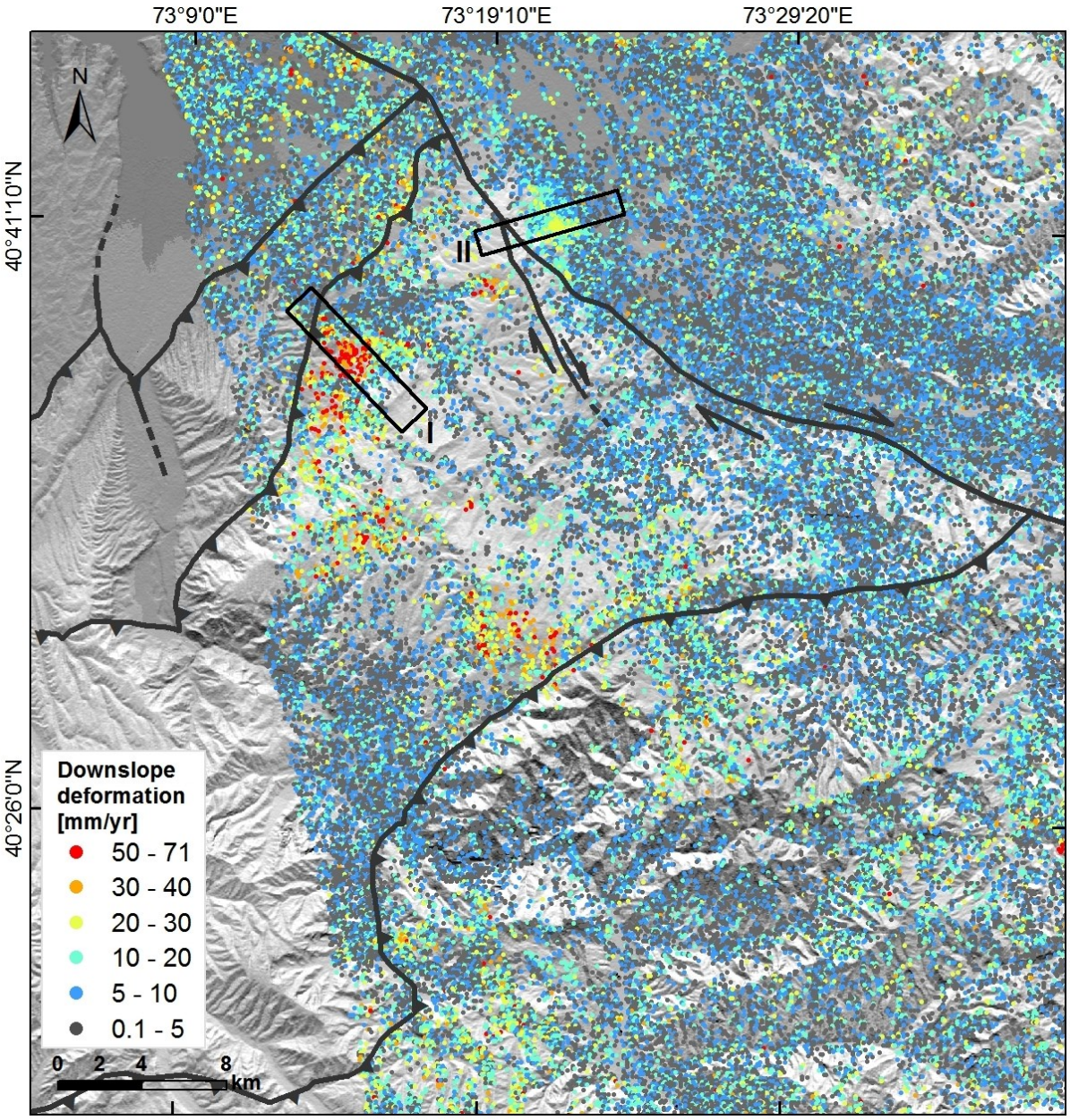

Figure 3. Spatial pattern of InSAR-derived downslope velocity (Vslope) rates (mm/yr) for the time period between 2007 and 2010. The black rectangles represent spatial subsets based on hotspot cluster analyses from (cf. Fig. 4).

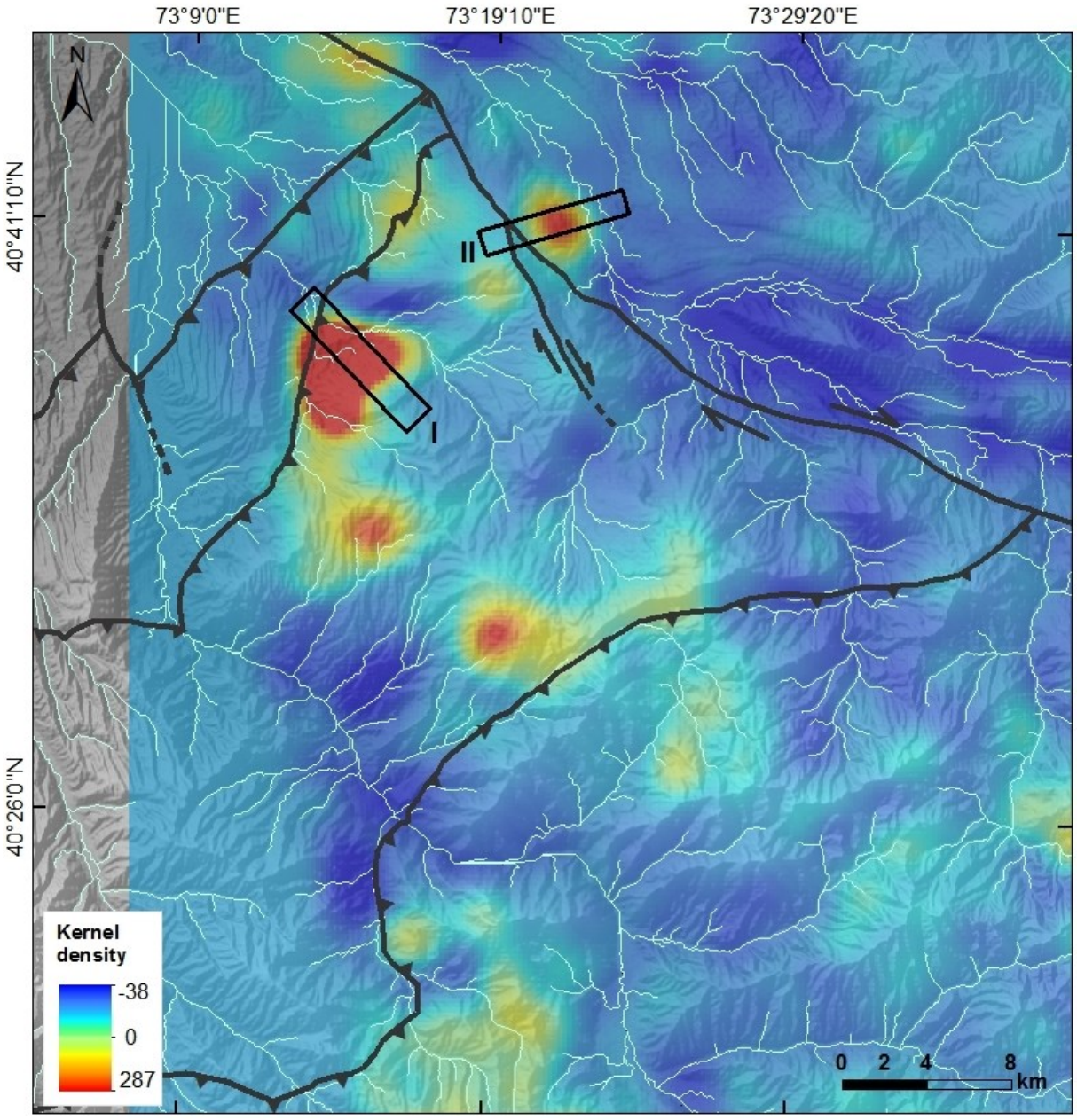

Figure 4. Hotspot cluster kernel density map showing smoothed spatial location of the hotspot clusters in the regions I and II. This analysis shows areas of spatially-correlating regions (i.e., clusters) as high kernel density values in red. Hotspot analysis was performed on downslope velocities.

4.4.1.1 Vslope displacement versus elevation

Plotting the observed Vslope displacement values against the absolute elevation values (Fig. 5a) shows that the observed signals of increased deformation mostly occur in an elevation range between 1000 and 1500 m. Maximum elevations along the slope I amount to about 2000 m, whereas the slope II show slightly higher maximum elevations of up to 2500m. The profiles are characterized by a sharp lower boundary at 1000 m. These observations suggest that the detected landslide reactivations might be facilitated by sliding planes, associated with folded structures in the southern Tien Shan mountain front. However, the verification of this hypothesis requires more detailed field investigations in future.

4.4.1.2 Vslope displacement versus slope angle

In Figure 5 b the downslope displacement values are plotted versus the slope angles for the location of hotspot I and hotspot II. Profile I shows that deformation is distributed between 5 and 25 degrees, whereas the lower-slope values occur in the area close to the thrust fault (Fig. 1). In profile II deformation is related to slope angles between 0 and 30 degrees. The higher maximum slope values reflect the greater steepness of the hotspot area II compared to the hotspot area I. However, the velocity displacement rates measured at the hotspot area II is about two times less compared to the hotspot area I. There is no correlation between the slope angle and downslope velocity displacement rates.

4.4.1.3 Vslope displacement versus flow accumulation

In Figure 5 c the displacement values are plotted versus flow accumulation using a logarithmic scale. The results for hotspot I (Fig. 4) show that the displacement is mainly related to contributing areas of up to 70000 m^2, whereas for hotspot II (Fig. 4) the contributing areas are larger with a maximum of up to 120000 m^2. In the area of hotspot cluster I the observed high deformation rates spatially coincide with the overall flow direction of the local drainage network (Fig. 4). Deformation rates of hotspot cluster II are perpendicular with respect to the overall flow direction of the local drainage network, which corresponds to the strike of the dextral strike-slip fault at the eastern slope. Thus, the area covered by profile A is characterized by a more developed drainage network compared to area of profile B.

4.4.2 Conformity between topographic and geological surfaces

We applied the categorical and continuous TOBIA models using the derived surfaces of slope, slope aspect, bedding dip, and dip direction across the study area. Figures 6 and 7 illustrate spatially distributed estimates of topographic-bedrock intersection angles calculated using the categorical and continuous models, respectively. By overlaying outputs from TOBIA index and hotspot cluster analysis, the conformity between topography/bedding planes and spatial location of slow moving landslides can be represented within each of the classified/indexed slope types (Figs. 4, 6, 7).

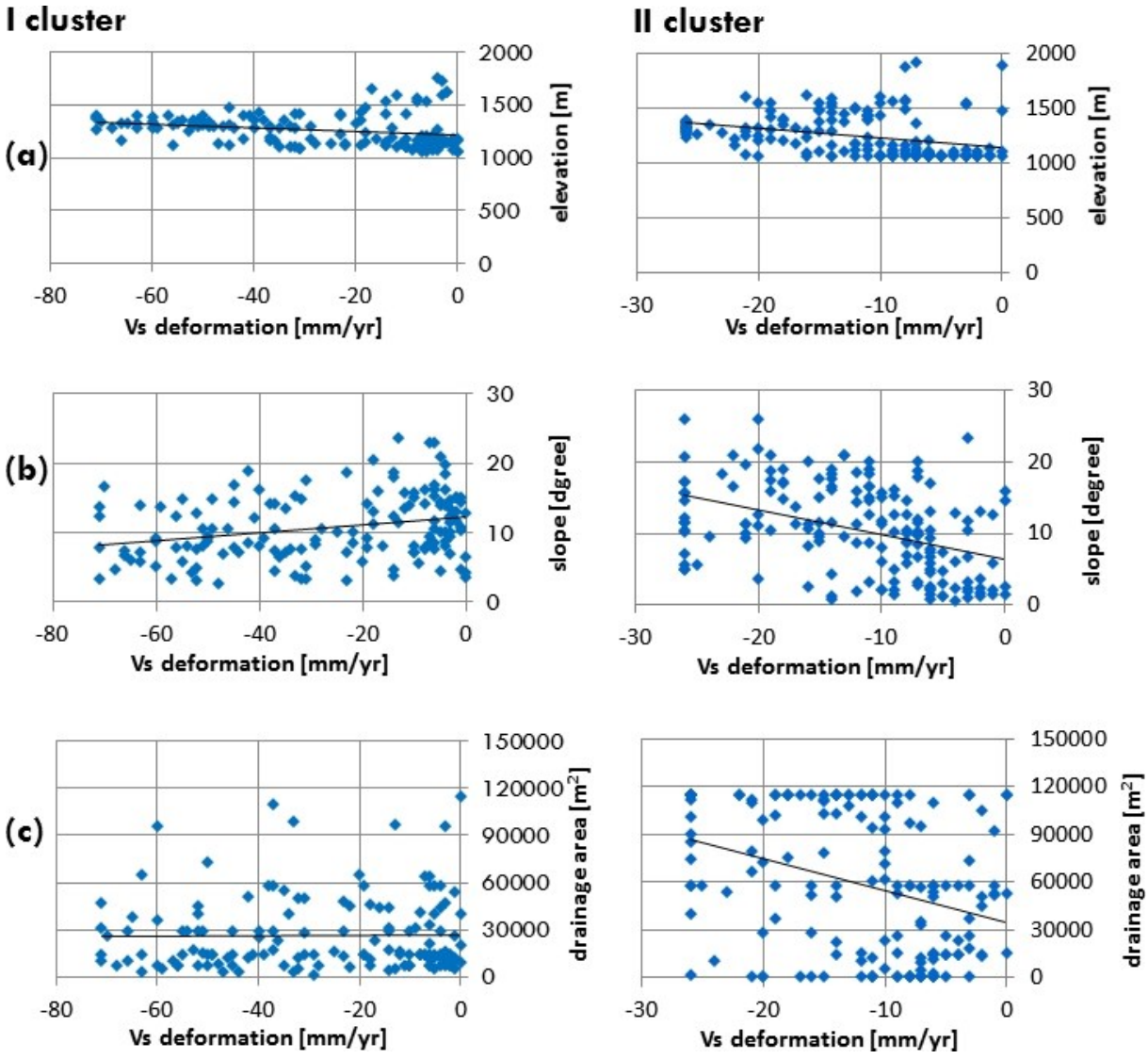

Figure 5. Downslope velocity Vslope displacement rate (mm/yr) plotted against (a) elevation, (b) hillslope angel and (c) flow direction for profiles of hotspot clusters I and II (cf. Figs. 3, 4). This analysis reveals that elevation, hillslope angle, and drainage area do not significantly influence downslope velocities.

The map of classified slopes (Fig. 6) illustrates logical variations in slope types as a function of different slope aspect and dip direction combinations. Most cataclinal slopes correspond to north-west and west-facing terrain. Hotspot I on Figure 6 depicts a cataclinal slope and associated with a relatively shallow slope gradient. Note that the topographic slope is generally north-facing and vary from relatively gentle to steep gradient.

Anaclinal slopes are typically associated with east-facing slopes and compose high percent of map area (hotspot II, Fig. 4, 6). Anaclinal slopes typically occur along steep, moderately inclined slopes, north-east and east-facing hillslopes. Field observations (Fig. 10) indicate that the mapped anaclinal slopes often correspond to the frequently exposed Cretaceous limestone as well as to the most resistant Paleozoic formations. The high occurrence of anaclinal slopes is expected given that the study site is positioned on the front of the mountain range and the dip azimuth is generally north-east-facing as well.

Orthoclinal slopes compose the lowest percent of map area in the study area (Fig. 6). This is not surprising given that the orthoclinal range is twice as less as the cataclinal and anaclinal ranges. Due to the north-east and north-west trending strike of the bedding planes, orthoclinal slopes are typically distributed on south-facing slopes.

The application of the continuous TOBIA index across the watershed (Fig. 7) produces the same general patterns as the map of classified slopes (Fig. 6). Conformity index between slope angles, slope aspect, dip and dip aspect in which high index values (e.g. >0.87) correspond to cataclinal slopes, and low index values (e.g. <0.72) correspond to anaclinal slopes. Moderate index values (0.72 – 0.87) generally correspond to orthoclinal slopes (Fig. 7). Additionally, index values of ridges and drainages are often intermediate between cataclinal and anaclinal slopes as they represent a transition in slope and slope aspect. The advantage of conformity index representation over the classified representation is that it permits greater detail in mapping transitions of topographic/bedding plane intersection angles.

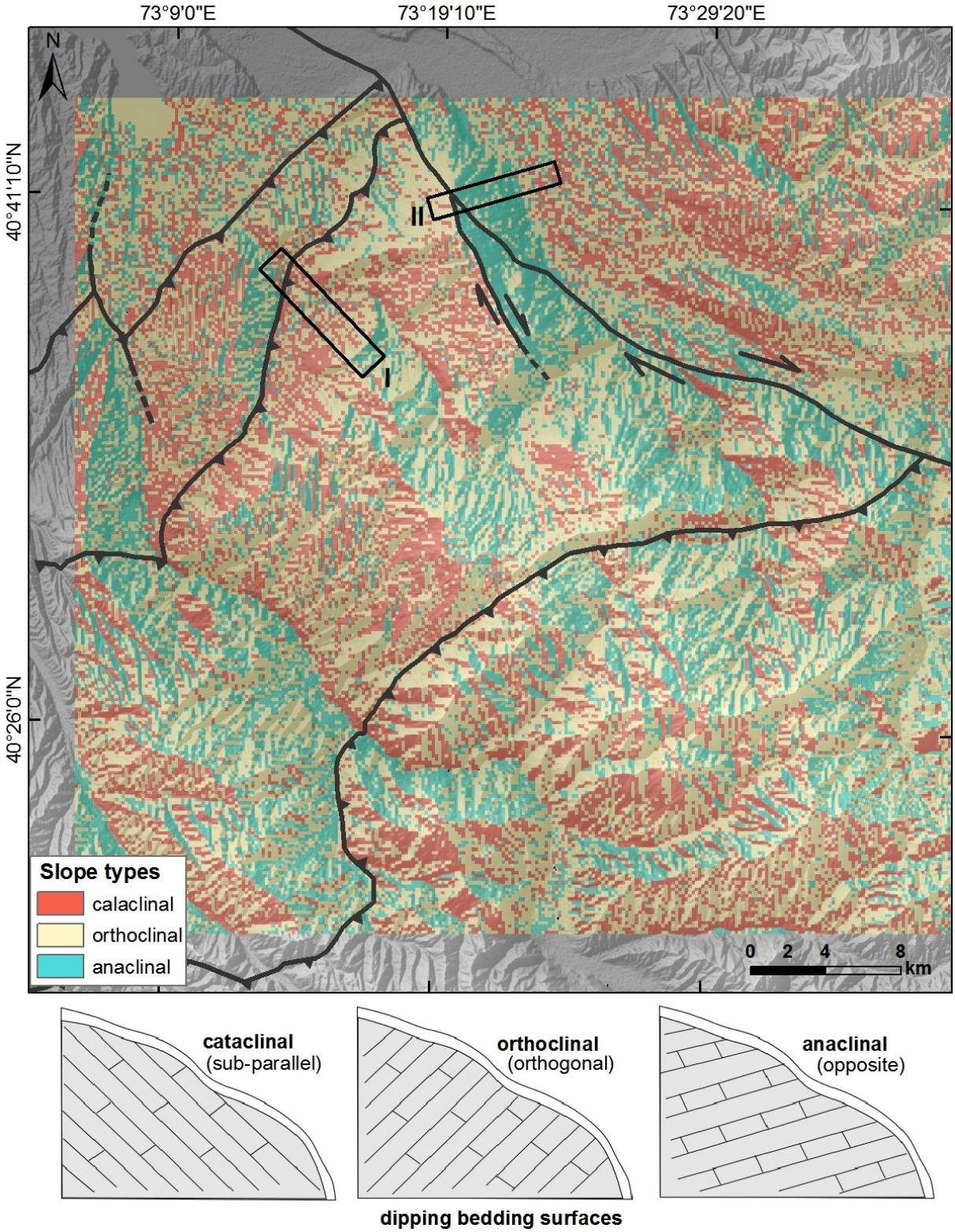

Figure 6. The classified map show cataclinal (bedding plane is parallel to hillslope dip direction), anaclinal (bedding plane is opposite to the hillslope) and orthoclinal slopes (bedding plane is perpendicular to the hillslope) (see cartoon below). Classification of slope types based on spatially-distributed estimates of slope aspect and dip direction angles. This map indicate that cluster I depict a cataclinal slope where bedding plane dips in the same direction as the slope. Cluster II depict anaclinal slope where bed dips in the direction apposite to the slope.

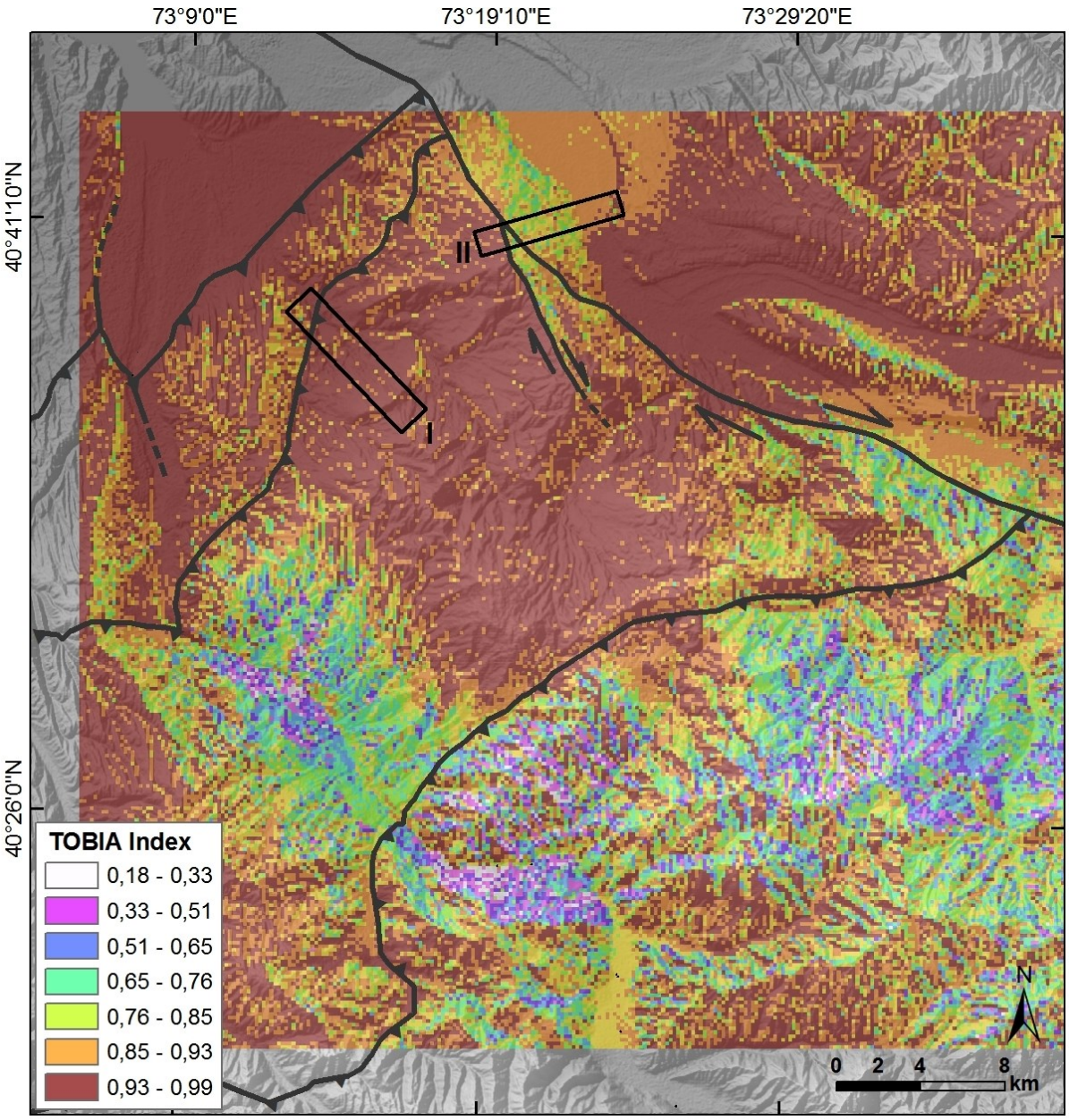

Figure 7. Topography-bedrock intersection index map (TOBIA) show conformity (high index values) and nonconformity (low index values) between slope angles, slope aspect, dip and dip aspect. This map indicates that cluster I is affected by high conformity and cluster II is affected by moderate conformity between topography and bedding planes.

4.5 Discussion

4.5.1 Cause and effect of slope instabilities

4.5.1.1 Implication of active tectonics

We observed downslope velocity deformation rates up to 71 mm/yr within an area of high rates that we have identified as hotspot cluster I (Fig. 4). In addition, a second hotspot II was identified with lower deformation rates of about 30 mm/yr that were characterized by very slow moving slope deformation (Teshebaeva et al., 2015). Similar remote-sensing studies utilizing InSAR detected slow moving slope deformation in Central Italian Apennine's (Tolomei et al., 2013), in the Eastern Betic Cordillera (Spain) (Delgado et al., 2011) and in Bologna in the Po Plain (Italy) (Stramondo et al., 2007).

Our analysis of the observed velocity deformation rates in relation with the elevation, hillslope, and flow direction reveals that the deformation signal does not depend on steepness signals but on lithology and tectonic preconditioning.

Hotspot cluster I is characterized with cataclinal slopes (Figs. 6, 10) located next to an active thrust fault (Fig. 2, 4) and thus, could be activated and shaken during a moderate or large earthquake (Abdrakhmatov et al., 2003). In a previous study, it has been argued that many of the large Kyrgyz Tien Shan rock slope failures occurred on slopes directly truncated by active faults (Strom and Korup, 2006). Here, we hypothesis that landslide are triggered by seismic activity on instable slopes that have been tectonically preconditioned and exhibit a specific structural settings as dip of the planes (Fig. 8). The evidence of enhanced and sustained surface deformation in proximity of active faults (Crozier and Glade, 2006) is underlined by the location of two large earthquakes of 1974 and 2015 in the study area (Fig.1).

However, this is not the case for slope instability identified for the hotspot cluster II. This slope instability is characterized by recently active landsliding of anaclinal slopes (Figs. 6, 10). The mapped breakaway scarps coincide with the surface expression of a major strike-slip fault with inverse and contracting character (Figs. 2, 4). Our hypothesis is that a fault plane origin as sliding surface of the cluster II slope instabilities is associated with the active steeply SW-dipping inverse strike-slip fault (Fig. 9).

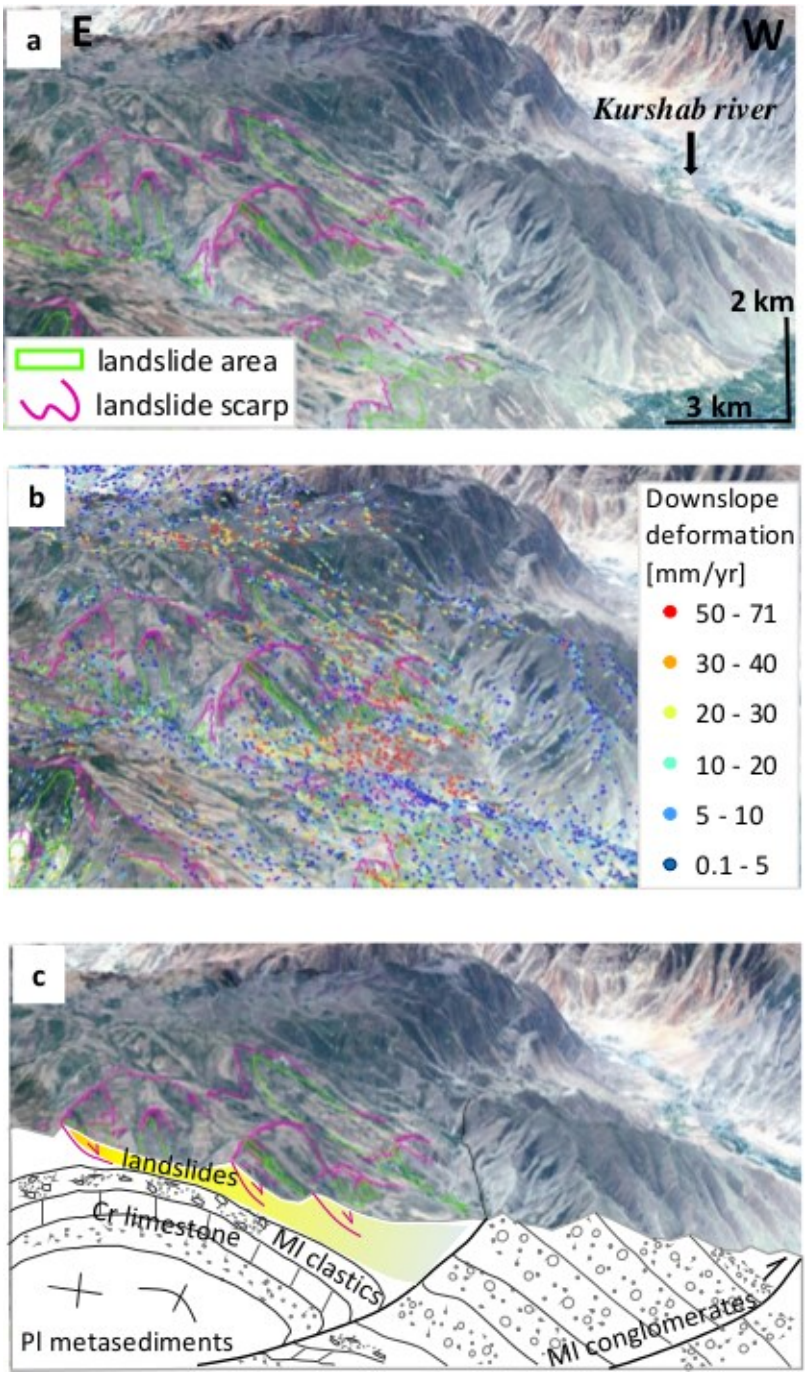

Figure 8. Oblique 3D view of the hot-spot cluster I (Figs. 3, 4) based on optical RapidEye data acquired in August 2014 with (a) mapped landslide areas and scarps, (b) downslope deformation rates and (c) simplified geological cross-section. This cross-section show that cluster I landsliding associated to folded unconsolidated Miocene clastics sediments and Cretaceous limestone/sandstones structures thrusted over Miocene conglomerates.

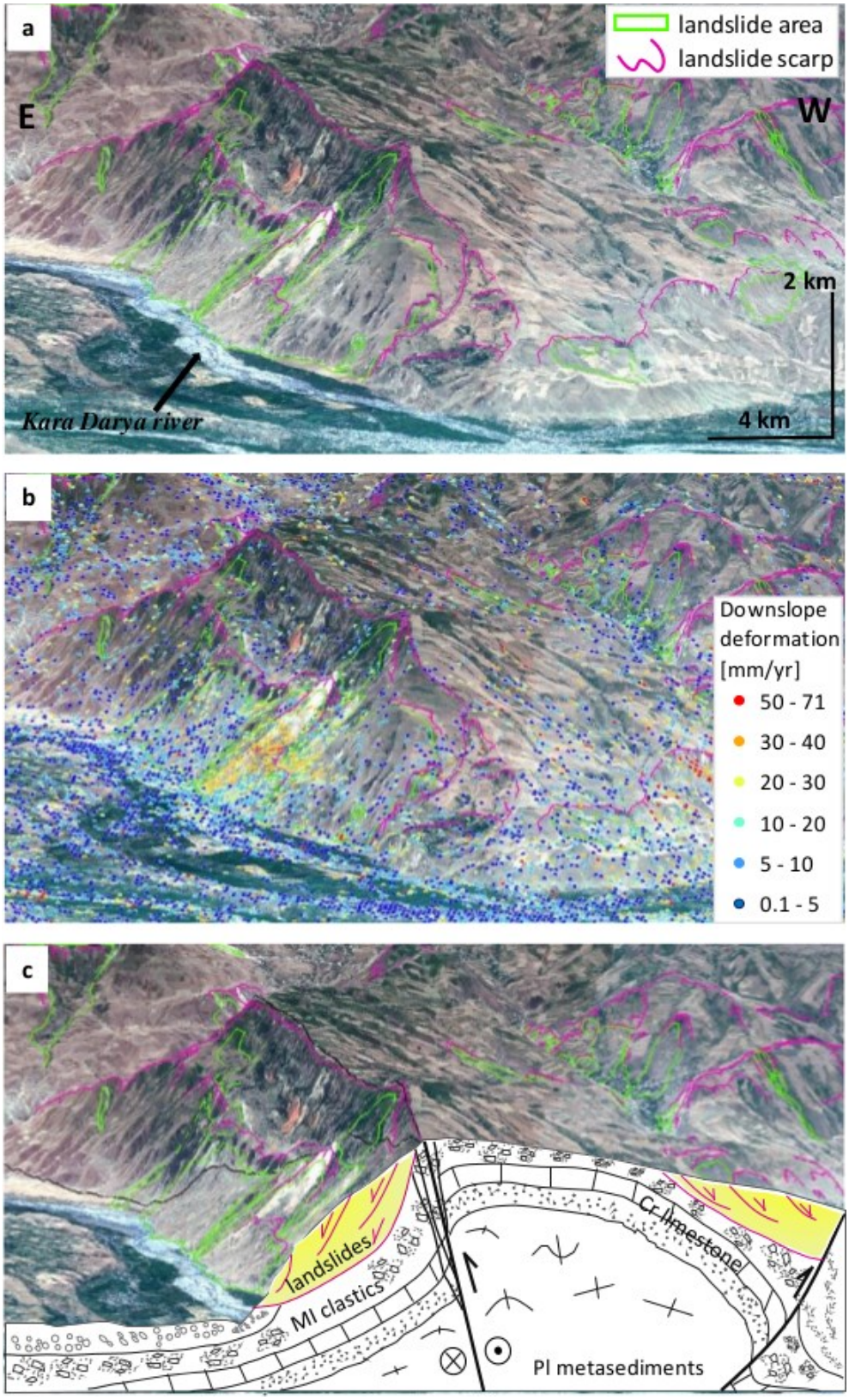

Figure 9. Oblique 3D view of the cluster II (Figs. 3, 4) based on optical RapidEye data acquired in August 2014 with (a) mapped landslide areas and scarps, (b) downslope deformation rates and (c) simplified geological cross-section. This cross-section show that cluster II landsliding associated to unconsolidated Miocene clastics sediments and Cretaceous limestone/sandstones structures. The landsliding is linked to active dextral strike-slip fault that cause slope failures.

The geometry of active tectonic structures (e.g., bedding planes, fold and faults) are often identified as important predisposing factors influencing the failure mechanism of slope instabilities (Agliardi et al., 2001; Agliardi et al., 2009; Ambrosi and Crosta, 2006; Bianchi Fasani et al., 2004; Bouissou et al., 2012; Nemčok et al., 1972). The high degree of conformity between topography and bedding planes (Figs. 6, 7) for the investigated clusters I and II support the hypothesis that the active tectonics with fold and thrust structures (Figs. 8, 9) precondition the site and the rates of the observed very slow moving gravitational phenomena. Overall, the faults and folds exposed in relation with these slopes are closely associated with active tectonics that ultimately cause slope failure in the study area (Figs. 8,9, 10).

4.5.1.2 Lithologic conditioning

The occurrence of continuous downslope moving slope deformation is localized within little or un-consolidated clastic syn-orogenic sedimentary formations mainly Quaternary in age. The phenomenon is exacerbated in cluster I when the folded sequences express bedding planes congruent with the surface and topographic slopes (Agliardi et al., 2009; Ambrosi and Crosta, 2006). We associated our observed hotspot cluster I and II signal with lithological features shown in Figures 2, 12 and 13. The downslope- creeping hills are composed of Plio-Pleistocene loess, Miocene clastics and Cretaceous-Oligocene limestone, evaporitic rocks, or a combination of these rock types (Figs. 8, 9).

For the cluster I, the sliding surfaces are set with alternating weak zones of evaporites and clastics that show bedding planes sub-parallel with the surface (Fig. 8). The cluster II active landsliding area along the steep fault and slope seems to integrate all the Neogene formations above the pre-orogenic Cretaceous-Oligocene limestone (Fig. 9). We hypothesize that the cluster II setting is also influenced by the strong topographic gradient with an average 25 degrees slope and not only the lithology.

4.5.1.3 Climatic influence

High-intensity rain is a critical factor for slope instabilities and catastrophic failures globally, but also in the Kyrgyz Tien Shan (Ibatulin, 2011; Strom and Korup, 2006). Triggering process such a critical slope steepening and debuttressing following deglaciation appear very unlikely for our InSAR observation. Our structures of surficial sliding are at altitudes where major valley glaciers never existed. Moreover our study area is characterized by a prevailing semi-arid climate, which is inferred to have been even drier in the Late Pleistocene and Mid-Holocene (Kovaleva, 2004)

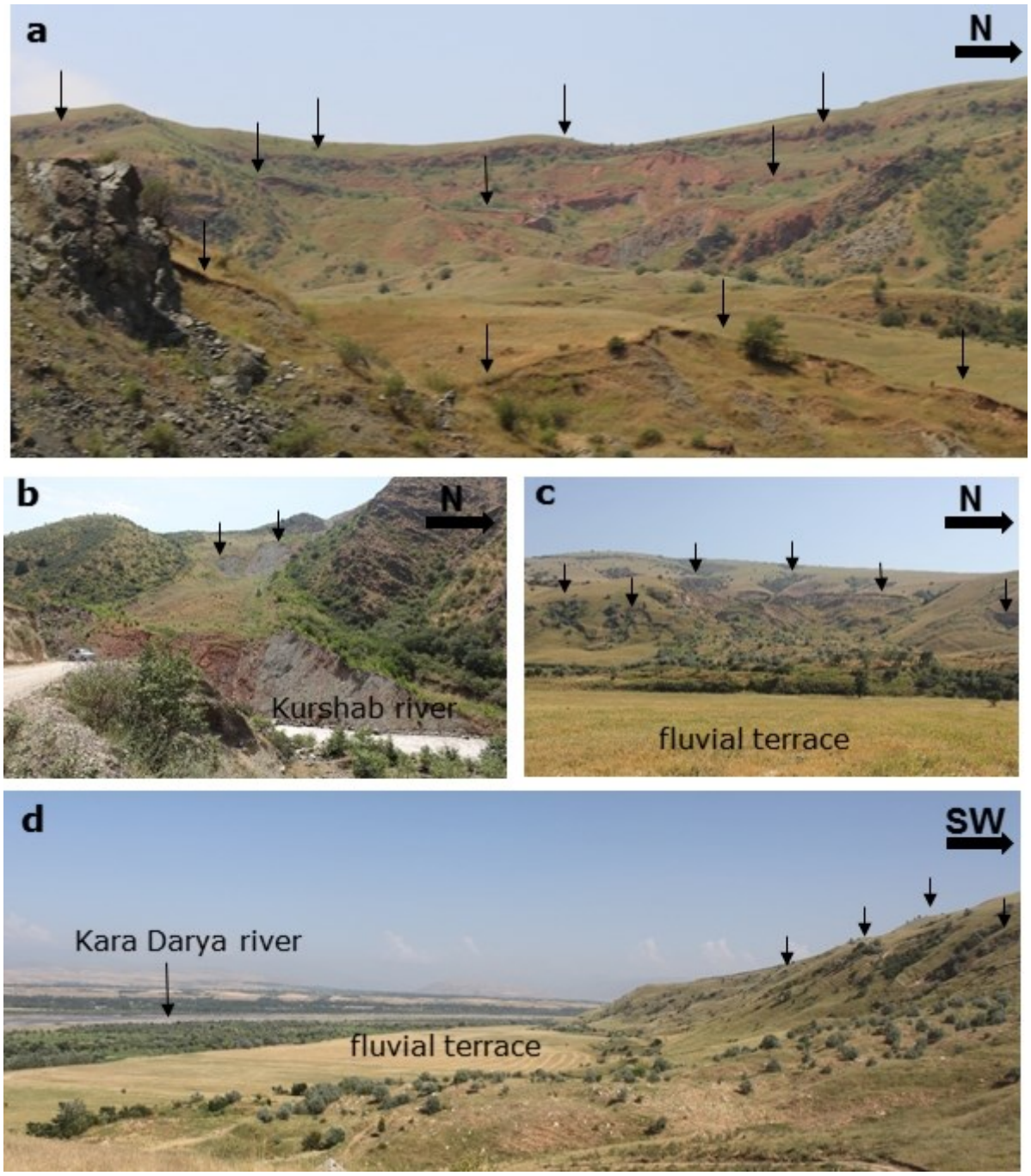

Figure 10. Pictures from the landslide complexes in the study area. Black arrows indicate surface scarps. (a) and (b) from the cluster I area of folded and faulted structures. (c) and (d) from the cluster II area of the strike-slip fault where deep-seated bodies slide over youngest fluvial terrace.

Despite the dominating semi-arid climate, the role of occasional strong precipitation events here should not be underestimated. Some catastrophic failures (e.g., 38 casualties April 2003 and 2004 in the Kara-Taldyk village) were caused by high-intensity rain within the hotspot cluster I area. Daneels et al. (2008) described the development of the 2004 catastrophic failure as a consequence of heavy precipitation filling up cracks generated from seismic deformation during a prior earthquake. Considering our 4-year observation period, we do not observe a direct relation between the rate of slope movements and precipitation. A decadel time series of InSAR observations may provide more hints in that respect.

A key question may be whether the observed very slow movements has the potential to fail within catastrophic dimensions with possible seismic and climatic hazards.
Our observations and the discussion of the main triggering factors emphasize the predominant roles of structural preconditioning, active tectonics, and the litho-structural setting in predicting large-scale slope instability phenomena.

4.5.2 Deformation in space and time

Our analyses reveal that InSAR observed deep-seated slope movements commonly cluster around major tectonic features. It is not clear if the structural features play an active or passive role in the slope movements, i.e. coincides with a zone of stress concentration or with a zone of weak rock. We propose to combine swath profiles and analyzed channel steepness values with InSAR slope movements (Figs. 12, 13).

Our geomorphic analyses suggest that high slope movements rates are coincide with very young morphology and display gentle knickzone of 350-370 k_{sn} values (Fig. 11) at elevations between 1000 and 2400 m (Figs. 12, 13). These slope movements are within unconsolidated Quaternary, Cretaceous, and Miocene sediments. The area is a northward propagating wedge with youngest deformation at northern end, these youngest deformation have unconsolidated lithology. Young deformation and unconsolidated lithologies do not generate steep terrain with high relief and high steepness indices.

The k_{sn} values increase southward with k_{sn} values of 800-900 present comparably stable hillslopes is steep in the Paleozoic basement. This is an example of the terrain with a long history of exhumation in the Paleozoic basement 15-20 km south (Fig. 12). Mode of mass

removal or movement are deep-seated, continuously moving landslides to maintain wedge angle (Davis et al., 1983). High rates of deep-seated landsliding spatially-continuous signal of clusters I and II (Figs. 3, 4, 12, 13). These observations show no climatic gradients in contrast to eastern Andes (Bookhagen and Strecker, 2012), southern Himalaya (Scherler et al., 2014), and eastern Tibet (Kirby and Ouimet, 2011).

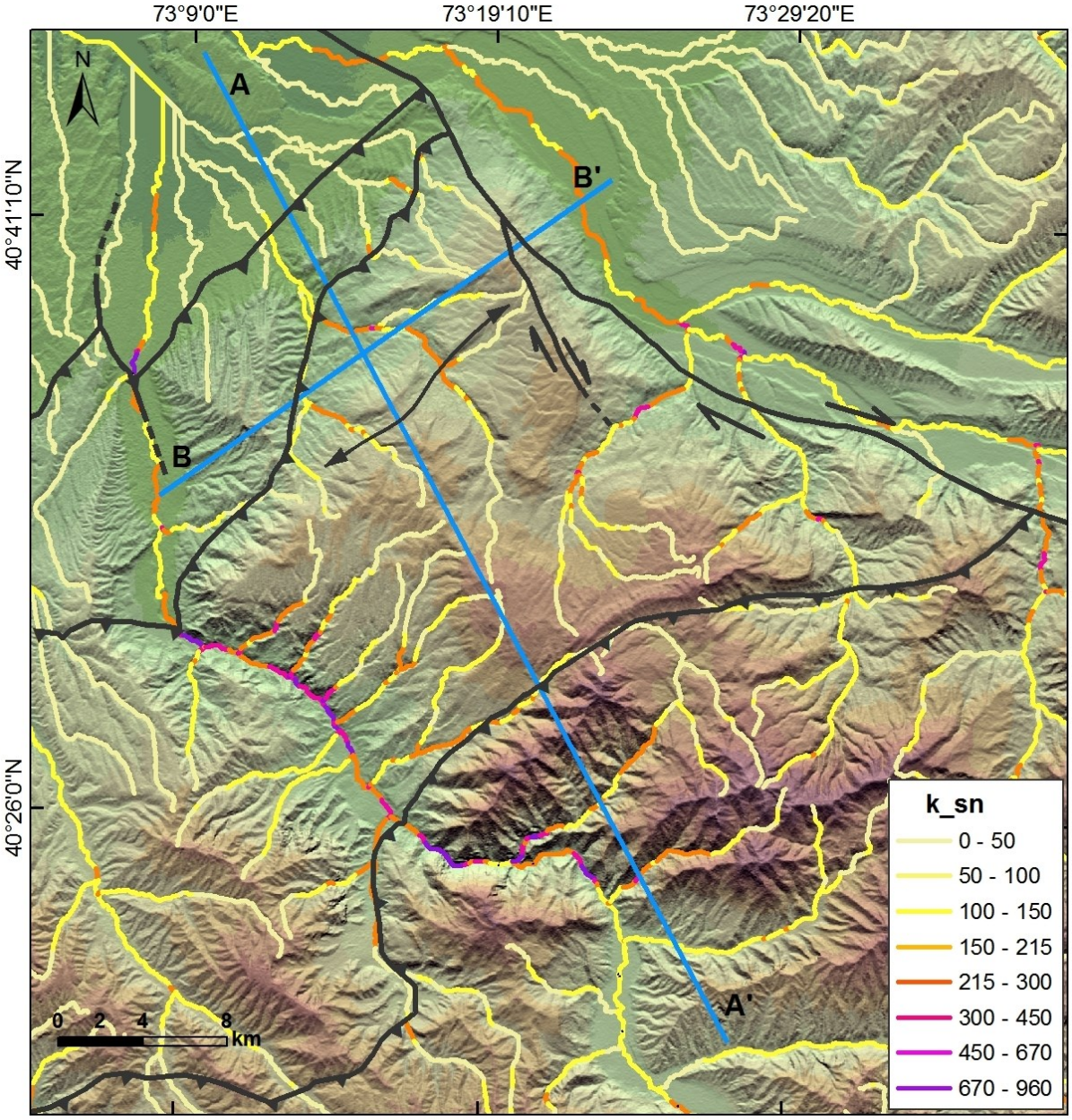

Figure 11. Map of normalized steepness index k_{sn} color-coded by steepness magnitude (theta_ref = -0.45). Main geologic structures (Chediya, 1986) are shown in black overlaid on the topography represented by the SRTM-X DEM.

4.6 Conclusions

In this study, we show results from InSAR and geomorphological investigations on the Alai mountain front in the Kyrgyz Tien Shan. The mountain front is an active fold-and-thrust belt with SW-NE trending and SSW-dipping thrust and inverse faults as well as NW-SE trending conjugate faults. The area is affected by numerous mass movements that are often in the vicinity to tectonically active structures. We analyzed the slope instabilities using InSAR time-series data in conjunction with digital topography, topometric indices, and field observations of tectonic activity and geomorphology. Our InSAR time-series data combined with a spatial cluster analysis revealed two continuously downslope moving areas. The obtained slow moving downslope deformation rates represent deep-seated gravitational slope deformation.–The clusters show no correlation with elevation, hillslope angle and drainage area. In order to test for other factors explaining the spatial distribution of hillslope deformation, we applied a conformity analysis. The high conformity degree between topography and bedding planes show that the spatial distribution of downslope deformation is controlled by the geometry of the folded and faulted structures and their lithology. We conclude that the active tectonics with fold and thrust structures precondition the site and the rates of the observed very slow moving gravitational phenomena. In addition, we evaluated long-term tectonic activity and extracted the normalized steepness index. The k_{sn} values correlate with unconsolidated lithologies and is not an appropriate metric of tectonic deformation for this study.

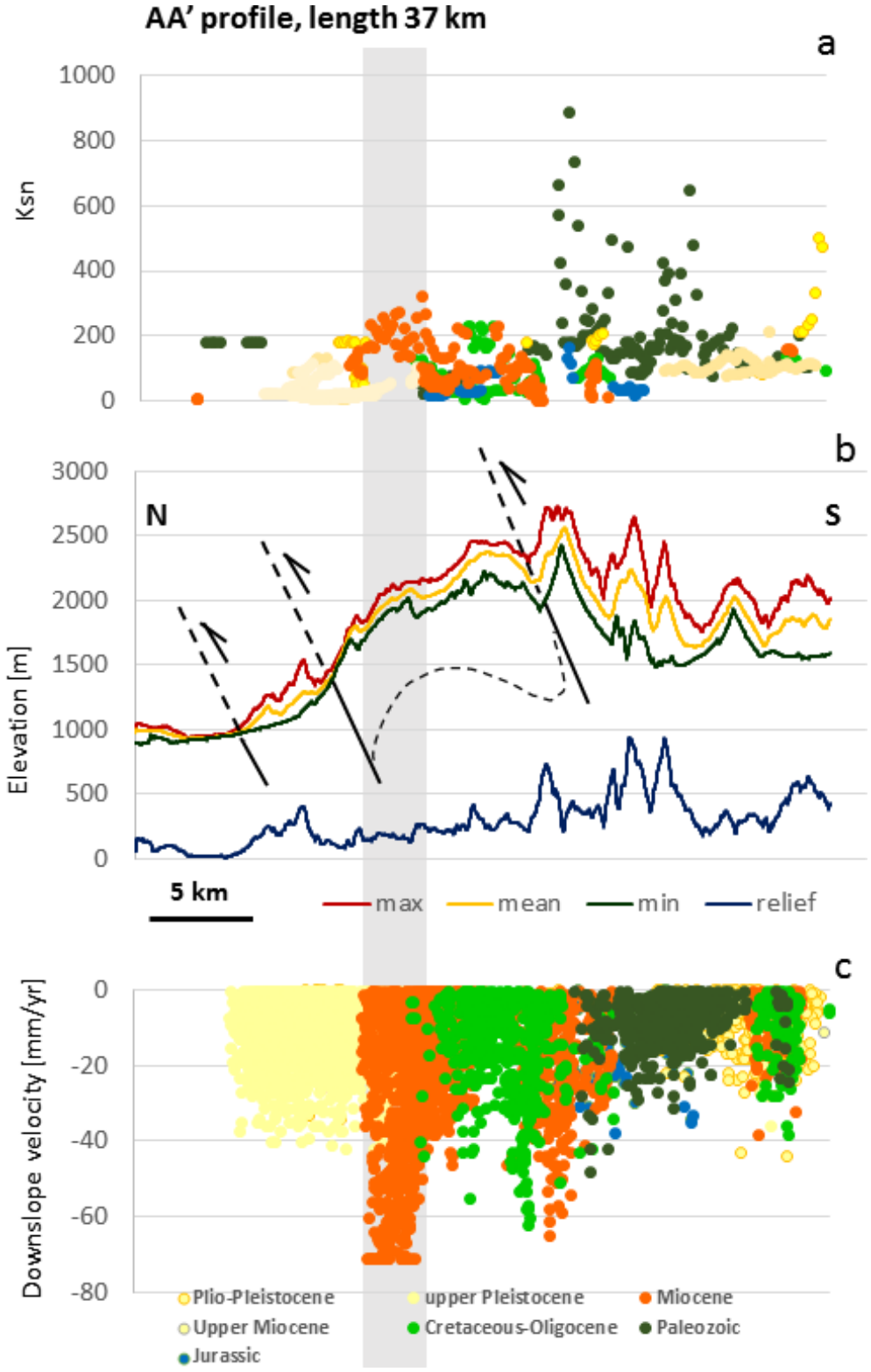

Figure 12. Swath and relief profile AA' (Figs. 1, 11) of topography related to k_{sn} trend and downslope velocity rates crossing the cluster I shown in Figs. 4 and 8: (a) trend plot of k_{sn} values in the channel reaches; (b) swath and relief profiles are plotted with simplified structures; (c) plot represents downslope velocity rates.

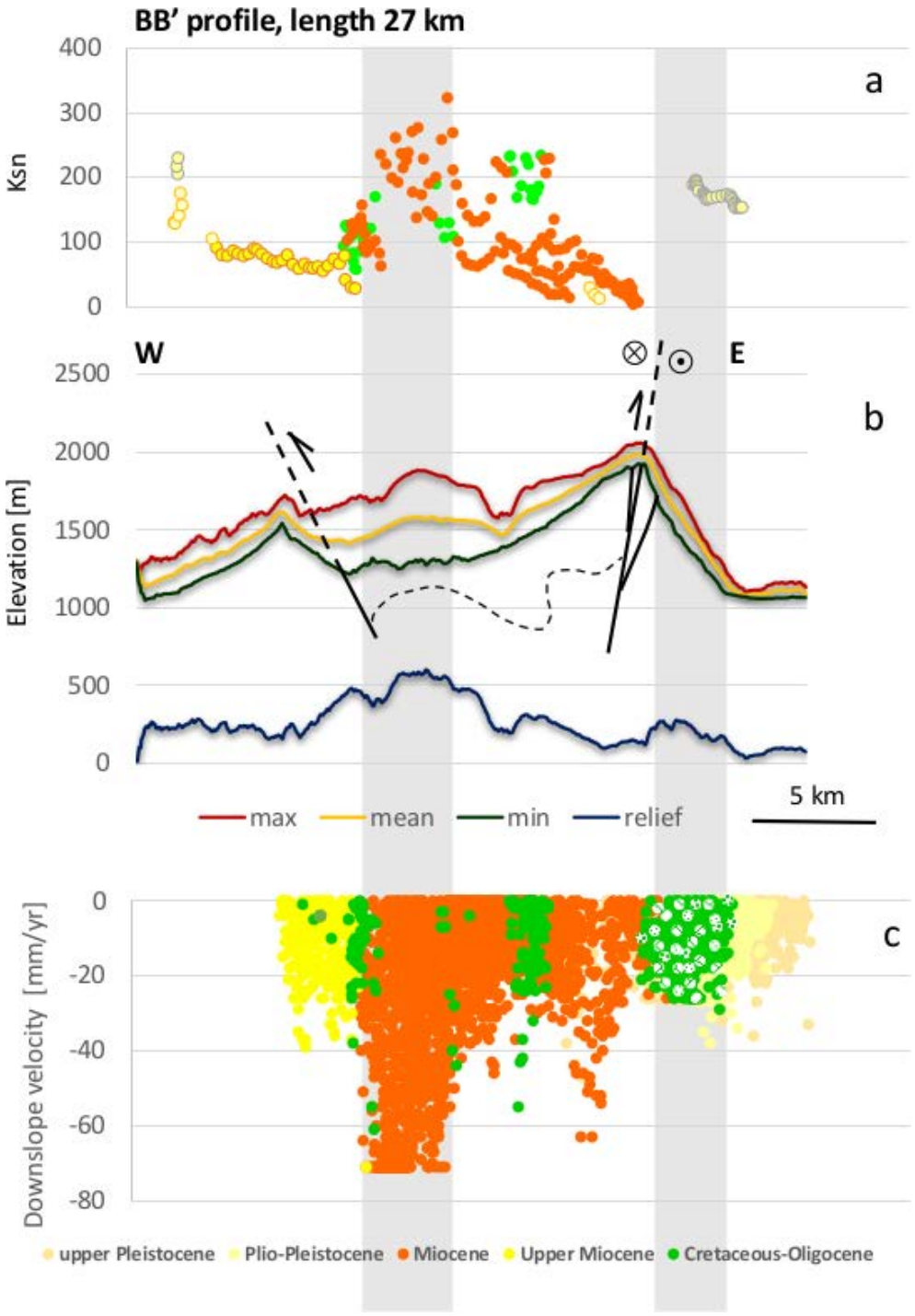

Figure 13. Swath and relief profile BB' (Fig. 1, 2) of topography related to k_{sn} trend and downslope velocity rates crossing the cluster II shown in Fig.4 and 9: (a) trend plot of k_{sn} values in the channel reaches; (b) swath and relief profiles are plotted with simplified structures; (c) plot represents downslope velocity rates.

Acknowledgments

We thank Sigrid Roessner, Oliver Korup and Bolot Moldobekov for valuable discussions, which helped to improve the content of the paper. This research was funded by the Volkswagen foundation within the frame of the LUCA (Land Use, Ecosystem Services and Human Welfare in Central Asia) post-graduate programme. The work was supported by the Central Asia and Afghanistan Research Fellowship (CAARF) and the German Research Foundation (DFG) under the auspices of the Graduate School GRK1364 "Shaping Earth's Surface in a variable Environment" (Strecker STR 373/18-1). This work was also supported by the CAWa project (www.cawa-project.net) funded by the German Federal Foreign Office as part of the German Water Initiative for Central Asia. The ALOS data for this study were provided by the Japanese Aerospace Agency (JAXA) through the research proposal P610.

REFERENCES

Abdrakhmatov, K., H.-B. Havenith, D. Delvaux, D. Jongmans, and P. Trefois, 2003, Probabilistic PGA and arias intensity maps of Kyrgyzstan (Central Asia): Journal of Seismology, v. 7, p. 203-220.

Agliardi, F., G. Crosta, and A. Zanchi, 2001, Structural constraints on deep-seated slope deformation kinematics: Engineering Geology, v. 59, p. 83-102.

Agliardi, F., G. B. Crosta, and P. Frattini, 2012, 18 Slow rock-slope deformation: Landslides: Types, Mechanisms and Modeling, p. 207.

Agliardi, F., A. Zanchi, and G. B. Crosta, 2009, Tectonic vs. gravitational morphostructures in the central Eastern Alps (Italy): constraints on the recent evolution of the mountain range: Tectonophysics, v. 474, p. 250-270.

Ambrosi, C., and G. B. Crosta, 2006, Large sackung along major tectonic features in the Central Italian Alps: Engineering Geology, v. 83, p. 183-200.

Arrowsmith, J. R., and M. Strecker, 1999, Seismotectonic range-front segmentation and mountain-belt growth in the Pamir-Alai region, Kyrgyzstan (India-Eurasia collision zone): Geological Society of America Bulletin, v. 111, p. 1665-1683.

Bazhenov, M., 1993, Cretaceous paleomagnetism of the Fergana basin and adjacent ranges, central Asia: tectonic implications: Tectonophysics, v. 221, p. 251 - 267.

Behling, R., S. Roessner, H. Kaufmann, and B. Kleinschmit, 2014, Automated Spatiotemporal Landslide Mapping over Large Areas Using RapidEye Time Series Data: Remote Sensing, v. 6, p. 8026-8055.

Berardino, P., G. Fornaro, R. Lanari, and E. Sansosti, 2002, A new algorithm for surface deformation monitoring based on small baseline differential SAR interferograms: Geoscience and Remote Sensing, IEEE Transactions on, v. 40, p. 2375-2383.

Bianchi Fasani, G., C. Esposito, A. Maffei, G. Scarascia Mugnozza, and S. Evans, 2004, Geological controls on slope failure style of rock avalanches in Central Apennines (Italy): Landslides: Evaluation and stabilization, Lacerda, Ehrlich, Fontoura & Sayao (eds), v. 1, p. 501-507.

Biske, Y. S., 1996, Paleozoic Structure and History of Southern Tian-Shan: Leningrad University, Leningrad, p. 187.

Bookhagen, B., and M. R. Strecker, 2012, Spatiotemporal trends in erosion rates across a pronounced rainfall gradient: Examples from the southern Central Andes: Earth and Planetary Science Letters, v. 327, p. 97-110.

Bouissou, S., R. Darnault, A. Chemenda, and Y. Rolland, 2012, Evolution of gravity-driven rock slope failure and associated fracturing: Geological analysis and numerical modelling: Tectonophysics, v. 526, p. 157-166.

Burtman, V., 2000, Cenozoic crustal shortening between the Pamir and Tien Shan and a reconstruction of the Pamir-Tien Shan transition zone for the Cretaceous and Palaeogene: Tectonophysics, v. 319, p. 69 - 92.

Burtman, V., 2006, The Tien Shan Early Paleozoic tectonics and geodynamics: Russian Journal of Earth Sciences, v. 8, p. 1-23.

Buslov, M., J. De Grave, E. Bataleva, and V. Batalev, 2007, Cenozoic tectonic and geodynamic evolution of the Kyrgyz Tien Shan Mountains: a review of geological, thermochronological and geophysical data: J Asian Earth Sci, v. 29, p. 205 - 214.

Cascini, L., G. Fornaro, and D. Peduto, 2010, Advanced low- and full-resolution DInSAR map generation for slow-moving landslide analysis at different scales: Engineering Geology, v. 112, p. 29-42.

Cobbold, P., P. Davy, D. Gapais, E. Rossello, E. Sadybakasov, J. Thomas, J. Tondji Biyo, and M. De Urreiztieta, 1993a, Sedimentary basins and crustal thickening: Sediment Geol, v. 86, p. 77 - 89.

Cobbold, P., E. Sadybakasov, and J. Thomas, 1994, Cenozoic transpression and basin development, Kyrgyz TienShan, Central Asia.: Geodynamic Evolution of Sedimentary Basins, International Symposium.: Moscow.

Cobbold, P., E. Sadybakasov, and J. Thomas, 1996, Cenozoic transpression and basin development, Kyrgyz Tien Shan: Central Asia, in Geodynamic Evolution of Sedimentary Basins, edited by F. Roure et al, p. 181-202.

Colesanti, C., A. Ferretti, C. Prati, and F. Rocca, 2003, Monitoring landslides and tectonic motions with the Permanent Scatterers Technique: Engineering Geology, v. 68, p. 3-14.

Colesanti, C., and J. Wasowski, 2006, Investigating landslides with space-borne synthetic aperture radar (SAR) interferometry: Engineering Geology, v. 88, p. 173-199.

Crozier, M. J., and T. Glade, 2006, Landslide hazard and risk: issues, concepts and approach: Landslide hazard and risk. Wiley, West Sussex, p. 1-40.

Cruden, D., and X. Hu, 1996, Hazardous modes of rock slope movement in the Canadian Rockies: Environmental & Engineering Geoscience, v. 2, p. 507-516.

Danneels, G., C. Bourdeau, I. Torgoev, and H. B. Havenith, 2008, Geophysical investigation and dynamic modelling of unstable slopes: case-study of Kainama (Kyrgyzstan): Geophysical Journal International, v. 175, p. 17-34.

Delgado, J., F. Vicente, F. García-Tortosa, P. Alfaro, A. Estévez, J. López-Sánchez, R. Tomás, and J. Mallorquí, 2011, A deep seated compound rotational rock slide and rock spread in SE Spain: structural control and DInSAR monitoring: Geomorphology, v. 129, p. 252-262.

Dikau, R., 1996, Landslide recognition: identification, movement, and clauses, Wiley.

Duethmann, D., J. Zimmer, A. Gafurov, A. Güntner, D. Kriegel, B. Merz, and S. Vorogushyn, 2013, Evaluation of areal precipitation estimates based on downscaled reanalysis and station data by hydrological modelling: Hydrol. Earth Syst. Sci., v. 17, p. 2415-2434.

Farr, T. G., and M. Kobrick, 2000, Shuttle radar topography mission produces a wealth of data: EOS Transactions, v. 81, p. 583-585.

Feld, C., C. Haberland, B. Schurr, C. Sippl, H.-U. Wetzel, S. Roessner, M. Ickrath, U. Abdybachaev, and S. Orunbaev, 2015, Seismotectonic study of the Fergana Region (Southern Kyrgyzstan): distribution and kinematics of local seismicity: Earth, Planets and Space, v. 67, p. 40.

Galadini, F., 2006, Quaternary tectonics and large-scale gravitational deformations with evidence of rock-slide displacements in the Central Apennines (central Italy): Geomorphology, v. 82, p. 201-228.

Getis, A., and J. K. Ord, 1992, The analysis of spatial association by use of distance statistics: Geographical analysis, v. 24, p. 189-206.

Ghose, S., M. Hamburger, and C. Ammon, 1998, Source parameters of moderate sized earthquakes in the Tien Shan, central Asia from regional moment tensor inversion: Geophys Res Lett, v. 25, p. 3181 - 3184.

Goldstein, R. M., and C. L. Werner, 1998, Radar interferogram filtering for geophysical applications: Geophysical Research Letters, v. 25, p. 4035-4038.

Gori, S., E. Falcucci, F. Dramis, F. Galadini, P. Galli, B. Giaccio, P. Messina, A. Pizzi, A. Sposato, and D. Cosentino, 2014, Deep-seated gravitational slope deformation, large-scale rock failure, and active normal faulting along Mt. Morrone (Sulmona basin, Central Italy): Geomorphological and paleoseismological analyses: Geomorphology, v. 208, p. 88-101.

Haberland, C., U. Abdybachaev, B. Schurr, H. Wetzel, S. Roessner, A. Sarnagoev, S. Orunbaev, and C. Janssen, 2011, Landslides in southern Kyrgyzstan: understanding tectonic controls: Eos Trans AGU, v. 92, p. 20.

Hooper, A., 2008, A multi-temporal InSAR method incorporating both persistent scatterer and small baseline approaches: Geophysical Research Letters, v. 35.

Hooper, A., and H. A. Zebker, 2007, Phase unwrapping in three dimensions with application to InSAR time series: Journal of the Optical Society of America a-Optics Image Science and Vision, v. 24, p. 2737-2747.

Ibatulin, K. V., 2011, Monitoring of landslides in Kyrgyzstan. Ministry of Emergency Situations of the Kyrgyz Republic, p. 145.

Ischuk, A., R. Bendick, A. Rybin, P. Molnar, S. F. Khan, S. Kuzikov, S. Mohadjer, U. Saydullaev, Z. Ilyasova, and G. Schelochkov, 2013, Kinematics of the Pamir and Hindu Kush regions from GPS geodesy: Journal of Geophysical Research: Solid Earth, v. 118, p. 2408-2416.

Jomard, H., T. Lebourg, and Y. Guglielmi, 2014, Morphological analysis of deep-seated gravitational slope deformation (DSGSD) in the western part of the Argentera massif. A morpho-tectonic control?: Landslides, v. 11, p. 107-117.

Kirby, E., and K. Whipple, 2001, Quantifying differential rock-uplift rates via stream profile analysis: Geology, v. 29, p. 415-418.

Kirby, E., and K. X. Whipple, 2012, Expression of active tectonics in erosional landscapes: Journal of Structural Geology, v. 44, p. 54-75.

Kirscher, U., A. Zwing, D. Alexeiev, H. Echtler, and V. Bachtadse, 2013, Paleomagnetism of Paleozoic sedimentary rocks from the Karatau Range, Southern Kazakhstan: Multiple remagnetization events correlate with phases of deformation: Journal of Geophysical Research: Solid Earth, v. 118, p. 3871-3885.

Kovaleva, N., 2004, Northern Tian-Shan paleosoil sedimentary sequences as a record of major climatic events: Revista mexicana de ciencias geológicas, v. 21, p. 71-78.

Lanari, R., F. Casu, M. Manzo, G. Zeni, P. Berardino, M. Manunta, and A. Pepe, 2007, An Overview of the Small BAseline Subset Algorithm: a DInSAR Technique for Surface Deformation Analysis: Pure and Applied Geophysics, v. 164, p. 637-661.

Meentemeyer, R. K., and A. Moody, 2000, Automated mapping of conformity between topographic and geological surfaces: Computers & Geosciences, v. 26, p. 815-829.
Mohadjer, S., R. Bendick, A. Ischuk, S. Kuzikov, A. Kostuk, U. Saydullaev, S. Lodi, D. Kakar, A. Wasy, and M. Khan, 2010, Partitioning of India-Eurasia convergence in the Pamir-Hindu Kush from GPS measurements: Geophysical Research Letters, v. 37.
Molnar, P., and P. Tapponnier, 1975, Cenozoic tectonics of Asia: effects of a continental collision: Science, v. 189, p. 419 - 426.
Nemčok, A., J. Pašek, and J. Rybář, 1972, Classification of landslides and other mass movements: Rock Mechanics, v. 4, p. 71-78.
Ni, J., and J. E. York, 1978, Late Cenozoic tectonics of the Tibetan plateau: Journal of Geophysical Research: Solid Earth (1978–2012), v. 83, p. 5377-5384.
Ouimet, W. B., K. X. Whipple, and D. E. Granger, 2009, Beyond threshold hillslopes: Channel adjustment to base-level fall in tectonically active mountain ranges: Geology, v. 37, p. 579-582.
Reigber, C., G. W. Michel, R. Galas, D. Angermann, J. Klotz, J. Y. Chen, A. Papschev, R. Arslanov, V. E. Tzurkov, and M. C. Ishanov, 2001, New space geodetic constraints on the distribution of deformation in Central Asia: Earth and Planetary Science Letters, v. 191, p. 157-165.
Roessner, S., H. Wetzel, H. Kaufmann, and A. Sarnagoev, 2005, Potential of satellite remote sensing and GIS for landslide hazard assessment in Southern Kyrgyzstan (Central Asia): Nat Hazards, v. 35, p. 395 - 416.
Scherler, D., B. Bookhagen, and M. R. Strecker, 2014, Tectonic control on 10Be-derived erosion rates in the Garhwal Himalaya, India: Journal of Geophysical Research: Earth Surface, v. 119, p. 83-105.
Schwanghart, W., and D. Scherler, 2014, Short Communication: TopoToolbox 2–MATLAB-based software for topographic analysis and modeling in Earth surface sciences: Earth Surface Dynamics, v. 2, p. 1-7.
Sengör, A., B. Natal'In, and V. Burtman, 1993, Evolution of the Altaid tectonic collage and Palaeozoic crustal growth in Eurasia: Nature, v. 364, p. 299-307.
Silverman, B. W., 1986, Density estimation for statistics and data analysis, v. 26, CRC press.
Sobel, E. R., J. Chen, L. M. Schoenbohm, R. Thiede, D. F. Stockli, M. Sudo, and M. R. Strecker, 2013, Oceanic-style subduction controls late Cenozoic deformation of the Northern Pamir orogen: Earth and Planetary Science Letters, v. 363, p. 204-218.
Sousa, J. J., P. Guimarães, A. Sousa, A. M. Ruiz, G. Patrício, L. Magalhães, and F. Pereira, 2014, viStaMPS – A Collaborative Project for StaMPS-MTI Results Interpretation: Procedia Technology, v. 16, p. 842-848.
Stramondo, S., M. Saroli, C. Tolomei, M. Moro, F. Doumaz, A. Pesci, F. Loddo, P. Baldi, and E. Boschi, 2007, Surface movements in Bologna (Po Plain—Italy) detected by multitemporal DInSAR: Remote Sensing of Environment, v. 110, p. 304-316.
Strecker, M., W. Frisch, M. Hamburger, L. Ratschbacher, S. Semiletkin, A. Zamoruyev, and N. Sturchio, 1995, Quaternary deformation in the eastern Pamirs, Tadzhikistan and Kyrgyzstan: Tectonics, v. 14, p. 1061-1079.
Strom, A. L., and O. Korup, 2006, Extremely large rockslides and rock avalanches in the Tien Shan Mountains, Kyrgyzstan: Landslides, v. 3, p. 125-136.
Teshebaeva, K., S. Roessner, H. Echtler, M. Motagh, H.-U. Wetzel, and B. Molodbekov, 2015, ALOS/PALSAR InSAR Time-Series Analysis for Detecting Very Slow-Moving Landslides in Southern Kyrgyzstan: Remote Sensing, v. 7, p. 8973-8994.
Tolomei, C., A. Taramelli, M. Moro, M. Saroli, D. Aringoli, and S. Salvi, 2013, Analysis of the deep-seated gravitational slope deformations over Mt. Frascare (Central Italy) with

geomorphological assessment and DInSAR approaches: Geomorphology, v. 201, p. 281-292.
Wetzel, H. U., Roessner, S., and Sarnagoev, A., 2000, Remote sensing and GIS based geological mapping for assessment of landslide hazard in Southern Kyrgyzstan (Central Asia): Management Information Systems 2000 - GIS and Remote Sensing, p. 355-366.
Windley, B. F., D. Alexeiev, W. Xiao, A. Kröner, and G. Badarch, 2007, Tectonic models for accretion of the Central Asian Orogenic Belt: Journal of the Geological Society, v. 164, p. 31-47.
Wobus, C., K. X. Whipple, E. Kirby, N. Snyder, J. Johnson, K. Spyropolou, B. Crosby, and D. Sheehan, 2006, Tectonics from topography: Procedures, promise, and pitfalls: Geological Society of America Special Papers, v. 398, p. 55-74.
Yerokhin, S. A., 1999, Investigation of landslide occurence in Osh and Djalalabad provinces of the Kyrgyz Republic., Bishkek, Institute of Geology.
Zhao, C. Y., Z. Lu, Q. Zhang, and J. de la Fuente, 2012, Large-area landslide detection and monitoring with ALOS/PALSAR imagery data over Northern California and Southern Oregon, USA: Remote Sensing of Environment, v. 124, p. 348-359.
Zubovich, A., X. Wang, Y. Scherba, G. Schelochkov, R. Reilinger, C. Reigber, O. Mosienko, P. Molnar, W. Michajljow, V. Makarov, J. Li, S. Kuzikov, T. Herring, M. Hamburger, B. Hager, Y. Dang, V. Bragin, and R. Beisenbaev, 2010, GPS velocity field for the Tien Shan and surrounding regions: Tectonics, v. 29.

5. Summary and conclusions

This work intends to contribute to a better understanding of natural surface processes and hazards associated with active mountain building processes in the Pamir - Tien Shan region. Two natural hazard phenomena present the main focuses of this dissertation. First, we investigated the 2008 Nura earthquake that occurred in the high-relief and not accessible area of the northern Pamir. Second, we investigated deep-seated slow moving landslide phenomena in the Alai mountain front in the southern Tien Shan.

(1) First case study - coseismic surface deformation of the 2008 Nura earthquake

We quantified and modeled coseismic surface deformation using two techniques and four independent datasets of ascending L-band ALOS/PALSAR imagery as well as descending C-band ENVISAT imagery. We used two-pass DInSAR technique and in addition we used pixel offset technique due to loss of coherence in rugged high relief areas of the analysed region. Our DInSAR coseismic surface deformation results guided the field work in 2012, when we found and measured surface ruptures that were not found during 2008 field work. These measured surface displacements in combination with geological observations and seismological data enhanced our understanding of active tectonics in a structurally complex continental collision zone. We found that the 2008 Nura earthquake (Mw 6.6) ruptured an imbricated thrust system. This thrust system is part of the Pamir Frontal thrust and constitutes a fold-and-thrust belt in the eastern convex transition of the Trans Alai range, where it collides with the Tien Shan to the north. The Irkeshtam fault at the deformation front is a moderate-angle decollement fault that seems to be aseismic and controlled by mechanically weak evaporites lubricating the fault. This fault was coseismically activated by the Nura earthquake, as documented by prominent surface ruptures and fractured boulders along the trace of the fault, whereas the earthquake nucleated at the back-range Pamir Frontal thrust. The Nura earthquake thus activated dip-slip thrusting and sinistrally oblique thrusting on the kinematically connected Pamir Frontal thrust and the Irkeshtam fault. This event presents an example of coseismic strain partitioning in a tectonically active collision zone, which is characterized by a northward propagating orogenic wedge toward the Tien Shan mountains.

(2) Second case study – surface deformation related to deep-seated landslides

At first step, we estimated the potential of L-band ALOS/PALSAR imagery using satellite InSAR time-series to observe slope instabilities in high relief and vegetated areas of the Alai range of southern Tien Shan. The Alai mountain front is an active fold-and-thrust belt with SW-NE trending and SSW-dipping thrust and inverse faults as well as NW-SE trending conjugate faults. The area is affected by numerous mass movements that are often in the vicinity to active structures. Satellite InSAR time-series analysis has resulted in very slow and temporally uniform landslide movements, which have occurred during the time period from 2007 to 2010. We detected and observed two distinct very slow-moving deep-seated landslides in the Alai mountain front. Further analyses of the temporal evolution of these very slow-moving landslide show that the local seismicity and the prior 3-month precipitation amounts contribute to the activation of landslide prone slopes.

In the next step, we showed the results from InSAR and geomorphological investigations. We analyzed the slope instabilities using InSAR time-series data in conjunction with an analysis of digital topography, tectonic geomorphology and lithology. Our InSAR time-series data revealed two clusters of continuous slow moving downslope deformation areas. These clusters of enhanced movements show no correlation with elevation, hillslope and flow direction. Further, we applied a conformity analysis between surface topography and geological structures that show spatial distribution of two clusters have good correlation between surface topography and bedding planes. These results support the hypothesis of the importance of tectonic precondition in predicting slope instabilities. Slow-moving landslides detected by InSAR represent active deep-seated gravitational slope deformation phenomena which is first time observed in the Tien Shan mountains. The spatial distribution is controlled by the geometry of the folded and faulted structures and their lithology. The observed deformation represent essential information for longer-term InSAR monitoring, assessment and mitigation of hazard in the region. Our results show that such multidisciplinary approaches deliver important additional information on predicting slope failures. The presented combination describes valuable tool to better understand the spatial distribution of deep-seated slope deformation phenomena in tectonically active mountainous regions.

Thus, it can be concluded that the results obtained by the two case studies provide valuable information about surface deformations and can be used concurrently to assess both short- and longer-term tectonic activity in the region. Both cases show the high potential of satellite InSAR analysis for the understanding of surface processes related with earthquake and landslide activities. This study also underlines that the integration of additional data sets relevant for surface processes like meteorology or seismology contribute to a better understanding of the underlying processes and thus to an improved assessment of natural risks for disaster prevention. This studies results show that L-band missions are a very important tool for the longer-term monitoring of slope instabilities in mountainous regions. The new opportunities from the recently launched PALSAR-2 and Sentinel-1 missions will largely widen the potential of these techniques in future. Especially in Central Asia where the topographic challenges are extremely high and mountains societies are highly endangered by natural risks the radar remote-sensing techniques and acquisition capabilities present a prosperous and sustained tool; this will increase the opportunity for the development of operational satellite InSAR-based monitoring systems complementary to ground-based slope observations (e.g. GPS). The combined analyses of the obtained InSAR time-series results with additional natural hazards related information will support regular process monitoring as part of a quantitative hazard and risk assessment may contribute effectively to an early warning system in all tectonically active and high hazardous regions of Central Asia.

Annex 1

Supplementary Material. Strain partitioning at the eastern Pamir-Alai revealed through SAR data analysis of the 2008 Nura earthquake

1.1 Processed SAR data

Table S1. Processed interferograms, bold letters denote the interferograms used in the analyses and model estimation.

	Pass	Track	Frame	Master (year/month/day)	Slave (year/month/day)	Baseline perpendicular [m]
ALOS/PALSAR						
1	Asc	527	780	2008/11/17	2007/09/30	-2729.50
2	Asc	527	780	2008/11/17	2008/02/15	-4145.11
3	Asc	527	780	2008/11/17	2008/04/01	-4322.26
4	Asc	527	780	2008/11/17	2008/05/17	-4565.30
5	Asc	527	780	2008/11/17	2008/07/02	-1276.47
6	Asc	527	780	2008/11/17	2008/08/17	1531.52
7*	Asc	527	780	2008/11/17	2008/10/02	491.93
8	Asc	527	780	2009/01/02	2007/09/30	-2614.07
9	Asc	527	780	2009/01/02	2008/04/01	-4206.85
10	Asc	527	780	2009/01/02	2008/05/17	-4449.89
11	Asc	527	780	2009/01/02	2008/08/17	1647.01
12	Asc	527	780	2009/01/02	2008/10/02	607.41
13	Asc	527	780	2009/01/02	2008/11/17	115.48
14	Asc	527	780	2009/02/17	2008/02/15	-3367.44
15*	**Asc**	**527**	**780**	**2008/07/02**	**2009/08/20**	**90.01**
16	Asc	527	780	2009/08/20	2008/08/17	2898.59

Table S2. Processed interferograms continued.

	Pass	Track	Frame	Master (year/month/day)	Slave (year/month/day)	Baseline perpendicular [m]
ENVISAT/ASAR						
1*	**Desc**	**234**	**2817**	**2008/05/08**	**2009/05/28**	**131.494**
2	Desc	234	2817	2008/05/08	2008/10/30	66.69
3	Desc	234	2817	2008/08/21	2008/10/30	112.23
4	Desc	234	2817	2008/09/25	2008/10/30	308.34
5	Desc	234	2817	2008/09/25	2009/05/28	379.86
6	Desc	234	2817	2008/09/25	2009/04/23	115.51
7	Desc	234	2817	2008/09/25	2009/03/19	739.25

1.2 Model results

We show here the test results for the hypothesis that only the Irkeshtam fault has been activated during the Nura earthquake. Based on our SAR surface displacement measurements we run an optimization with the two segments of the Irkeshtam fault only and without the activation of the Pamir Frontal thrust (Figs. S2, S3). Otherwise the optimization settings remained unchanged. In particular for the ALOS InSAR data the Irkeshtam-only model shows less good data fit (Fig. S2, b).

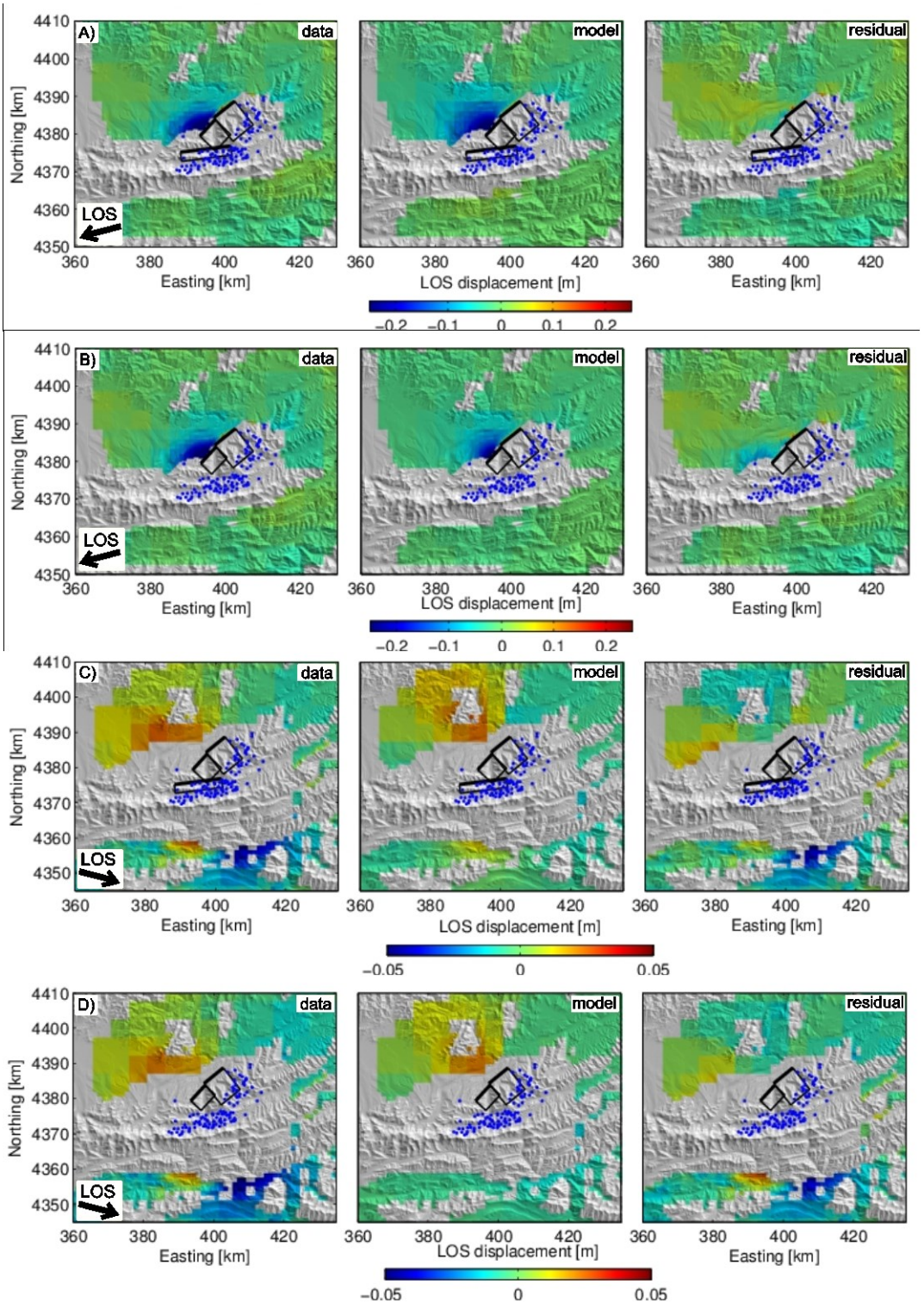

Figure S2. Model results for a) ALOS InSAR data and c) ENVISAT InSAR data for the two-fault model involving an activated Pamir Frontal thrust and the Irkeshtam fault (same as in Fig. 4 in the main article) compared against a one-fault model (b and d), respectively, involving only the Irkeshtam fault. The map-projected fault segments are marked in solid black lines, where thick lines mark the upped edge. Aftershock locations are shown in blue dots.

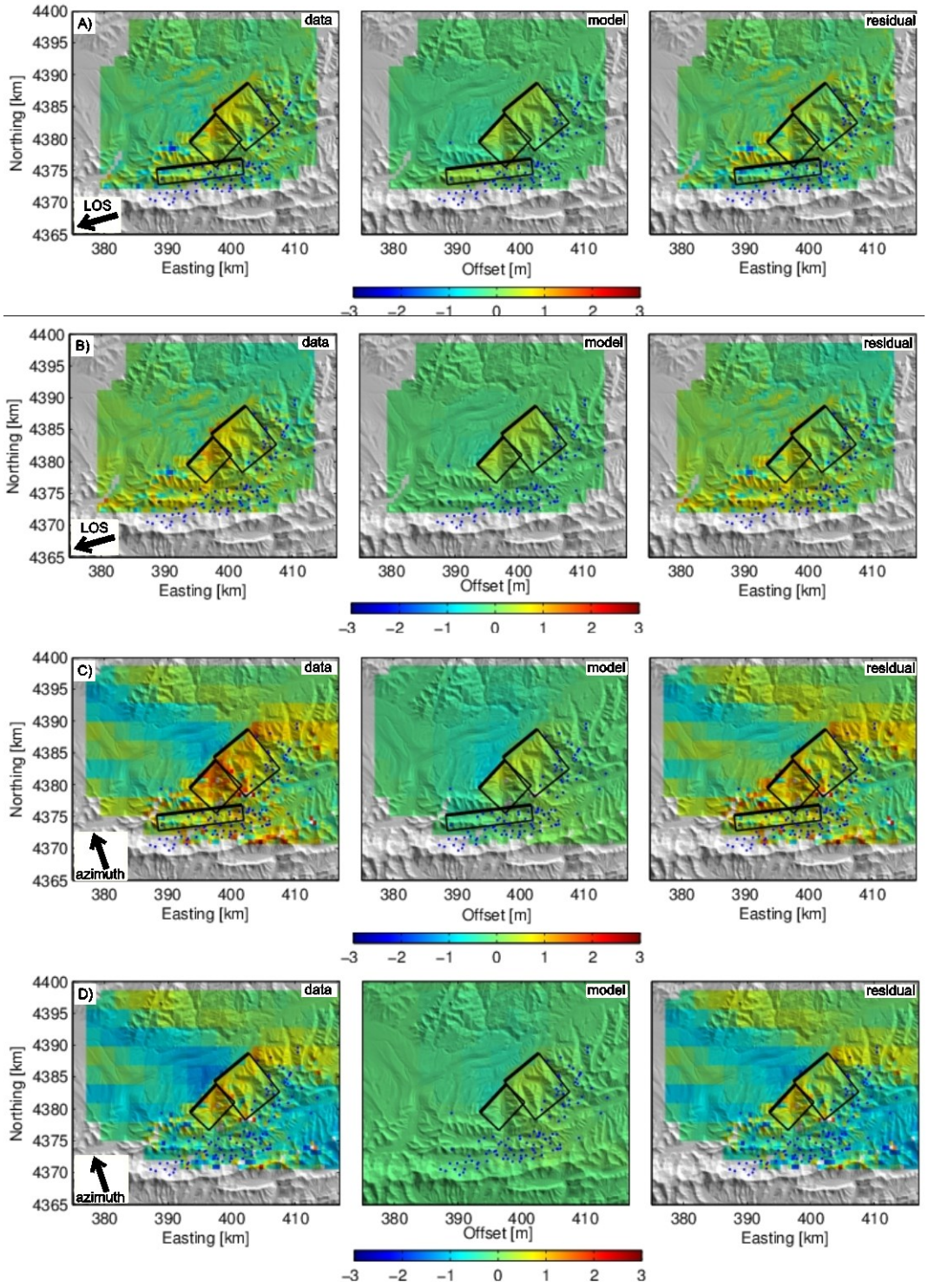

Figure S3. Model results for ALOS a) range pixel offsets and c) azimuth pixel offsets for the two-fault model involving an activated Pamir Frontal thrust and the Irkeshtam fault (same as in Fig. 5 in the main article) compared against a one-fault model (b and d), respectively, involving only the Irkeshtam fault. The map-projected fault segments are marked in solid black lines, where thick lines mark the upped edge. Aftershock locations are shown in blue dots.

Annex 2

Styles of surface deformation in the southern Kyrgyz Tien Shan revealed from InSAR analyses and tectonic geomorphology

Supplementary data repository:

Calculation of a topographic/bedding-plane intersection angle at a given point requires four variables: topographic hillslope angle (S; 0-90^0), hillslope aspect (A; 0-360^0), bedding dip (θ; 0-90^0) and dip direction (α; 0-360^0). TOBIA can be modeled either (1) categorically or (2) continuously.

(1) Categorical modeling – classification of slopes

Using hillslope angle, slope aspect, dip, and dip direction, the slopes are classified into cataclinal, anaclinal, and orthoclinal types based on the conformity between dip direction and slope aspect. In order to determine the difference between α and A for classified slopes, we compute the chord length subtended by the angle between α and A on the unit circle. The chord describes a continuous function between zero and two on the unit circle (Meentemeyr and Moody, 2000). The chord length is:

$$L = \sqrt{(cos \propto -cosA)^2 + (sin \propto -sinA)^2} \quad \text{(equation 1)}$$

Each slope type is then classified based on the chord length ranges and expressed as:
if $0 \leq L \leq 0.7654$ then cataclinal slopes ($0^0 \pm 45^0$)
if $0.7654 < L \leq 1.8478$ then orthoclinal slopes ($90^0 \pm 45^0$ or $270^0 \pm 25^0$)
if $1.8478 < L \leq 2$ then anaclinal slopes ($180^0 \pm 45^0$)

(2) Continuous modeling – conformity index

Topographic/bedding plane intersection angles (TOBIA) can also be modeled in a continuous manner. An index of TOBIA can be expressed continuously as after Meentemeyr and Moody, (2000):

$$TOBIA = \cos\theta \cos S + \sin\theta \sin S \cos(\alpha - A) \qquad \text{(equation 2)}$$

The model calculates an index of conformity between topography and a bedding plane. Index values range from one to negative one. More details on TOBIA modeling can be found in Meentemeyr and Moody (2000).

The models described above are applied using mapped geologic data and SRTM DEM in a standard GIS environment. We derived hillslope angle and aspect surfaces from the 30-meter SRTM DEM. Next, we digitized 202 strike/dip points within study area from geological maps to obtain spatially distributed field of strike and dip. The strike data were adjusted 90 degree in order to obtain dip direction. Ordinary kriging was used to spatially interpolate dip and dip direction surfaces from digitized points (Meentemeyr and Moody, 2000). Furthermore, the classified slopes and index of conformity between topographic surface and geological structures were correlated with hotspot clusters of the InSAR velocity deformation rates.

REFERENCES

Arrowsmith, J. R., and M. Strecker, 1999, Seismotectonic range-front segmentation and mountain-belt growth in the Pamir-Alai region, Kyrgyzstan (India-Eurasia collision zone): Geological Society of America Bulletin, v. 111, p. 1665-1683.

Bazhenov, M., 1993, Cretaceous paleomagnetism of the Fergana basin and adjacent ranges, central Asia: tectonic implications: Tectonophysics, v. 221, p. 251 - 267.

Biske, Y. S., 1996, Paleozoic Structure and History of Southern Tian-Shan: Leningrad University, Leningrad, p. 187.

Burtman, V., 2000, Cenozoic crustal shortening between the Pamir and Tien Shan and a reconstruction of the Pamir-Tien Shan transition zone for the Cretaceous and Palaeogene: Tectonophysics, v. 319, p. 69 - 92.

Burtman, V., 2006, The Tien Shan Early Paleozoic tectonics and geodynamics: Russian Journal of Earth Sciences, v. 8, p. 1-23.

Cobbold, P., E. Sadybakasov, and J. Thomas, 1996, Cenozoic transpression and basin development, Kyrgyz Tien Shan: Central Asia, in Geodynamic Evolution of Sedimentary Basins, edited by F. Roure et al, p. 181-202.

Coutand, I., Strecker, M.R., Arrowsmith, R., Hilley, G., Thiede, R.C., Korjenkov, A. & Omuraliev, M., 2002. Late Cenozoic tectonic development of the intramontane Alai Valley (Pamir-Tien Shan region, Central Asia): an example of intracontinental deformation due to the Indo-Eurasia collision, Tectonics, 21(6), doi:10.1029/2002TC001358.

Fialko, Y., Sandwell, D., Simons, M. & Rosen, P., 2005. Three-dimensional deformation caused by the Bam, Iran, earthquake and the origin of shallow slip deficit Nature, 435, 295–299.

Ibatulin, K. V., 2011, Monitoring of landslides in Kyrgyzstan. Ministry of Emergency Situations of the Kyrgyz Republic, p. 145.

Kalmetieva, Z.A., Mikolaichuk, A.V., Moldobekov, B.D., Meleshko, A.V., Jantaev, M.M. & Zubovich, A.V., 2009. The atlas of earthquakes in Kyrgyzstan. CAIAG Bishkek, 76, ISBN 978-9967-25-829-7.

Meentemeyer, R. K., and A. Moody, 2000, Automated mapping of conformity between topographic and geological surfaces: Computers & Geosciences, v. 26, p. 815-829.

Michel, R. & Rignot, E., 1999. Flow of glacier Moreno, Argentina, from repeat-pass Shuttle Imaging Radar images: comparison of the phase correlation method with radar interferometr y, J. Glaciol., 45(149), 93– 100.

Molnar, P., and P. Tapponnier, 1975, Cenozoic tectonics of Asia: effects of a continental collision: Science, v. 189, p. 419 - 426.

Reigber, C., G. W. Michel, R. Galas, D. Angermann, J. Klotz, J. Y. Chen, A. Papschev, R. Arslanov, V. E. Tzurkov, and M. C. Ishanov, 2001, New space geodetic constraints on the distribution of deformation in Central Asia: Earth and Planetary Science Letters, v. 191, p. 157-165.

Rosen, P., Henley, S., Peltzer, G. & Simons, M., 2004. Updated Repeat Orbit Interferometr y Package Released, EOS, Trans. Am. geophys. Un., 85(5), 47.

Sobel, E. R., J. Chen, L. M. Schoenbohm, R. Thiede, D. F. Stockli, M. Sudo, and M. R. Strecker, 2013, Oceanic-style subduction controls late Cenozoic deformation of the Northern Pamir orogen: Earth and Planetary Science Letters, v. 363, p. 204-218.

Strecker, M., W. Frisch, M. Hamburger, L. Ratschbacher, S. Semiletkin, A. Zamoruyev, and N. Sturchio, 1995, Quaternary deformation in the eastern Pamirs, Tadzhikistan and Kyrgyzstan: Tectonics, v. 14, p. 1061-1079.

Strecker, M.R., Hilley, G.E., Arrowsmith, J.R. & Coutand, I., 2003. Differential structural and geomorphic mountain-front evolution in an active continental collision zone: the NW Pamir, southern Kyrgyzstan, Geol. soc. Am. Bull., 115, 166–181.

Wasowski, J., & Bovenga, F. (2014). Investigating landslides and unstable slopes with satellite Multi Temporal Interferometry: Current issues and future perspectives. Engineering Geology, 174, 103-138. Retrieved from <Go to ISI>://WOS:000335630500009

Wright, T.J., Parson, B.E. & Lu, Z., 2004. Towards mapping surface deformation in three dimensions using InSAR, Geophys. Res. Lett., 31(1), doi:10.1029/2003GL018827.

Zhao, C. Y., Z. Lu, Q. Zhang, and J. de la Fuente, 2012, Large-area landslide detection and monitoring with ALOS/PALSAR imagery data over Northern California and Southern Oregon, USA: Remote Sensing of Environment, v. 124, p. 348-359.

Yang, S. M., Li, J. & Wang, Q., 2008. The deformation pattern and fault rate in the Tianshan Mountains inferred from GPS observations, Sci. China, 51(8), 1064–1080.

Zubovich, A., X. Wang, Y. Scherba, G. Schelochkov, R. Reilinger, C. Reigber, O. Mosienko, P. Molnar, W. Michajljow, V. Makarov, J. Li, S. Kuzikov, T. Herring, M. Hamburger, B. Hager, Y. Dang, V. Bragin, and R. Beisenbaev, 2010, GPS velocity field for the Tien Shan and surrounding regions: Tectonics, v. 29.